論文 / 著書情報
Article / Book Information

題目(和文)	ブロックコポリマー系熱可塑性エラストマーのモルフォロジーおよびナノメカニカル特性評価
Title(English)	Morphological and Nanomechanical Characterization of Block Copolymer-Based Thermoplastic Elastomers
著者(和文)	劉浩男
Author(English)	Haonan Liu
出典(和文)	学位:博士（工学）, 学位授与機関:東京工業大学, 報告番号:甲第11801号, 授与年月日:2022年3月26日, 学位の種別:課程博士, 審査員:中嶋 健,福島 孝典,原 正彦,古屋 秀峰,澤田 敏樹
Citation(English)	Degree:Doctor (Engineering), Conferring organization: Tokyo Institute of Technology, Report number:甲第11801号, Conferred date:2022/3/26, Degree Type:Course doctor, Examiner:,,,,
学位種別(和文)	博士論文
Type(English)	Doctoral Thesis

Tokyo Institute of Technology
School of Materials and Chemical Technology
Department of Chemical Science and Engineering

Morphological and Nanomechanical Characterization of Block Copolymer-Based Thermoplastic Elastomers

by

Haonan LIU

M.E., Tokyo Institute of Technology (2019)

Submitted in part fulfillment of the requirements for
the degree of
Doctor of Engineering
at the
Tokyo Institute of Technology, March 2022

Morphological and Nanomechanical Characterization of Block Copolymer-Based Thermoplastic Elastomers

by

Haonan LIU

Submitted to the School of Materials and Chemical Technology
in partial fulfillment of the requirements for the degree of
Doctor of Engineering

Abstract

Thermoplastic elastomers (TPEs) retain permanent deformation after elongation, preventing them from replacing rubber as an environmentally friendly material. To address TPE's vulnerability, in this thesis, an in situ atomic force microscopy (AFM) is used to characterize the evolution of TPEs' microstructure and micromechanical properties before, during, and after stretching. A finite element analysis (FEA) is then developed and implemented to visualize the local behavior of TPE at the nanoscale. Experiments and data analysis show that solving the hard-domain splitting problem in TPE's microphase separated structure is crucial to increasing its strength.

Chapter 1, "Introduction A: Thermoplastic Elastomers", gives an overview of the TPEs' microphase-separated structure of the hard domain and soft matrix, as well as their mechanical properties, which combine flexibility and toughness like crosslinked rubber. In TPE materials, however, because the hard domain acts as a physical crosslinking point, the crosslinking point's binding force is weaker than that of chemically crosslinked rubber, and stress relaxation and residual strain are considered inferior. The importance of elucidating the macroscopic and microscopic structure-property relationships for TPE materials under deformation is discussed to provide design guidelines for TPE materials that can replace cross-linked rubbers. It is also discussed that, while molecular dynamics (MD) simulations predict hard domain behavior during deformation, experimental techniques to validate the predictions are lacking.

Chapter 2, "Introduction B: Atomic Force Microscopy for Polymer Science", discusses the principle of simultaneous measurement of structure and properties of polymeric materials by a nano-palpation technique based on AFM, as well as the effect of deformation of the AFM tip on the sample. It also presents a typical Johnson-Kendall-Robert (JKR) contact theoretical

model for analyzing the load-deformation curve produced when an AFM probe is deformed into a sample. The in-situ nano-palpation AFM is also developed and described, which allows in-situ observation of nanostructure and physical properties of specimens under deformation, as well as investigation of stress relaxation and residual strain in TPE materials.

Chapter 3, "Dynamic Stress Network in the TPE", investigates the macroscopic stress relaxation phenomenon of TPE materials under constant strain using a block copolymer TPE, styrene-ethylene-butylene-styrene (SEBS). At 50% elongation, in situ AFM is used to investigate the microstructure and properties of SEBS. It has been confirmed that when the soft matrix is elongated, stress chains connecting the hard domains form in the soft matrix, and that the soft matrix modulus decreases while the number of hard domains increases in the early stages of the relaxation process, before stabilizing in the later stages. Furthermore, by focusing on a specific local region, the formation of hard domains, the emergence of new stress chains, and the splitting of hard domains, i.e., the existence of a dynamic stress network, have been clarified. The topology of the polymer is permanently changed by the dynamic stress network, implying that it is caused by stress relaxation phenomena.

Chapter 4, "Nanoscale Strain-Stress Mapping for the TPE", develops an FEA program for AFM images to better understand the relationship between the "dynamic stress network" and the property changes of TPE materials. In this program, the hard domain distributed in the AFM deformation image is extracted as a set of discrete points and divided into each image by Delaunay triangulation. The strain in each triangle region is calculated during the relaxation process and combined with the AFM modulus image, the local strain and local stress can be discussed. In the early stage of the relaxation process, severe contraction occurs inside the material along the tensile direction and stress concentration is observed. In the later stage, unlike the early stage, the average strain in the tensile direction becomes close to zero, the region of stress concentration disappears, and the stress is uniformly distributed over a small area, describing the visualization of the stress relaxation behavior of TPE materials at a microscopic level.

Chapter 5, "Heterogeneously Formation of the Stress Network in the TPE", observes the microstructure and physical properties of the initial elongation process of the TPE material from unelongated to about 45% elongation by in situ nano-palpation AFM. The micro-elastic modulus and macro-stress were measured. Since both micro-elastic modulus and macro-stress show

a non-linear correlation with strain, the FEA method will be used to study them in detail. Initially, almost all regions deformed regularly, but at the cost of stress concentration in some regions. As the strain increases, non-uniform deformation due to accumulated stresses begins. Finally, all the domains are simultaneously undergoing negative deformation with stress relaxation. The number of domains decreases and then increases during this process, which establishes consistency with the MD simulation prediction.

Chapter 6, "AFM Characterization of Triptycene-Appended Polymers", investigated triptycene-appended polymers by AFM. The triptycene units in the side chains of the block copolymer and both terminals of the polymer are described as a special aggregation structure that improves the mechanical properties of the original polymer.

Chapter 7, "Summary and Open Questions", summarizes the contents of this thesis and describes the prospects.

Acknowledgements

The content presented in this thesis represents over three years of research and experimentation that would not have been possible without the outpouring support from family, faculty, colleagues, and friends.

First and foremost I would like to express my sincere gratitude to my research supervisor Ken Nakajima-sensei for the academic guidance and financial support, for encouraging me to challenge unprecedented research topics, and for allowing me the freedom to pursue my own ideas.

I am also deeply thankful to the members of my dissertation committee: Takanori Fukushima-sensei, Masahiko Hara-sensei, Hidemine Furuya-sensei, Toshiki Sawada-sensei for generously offering their time throughout the review of this thesis.

I wish to thank various people for their contribution to this thesis, Tomoya Fukui-sensei, Yugen Chen-san and Ayami Itagaki-san of Laboratory for Chemistry and Life Science, for providing samples and valuable discussion; Tadahiko Shinshi-sensei and Rina Nishida-san of Department of Mechanical Engineering for their help in designing the in-situ stretcher.

My deep appreciation goes out to Xiaobin Liang-san, for his patient guidance, enthusiastic encouragement and useful critiques of this research work. I also deeply thank to Makiko Ito-san for her invaluable advice, guidance and taking some time to discuss and enrich my work.

Many thanks also to researchers: Ling Gao-san, Kim Hung Nguyen-san and clerical assistant: Hiromi Araki-san for lab facilities and kind help during the research and lab life.

I do extend my profound regards to PhD colleagues: Koji Okamoto-san, Ryohei Hosoya-san, Akihiro Naruke-san, Hiroyuki Watabe-san, Ayumi Ando-san for their kind help, encouragement and suggestions, which helped me in successful completion of this thesis.

With great appreciation I shall acknowledge all my labmates: Mishael Eleosca Gunawan, Xu Li, Yuki Okinaga, Ryusei Nomura, Koki Hara, Hayate Haruno, Qingyan Shen, Takashi Kikuchi, Hiroki Sagawa, Kohei Shiomi, Kei Sekine, Dingrui Wang, Toru Kobayashi, Ren Tajiri, Yuto Miyata, Ryo Miyata, Kaede Mogi, Pijak Thidaychanun, Mingjun Tang, Kotaro Osako, Yasuharu Kashimori, Airi Sato, Masato Mori, Shun-ichi Nomura, Mari Hanai, Kazuhiko Fujimori

for the stimulating discussions, for the sleepless nights we were working together before deadlines, and for all the fun we have had in the last years.

I would like to thank my family for the continuous support they have given me throughout my time in graduate school. My special thanks goes to my beloved girlfriend Xinqi Cong for her understanding and encouragement not only during my thesis studies but also my life.

The research work in this thesis is mainly supported by JST "Core Research for Evolutionary Science and Technology (CREST)" JPMJCR17J4 and partially supported by JST "Support for Pioneering Research Initiated by the Next Generation (SPRING)" JPMJSP2106. Chapter 6 was performed under the Cooperative Research Program of "Network Joint Research Center for Materials and Devices".

Main Building, Ookayama Campus

Haonan Liu

March 2022

Contents

List of Tables

List of Figures

Chapter 1

Introduction A: Thermoplastic Elastomers

1.1 General

Thermoplastic elastomer (TPE) is a thermoplastic high molecular-weight material that behaves like a rubbery elastic material at room temperature and undergoes plastic deformation at high temperatures[1;2]. Therefore, it is easy to obtain TPE products with rubber elasticity by using a molding machine for thermoplastics. Usually, rubber products are manufactured by kneading reinforcing fillers, vulcanizing agents, and other auxiliary agents to chain polymers with low glass transition temperature and capable of micro-Brownian motion at room temperature, then heating them at high temperature after preforming to cause intermolecular crosslinking (vulcanization) reactions. The rubber industry has long been energy-intensive and human resource-intensive. On the other hand, the thermoplastic products that make up most plastics can be obtained by simply shearing the raw plastic at a high temperature above the softening point to make it flow, then injecting it into a cold mold and manufacturing it using various molding machines. Unlike the case of vulcanized rubber, material recovery is also easy. Therefore, it was thought that there should be a rubber that could be molded and processed like plastic.

By combining the processing advantages of thermoplastics with the performance properties of elastomers, TPEs can be processed relatively easily using thermoplastic methods such as extrusion and injection molding, eliminating time-consuming and environmentally unfriendly methods of rubber processing, especially vulcanization. Industrial production of TPE products began in the 1960s. In 1965, Shell developed and industrialized a linear styrene-butadiene-styrene triblock copolymer (SBS, Fig. 1.1) copolymer by a three-step sequential dosing method using anionic polymerization technology, under the trade name Kraton D. At high temperatures, the polystyrene (PS) and polybutadiene (PB) blocks in SBS are compatible and mobile. Still, at low temperatures, they spin off and form a microphase-separated structure in which the PS domain is finely dispersed as a spherical/cylinder phase in the PB domain on a scale of more than 10 nm. Since the PS domain plays the role of both crosslinking point and reinforcing material in vulcanized rubber, elastic properties can be achieved without adding vulcanizing agents or reinforcing fillers. SBS is considered a pioneer in polymer nanotechnology due to the characteristic length of the microphase-separated structure.

At present, there are many types of TPE that have been industrially produced[3;4;5], mainly divided into the following types: styrenics, olefins, dienes, vinyl chloride, ammonia esters, esters, amides, organofluorine, silicone, and vinyl, etc. Below is a brief introduction.

1. Styrene-based thermoplastic elastomers (TPS, TPE-s). The type of products such as SBS, SEBS, SIS, SEPS, SIBS, etc. The characteristic molecular structure is a three-block polymer, the hard segment is polystyrene, the rest are soft segments (rubber phase).

2. Polyolefin thermoplastic elastomer (TPO, POE), composed of rubber and polyolefin, usually rubber components for EPDM, NBR and butyl rubber; polyolefin components are mainly polypropylene (PP) and polyethylene (PE), TPO products in the largest amount of EPDM/PP. TPO prepared by dynamic vulcanization process is referred to as TPV. Such as PP/EPDM (Santoprene), PP/NBR (Geolast), thermoplastics/silicone rubber (TPSiV), etc.

3. Polyurethane thermoplastic elastomer (TPU), from the reaction with isocyanate ammonia ester hard chain segment and polyester or polyether soft chain segment of the mutual block

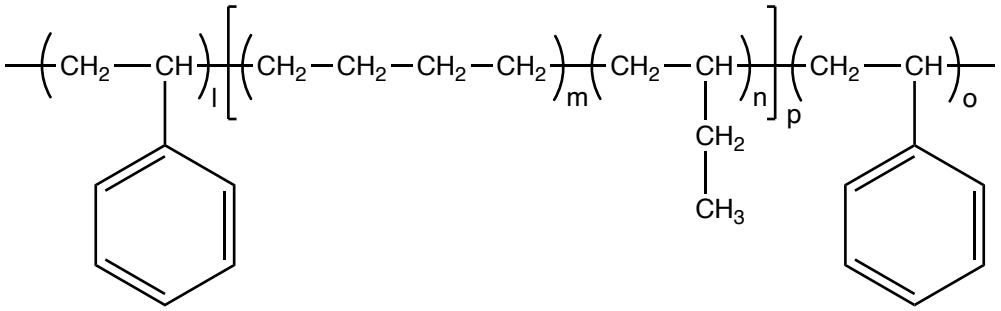

Styrene-ethylene-butylene-styrene triblock copolymer (SEBS)

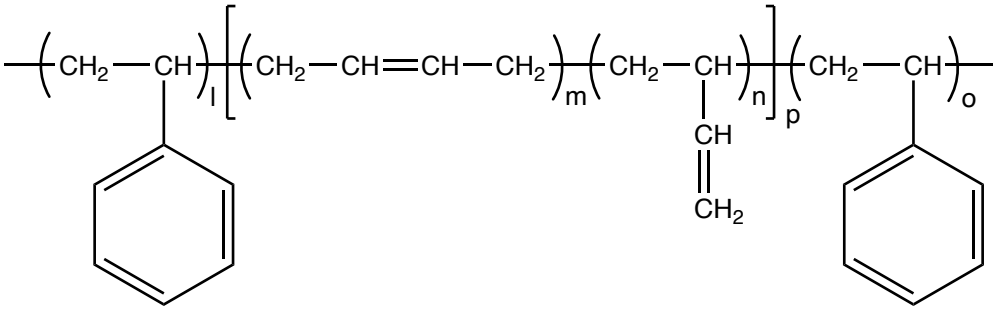

Styrene-butadiene-styrene triblock copolymer (SBS)

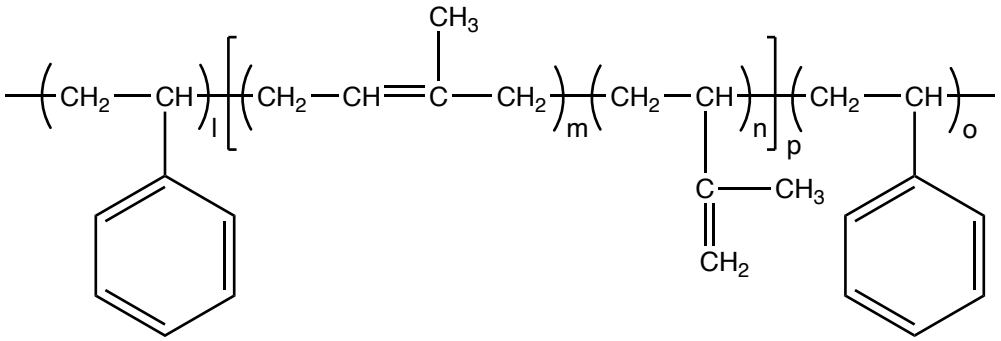

Styrene-isoprene-styrene triblock copolymer (SIS)

Figure 1.1: The molecular structures of SEBS, SBS, and SIS triblock copolymer.

combination of thermoplastic polyurethane rubber, referred to as TPU.

4. Polyester ether thermoplastic elastomer (TPEE), polybutylene terephthalate (PBT) as a hard segment, polyether or polyester as a soft segment of the block copolymer.

5. Polyamide thermoplastic elastomer (TPAE), such as polyester amide, polyether ester amide, polycarbonate-ester amide, polyether-amide and other hard segments for polyamide, soft segments for polyether and/or polyester segmented block copolymers.

6. Diene thermoplastic elastomers, mainly natural rubber isomers, is called trans-natural rubber (T-NR). The main varieties are T-NR-trans polyisoprene rubber (TPI) and be-

tween the same 1,2-polybutadiene (TPB).

7. Organofluorine thermoplastic elastomer (TPF)
8. Polyvinyl chloride thermoplastic elastomer, mainly divided into thermoplastic PVC (TPVC) and thermoplastic chlorinated polyethylene (TCPE) two categories.
9. Acrylate thermoplastic elastomer
10. Silicone rubber thermoplastic elastomer

All TPE terms used in this thesis default to the most widely used styrene-based TPE.

1.2 Structure of BCP-Based TPE

The nature of the molecular structure gives TPEs a higher degree of elasticity. All TPEs are composed of crystalline (glassy) and non-crystalline (amorphous) domains. They can be physical blends or alloys of crystalline and non-crystalline polymers or block copolymers, which are chemical mixtures of crystalline and non-crystalline structural blocks in the polymer chain.

In the case of TPEs and blends, the hard chain segments are responsible for the plastic properties of the final product, including ease of processing and high-temperature resistance, as well as material properties such as tensile strength or chemical resistance. Adhesion is also determined by these properties. Soft chain segments are responsible for elastic or resilient properties. They determine material properties such as hardness, elasticity, and the degree of permanent deformation (Fig. 1.2).

From the SBS example, there must be a soft segment domain that shows the elasticity of the rubber and a hard segment domain that prevents plastic deformation and provides reinforcement in the material to show properties as a TPE. Since SBS development, a wide variety of TPEs has been developed and marketed. In addition to those TPEs based on polymer synthesis, such as block copolymers and graft polymers, the types of TPEs are further increased when rubber/resin blends are included. In particular, Toyota super olefin polymer (TSOP),

which was developed by reversing the concept of impact-resistant plastics, was introduced by Toyota in 1991 and has become the global standard for automotive bumper materials. This technology, in which the elastomer is a continuous phase, and the polypropylene (PP) micro-crystals are finely dispersed, can be regarded as a model for TPE materials. However, there are still many issues to be solved in terms of materials, such as heat resistance, creep resistance, and fatigue resistance. In addition, TPEs have difficulties in long-term durability and stress retention under large deformations like crosslinked rubber.

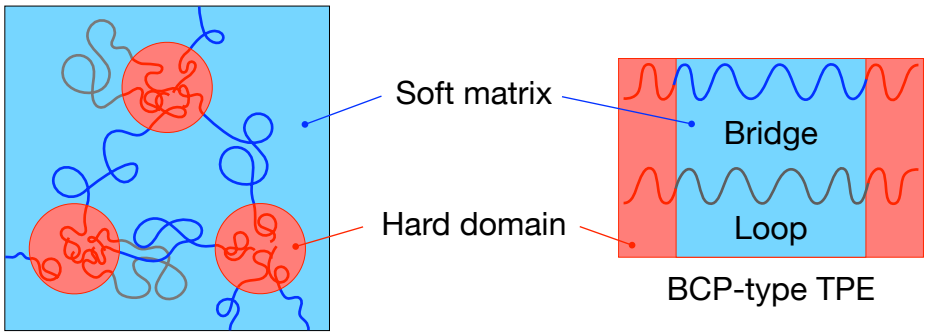

Figure 1.2: Schematic of BCP-type TPE's microphase-separated structure.

1.3 Methods to Improve the Mechanical Strength of TPE

In an ideal TPE material, where complete elastic deformation can occur after stretching without damage to the internal structure, it is necessary that the phase separation structure remains extremely stable. The material deformation pattern in this case is shown in Fig 1.3, the bridge chain formed between the hard domains can maintain the stretch and avoid further collapse. However, this ideal elasticity variation is very difficult for the currently marketed TPE materials. The reason is that in a discontinuous phase separation structure like TPE, the percentage of hard phase has to be controlled in a low range (usually less than 30%), which results in insufficient strength of the hard phase. In this regard, there are two general solutions, one is to improve the strength of the hard phase by molecular design[6;7;8;9] or polymer blending[10], and the other is to construct new topological networks[11] so that the individual hard phases are subjected to smaller forces during the stretching process. However, either method requires the most profound characterization of the formation mechanism of TPE deformation,

damage, deterioration, etc., which requires the cooperation of the state-of-the-art analytical techniques.

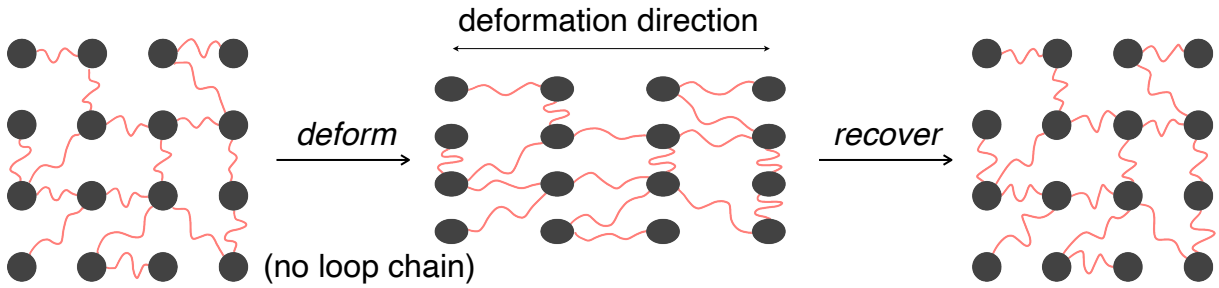

Figure 1.3: Schematic of the elastic deformation of BCP-type TPE.

1.4 Analytical Techniques for TPE

To date, in addition to traditional testing techniques such as tensile test, rheomter, dynamic mechanical analysis, etc., characterization techniques at the nano level are becoming more and more dominant. Many researchers used small angle X-ray scattering (SAXS)[12;13;14;15;16;17], Fourier transform infrared spectroscopy (FT-IR)[18;19;20;21], and transmission electron microscopy (TEM)[16;22;23;24;25;15;7] to investigate the deformation of BCP-based TPEs. More recently, in-situ SAXS has been used to observe the microstructure of TPE during macroscopic elongation[26]. So far, as shown in Fig. 1.4, by experiment[17;26] and simulation[27;28], it is found that hard domain could be deformed, fused, and divided with the increase of strain. Although the simulations give many predictions of the dynamic behavior of the domain, however, the existence of factors such as different stretching speeds in the simulations than in the real experiments and the inability of the set parameters to fully restore the real situation make it urgent to repeat the results of the simulations using experimental techniques. Alternatively, AFM has the function to get the force-distance curves of the surface by deforming the material with a probe and employing contact mechanics to obtain the elastic modulus, adhesion energy, and other physical characteristics, which makes AFM the only technology available that can simultaneously derive the target microscopic region's structure and mechanical properties[29;30;31].

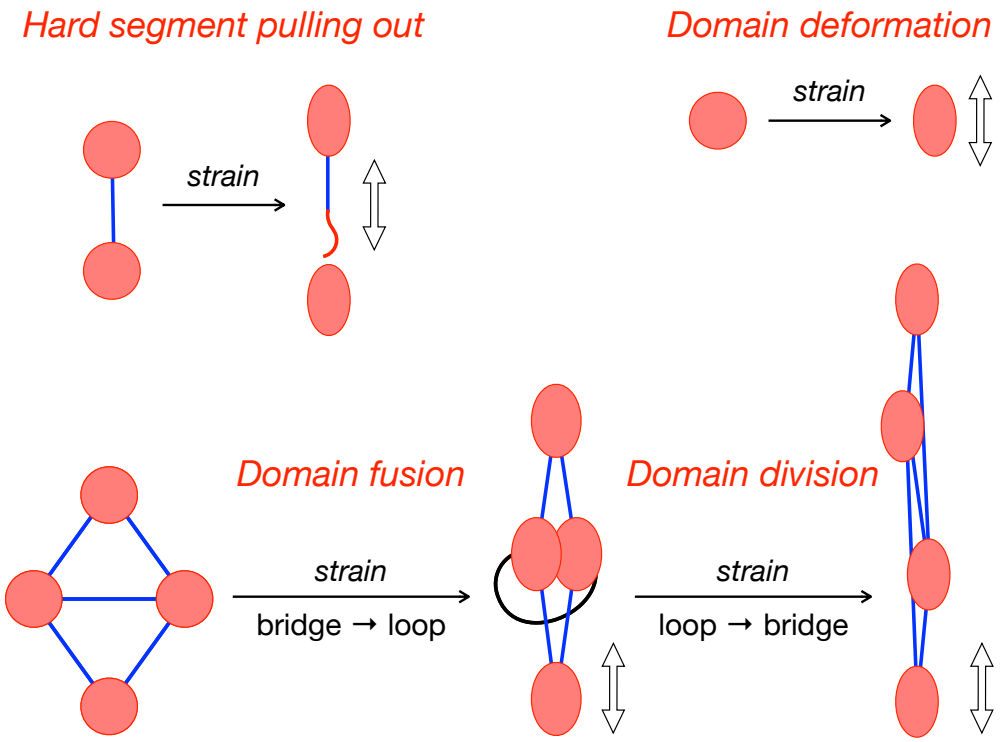

Figure 1.4: Schematic diagram of the dynamic behavior of the TPE during the stretching process.

1.5 References

[1] Akiba, M. a. & Hashim, A. Vulcanization and crosslinking in elastomers. *Progress in polymer science* **22**, 475–521 (1997).

[2] Spontak, R. J. & Patel, N. P. Thermoplastic elastomers: fundamentals and applications. *Current opinion in colloid & interface science* **5**, 333–340 (2000).

[3] Bhowmick, A. K. & Stephens, H. *Handbook of elastomers* (CRC Press, 2000).

[4] Shanks, R. A. & Kong, I. General purpose elastomers: structure, chemistry, physics and performance. *Advances in Elastomers I* 11–45 (2013).

[5] Drobny, J. G. *Handbook of thermoplastic elastomers* (Elsevier, 2014).

[6] Shi, W. *et al.* Toward strong thermoplastic elastomers with asymmetric miktoarm block copolymer architectures. *Macromolecules* **47**, 2037–2043 (2014).

[7] Shi, W. *et al.* Mechanics of an asymmetric hard–soft lamellar nanomaterial. *ACS nano* **10**, 2054–2062 (2016).

[8] Rosenbloom, S. I. & Fors, B. P. Shifting boundaries: controlling molecular weight distribution shape for mechanically enhanced thermoplastic elastomers. *Macromolecules* **53**, 7479–7486 (2020).

[9] Weidisch, R. *et al.* Tetrafunctional multigraft copolymers as novel thermoplastic elastomers. *Macromolecules* **34**, 6333–6337 (2001).

[10] Puskas, J. E., Kwon, Y., Altstädt, V. & Kontopoulou, M. Blends of poly (2, 6-dimethyl-1, 4-phenylene oxide)(ppo) with polystyrene-based thermoplastic rubbers: A comparative study. *Polymer* **48**, 590–597 (2007).

[11] Hayashida, K., Dotera, T., Takano, A. & Matsushita, Y. Polymeric quasicrystal: Mesoscopic quasicrystalline tiling in a b c star polymers. *Physical Review Letters* **98**, 195502 (2007).

[12] Inoue, T., Moritani, M., Hashimoto, T. & Kawai, H. Deformation mechanism of elastomeric block copolymers having spherical domains of hard segments under uniaxial tensile stress. *Macromolecules* **4**, 500–507 (1971).

[13] Séguéla, R. & Prud'Homme, J. Affinity of grain deformation in mesomorphic block polymers submitted to simple elongation. *Macromolecules* **21**, 635–643 (1988).

[14] Prasman, E. & Thomas, E. L. High-strain tensile deformation of a sphere-forming triblock copolymer/mineral oil blend. *Journal of Polymer Science Part B: Polymer Physics* **36**, 1625–1636 (1998).

[15] Honeker, C. C. *et al.* Perpendicular deformation of a near-single-crystal triblock copolymer with a cylindrical morphology. 1. synchrotron saxs. *Macromolecules* **33**, 9395–9406 (2000).

[16] Cohen, Y., Albalak, R. J., Dair, B. J., Capel, M. S. & Thomas, E. L. Deformation of oriented lamellar block copolymer films. *Macromolecules* **33**, 6502–6516 (2000).

[17] Tomita, S. *et al.* Strain-induced deformation of glassy spherical microdomains in elastomeric triblock copolymer films: simultaneous measurements of a stress–strain curve with 2d-saxs patterns. *Macromolecules* **50**, 677–686 (2017).

[18] Zhao, Y. Structural changes upon annealing in a deformed styrene-butadiene-styrene triblock copolymer as revealed by infrared dichroism. *Macromolecules* **25**, 4705–4711 (1992).

[19] Sakurai, S., Sakamoto, J., Shibayama, M. & Nomura, S. Effects of microdomain structures on the molecular orientation of poly (styrene-block-butadiene-block-styrene) triblock copolymer. *Macromolecules* **26**, 3351–3356 (1993).

[20] Kraus, G. & Rollmann, K. Effects of domain and molecular orientations on the mechanical properties of a styrene-butadiene block polymer. *Journal of Macromolecular Science, Part B: Physics* **17**, 407–425 (1980).

[21] Duan, Y. *et al.* Deformation behavior of sphere-forming trifunctional multigraft copolymer. *Macromolecules* **41**, 4565–4568 (2008).

[22] Odell, J. & Keller, A. Deformation behavior of an s-b-s copolymer. *Polymer Engineering & Science* **17**, 544–559 (1977).

[23] Yamaoka, I. & Kimura, M. Effects of morphology on mechanical properties of a sbs triblock copolymer. *Polymer* **34**, 4399–4409 (1993).

[24] Yamaoka, I. Effects of morphology on mechanical properties of styrene-butadiene-styrene triblock copolymer/methyl methacrylate styrene copolymer blends. *Polymer* **37**, 5343–5356 (1996).

[25] Yamaoka, I. Anisotropic behaviour of styrene-butadiene-styrene triblock copolymer/methyl methacrylate-styrene copolymer blends. *Polymer* **39**, 1081–1093 (1998).

[26] Dechnarong, N. *et al.* In situ synchrotron radiation x-ray scattering investigation of a microphase-separated structure of thermoplastic elastomers under uniaxial and equi-biaxial deformation modes. *Macromolecules* **53**, 8901–8909 (2020).

[27] Morita, H., Miyamoto, A. & Kotani, M. Recoverably and destructively deformed domain structures in elongation process of thermoplastic elastomer analyzed by graph theory. *Polymer* **188**, 122098 (2020).

[28] Aoyagi, T., Honda, T. & Doi, M. Microstructural study of mechanical properties of the aba triblock copolymer using self-consistent field and molecular dynamics. *The Journal of Chemical Physics* **117**, 8153–8161 (2002).

[29] Nakajima, K. *et al.* Nano-palpation afm and its quantitative mechanical property mapping. *Microscopy* **63**, 193–208 (2014).

[30] Wang, D. & Russell, T. P. Advances in atomic force microscopy for probing polymer structure and properties. *Macromolecules* **51**, 3–24 (2018).

[31] Garcia, R. Nanomechanical mapping of soft materials with the atomic force microscope: methods, theory and applications. *Chemical Society Reviews* **49**, 5850–5884 (2020).

Chapter 2

Introduction B: Atomic Force Microscopy for Polymer Science

2.1 General

In the recent history of instrumentation development, microscopy has been developing rapidly along with the progress of human science and technology. Scientific research and materials development have been pushed to an unprecedented level of miniaturization with the invention of new microscopy techniques. Since the invention of the scanning tunneling microscope (STM) by Binning et al. in 1982[1], humankind's desire to explore the atomic scale has taken a giant leap forward, and the study of material surface phenomena has become more profoundly understood. Before that, the only instruments that could directly see the size of atoms were field ion microscopy (FIM) and electron microscope (EM). The invention of STM overcame these problems, as the study of atomic dimensions was extremely limited due to the conditions of preparation and operating environment. The principle of STM is to use the electron tunneling effect to obtain atomic images. Still, the sample for STM is basically a conductor, and the surface must be very flat, limiting the use of STM. In 1986, Binning et al. developed the atomic force microscope (AFM)[2], which not only has the ability to resolve atomic dimensions, but also solves the limitations of STM on conductors, making it more convenient for application.

Since the introduction of STM, dozens of types of probe microscopes have been continuously developed. Scanning probe microscope (SPM) is a large family of probe-based microscopes, among which the more familiar techniques are: STM, AFM, near field optical microscope (NSOM), magnetic force microscope (MFM), chemical force microscope (CFM), scanning thermoprobe microscope (SThM), phase probe microscope (PDM), electrostatic force microscope (EFM), lateral frictional force microscope (LFM), etc. Among the various SPM techniques, AFM is the most widely used and can be applied to a variety of items, such as metallic materials, polymers, biological cells, etc. It can be operated in atmospheric, vacuum, electrical and liquid phase environments for different physical properties analysis. Therefore, AFM has a wide range of applications in the study of biological materials, crystal growth, and action forces.

Depending on the tip-sample material and the tip-sample distance, the forces between the tip and the sample can be interatomic repulsion, van der Waals attraction, elastic force, adhesion, magnetic and electrostatic forces, and the frictional forces generated by the tip during scanning. Fig. 2.1 shows the typical inter-atomic interaction in imaging. The black curve is a combination of long-range attractive and short-range repulsive interaction forces called the Lennard-Jones Potential. At larger distances, the force is attractive, which switches to a repulsive force when two atoms are brought closer together. The orchid curve represents a repulsive interaction, while the teal curve represents an attractive interaction. By controlling and detecting these forces between the tip and the sample, not only the surface morphology of the sample can be characterized at high resolution, but also the surface properties corresponding to the forces can be analyzed: LFM can analyze the friction coefficient of the studied material; MFM can study the magnetic domain distribution on the sample surface; EFM can analyze the sample surface potential, the dielectric constant of the film, and the deposited charge. In addition, AFM can manipulate, modify and process atoms and molecules, and design and create new structures and substances[3]

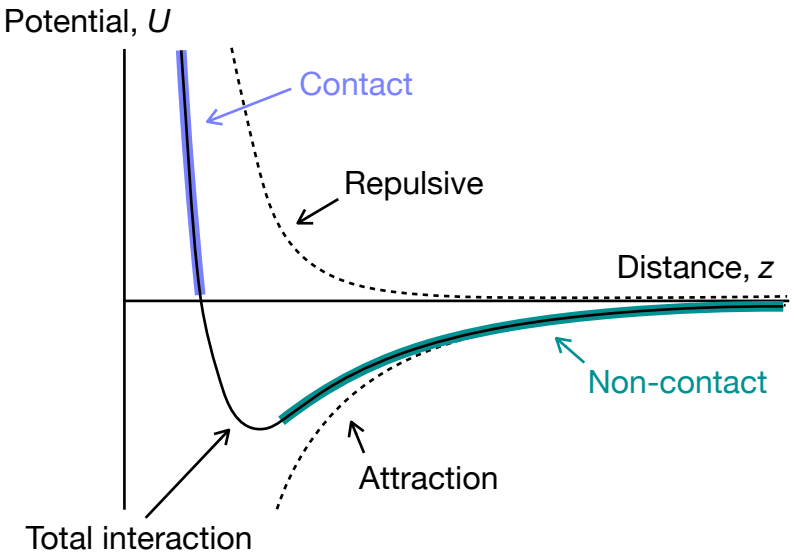

Figure 2.1: Inter-atomic interaction potential U vs. distance z.

2.2 The Working Principle of AFM

The principle of operation is that a micro-cantilever, which is sensitive to very weak forces, is fixed at one end and has a tiny tip at the other end, which is in gentle contact with the sample surface. Due to the extremely weak repulsive force between the atoms at the tip of the tip and the sample surface, the cantilever with the tip will move in an undulating direction perpendicular to the sample surface by controlling this force to be constant during the scan, corresponding to the isotope of the force between the atoms. Using optical detection or tunneling current detection, the change in position corresponding to each point of the scan is measured, and the signal is amplified and converted to obtain a three-dimensional image of the sample surface at the atomic level.

The AFM consists of a piezoelectric scanner that performs raster scanning and z-positioning, feedback electronics, an optical reflection system, a probe, an anti-vibration system, and a computer control system (Fig. 2.2). The piezoelectric ceramic tube controls the movement of the sample in the x, y, and z directions. When the sample is scanned along the x/y direction relative to the probe tip, the distance between the probe tip and the sample surface is changed due to the high and low undulations of the surface. When the laser beam is irradiated to the back of the cantilever and then reflected to the position-sensitive photo-detector, the difference

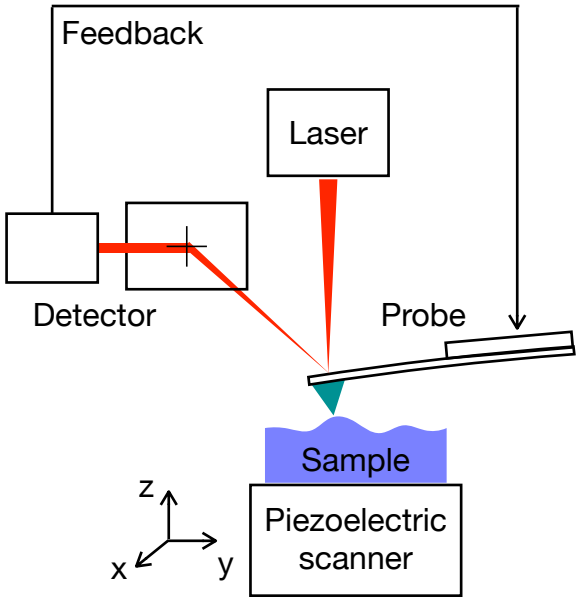

Figure 2.2: Schematic diagram of the principle of AFM.

in laser intensity received by the detector in different quadrants forms a certain proportional relationship with the deformation of the cantilever. Feedback loop according to the detector signal and the difference between the preset value, and constantly adjust the distance between the tip and the surface. Keeping the force between the tip and surface unchanged can get the morphology image. This measurement mode is called constant force mode. When the surface of the sample is known to be very smooth, the scanning can be performed in constant height mode, i.e., the distance between the tip and the sample is kept constant. At this point the magnitude of the force directly reflects the surface morphology image.

2.2.1 Basic Operation Modes of AFM

At present, there are three basic modes of AFM operation, which can be distinguished as contact , non-contact, and tapping modes. Contact and non-contact are susceptible to other external factors, such as the attraction of water molecules, which can cause scratches on the surface of the material and image distortion by poor resolution; thus, there are limitations on their use, especially in biological and polymer soft materials. The following is a brief introduction to the basic principles of the three basic forms.

Contact Mode

The tip is used to interact with the atomic force on the surface (must be in contact), so that the very soft probe arm is deflected. The back of the probe arm is irradiated with a special tiny laser light, and the laser light reflected by the probe arm is used as a two-phase photo diode (laser light phase detector) to record the change of laser light deflection by the probe arm. The interatomic repulsive force between the probe and the sample is about 10^{-6} to 10^{-9} N. However, since the tip is in contact with the surface, excessive forces can still damage the sample, especially on soft materials such as polymers and cellular organisms. However, better resolution is usually obtained on harder materials.

Non-Contact Mode

In order to solve the shortcomings of contact AFM that may damage the sample, non-contact AFM was developed, which operates by using the long distance attraction - van der Waals force. The distance between the probe and the sample and the amplitude of the probe must strictly follow the van der Waals force principle, so the distance between the probe and the sample must not be too far, the amplitude of the probe must not be too large (about 2 to 5 nm), and the scanning speed must not be too fast. When the sample is placed in atmospheric environment and the humidity exceeds 30%, a 5 to 10 nm thick film of water molecules will cover the surface of the sample, which makes it difficult or wrong to feedback.

Tapping Mode

Tapping mode is improved by bringing the tip closer to the sample and increasing the amplitude of the probe (10-300 kHz) with force of about 10^{-12} N. The probe has resonant vibration and the amplitude can be adjusted to have intermittent slight beating contact with the material surface. The amplitude in the tapping mode AFM can be adjusted to be small enough not to interfere with the water molecule film, and large enough not to damage the probe by hard knocking on the sample surface, with an ultimate resolution of 2 nm in the XY plane. It does

not cause permanent damage in the z-direction. In the x-y direction, because the probe is intermittently bouncing in contact, it will not cause permanent damage as in contact mode, where the probe is dragged in the x-y direction. However, due to the high frequency of probe strikes, the tip of the probe can be damaged for very hard samples.

2.2.2 AFM Nanomechanical Mode

From the beginning of the development of AFM, there were signs that it would be applied to nanomechanics not only in polymers but also in various other materials fields. Nowadays, there are various modes for imaging mechanical property information[4;5;6]. In these modes, the AFM tip is not scanned along the surface of the sample, but is repeatedly brought into contact with the sample perpendicular to the surface, and then pulled away. The relationship between the sample deformation and the interaction force is then combined with contact mechanics such as Hertz theory, Derjaguin-Muller-Toporov (DMT)[7] theory and JohnsonKendall-Roberts (JKR)[8] theory. The DMT and JKR theories provide information on the condensation energy as well as the elastic modulus. The DMT and JKR theories provide information on the cohesive energy as well as the elastic modulus. The elastic modulus of an unstretched sample often correlates well with the tensile modulus (Young's modulus). On the other hand, when the AFM probe is pressed against a macroscopically elongated sample, the obtained modulus is generally larger than that of the unelongated sample. This is natural because stress is applied at various locations corresponding to the macroscopic strain, but the resulting stress distribution is very non-uniform, reflecting the local nature of the sample.

For the static AFM force mapping mode, two different measurement modes are commonly used. Force-volume (FV) AFM is the mode in which a series of force-distance curve are recorded at each point of the specimen surface. The rate of force-distance curve acquisition is about 1–10 Hz. The PeakForce quantitative nanomechanical mapping (QNM) mode was also utilized. The method can also generate force-distance curves and has a much higher acquisition rate (0.5–2 kHz). In the case of iroprene rubber (IR) specimens, both FV and QNM provide an accurate estimate of rubbery modulus[4], whereas QNM provides an incredibly higher modulus for

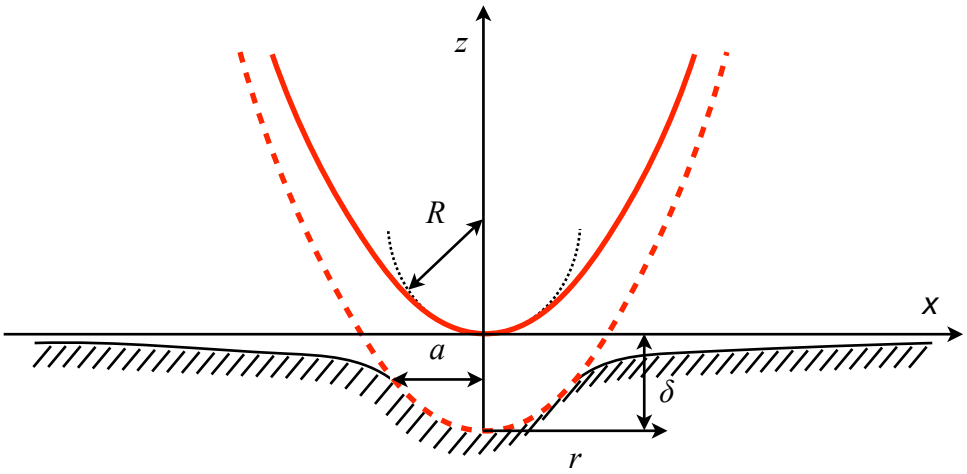

Figure 2.3: Schematic diagram of the deformation of the sample surface by the probe tip.

styrene-butadiene rubber (SBR) due to the faster acquisition rate, where the time-temperature superposition (TTS) principle is important.

In analyzing force-distance curves on rubbery materials with significant adhesive interaction, a contact mechanics model, first developed by Johnson et al. and thus known as the JKR model[8], can be used to relate the applied force F to the contact radius a for an indenting probe of the radius R (Fig. 2.3) as follows;

$$a = \left(\frac{R}{K}\right)^{1/3} \left(\sqrt{F - F_c} + \sqrt{-F_c}\right)^{2/3}, \tag{2.1}$$

where K, F_c are the reduced modulus and the maximum adhesive force, respectively. The contact radius directly correlates with the sample deformation δ by the following equation,

$$\delta = \frac{a^2}{R} - \frac{4}{3}\sqrt{\frac{a\,(-F_c)}{KR}}\,. \tag{2.2}$$

To obtain a direct relationship between F and δ, it is difficult to perform implicit-function curve fitting by eliminating a. To overcome this difficulty, instead of fitting the $F-\delta$ curve completely, two special points on the curve can be chosen to directly calculate the sample modulus, which is known as the JKR two-point method[9]. The balance point ($delta_0$, 0), where the apparent force F exerted on the cantilever becomes zero, and the maximum adhesion point ($delta_1$, F_c), where

the adhesive force reaches the maximum negative value on the unloading curve, are the two points. Combining the above equations yields an algebraic formula for calculating the reduced modulus.

$$K = \left(\frac{1+16^{1/3}}{3}\right)^{3/2} \frac{(-F_c)}{\sqrt{(\delta_0-\delta_1)^3 R}} \,. \tag{2.3}$$

This JKR two-point method has been shown to accurately determine the elastic modulus of a variety of rubbers and glassy polymers.

2.3 In-Situ AFM

As the research in materials science is gradually moving to depth, there is an urgent need for researchers to conduct more in-depth studies on the mechanism of action, structural changes, and factors affecting the properties of materials. Then, the traditional ex-situ research methods can no longer meet the current needs. In-situ characterization techniques, which have been developed in the last three decades, allow 'on-line' analysis of specific reaction processes using different instrumentation. This technique is often used to elucidate the changes in a material process by means of a specific device that performs continuous and simultaneous analysis of the substance and traces a series of structures parameterized by time or other relevant conditions.

Because AFM testing causes little damage to the sample, in situ AFM techniques are widely used to measure the mechanical and electromechanical properties of nanomaterials[10]. So far, in situ AFM has been used to study batteries[11;12], crystallization[13;14], phase transition[15;16], biomolecules[17;18] etc. Since AFM can combine various external stimuli such as light, electricity, heat, and chemical reactions to observe the structure and physical properties of the sample, it makes in situ AFM a very promising application.

2.3.1 In-Situ AFM Nanomechanics

In-Situ AFM Nanomechanics is based on the In-Situ AFM technique, which combines the analysis of force curves obtained from tests to grasp changes in the properties of substances in response to external stimuli (Fig. 2.4). Since obtaining force curves requires applying deformation to the material surface, the test objects are usually soft materials, especially polymers. The external stimuli that can be applied include tensile, compressive, etc. However, polymers, especially block copolymers, often have a structural scale of just a few tens of nanometers, and in order to maintain a high resolution, the scan size is usually only a few hundred nanometers or micrometers. It becomes very difficult to continuously track the same region after the application of external stimuli, and this challenge is the main research object of this thesis.

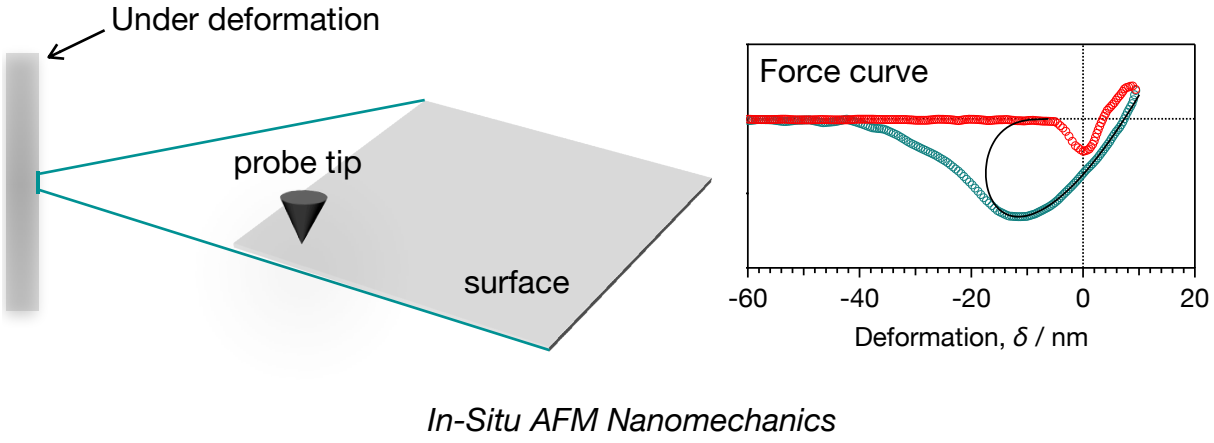

Figure 2.4: The working principle of in-situ AFM nanomechanics.

2.4 The Objective of This Thesis

In this thesis, in order to solve the common macroscopic stress-strain characteristics of TPE (Fig. 2.5), including stress relaxation, permanent deformation, etc., I developed and used in situ AFM nanomechanics to make real-time structural and nanomechanical property observations of TPE materials under deformation. Since AFM can simultaneously obtain the structural and physical properties of an observed region, there is no suitable analysis method to analyze a series of in situ images in depth; therefore, a corresponding program is planned to be developed.

Finally, in order to develop new high-strength TPEs, in addition to the marketed TPE samples, unmarketed polymer materials with potential were also characterized using AFM.

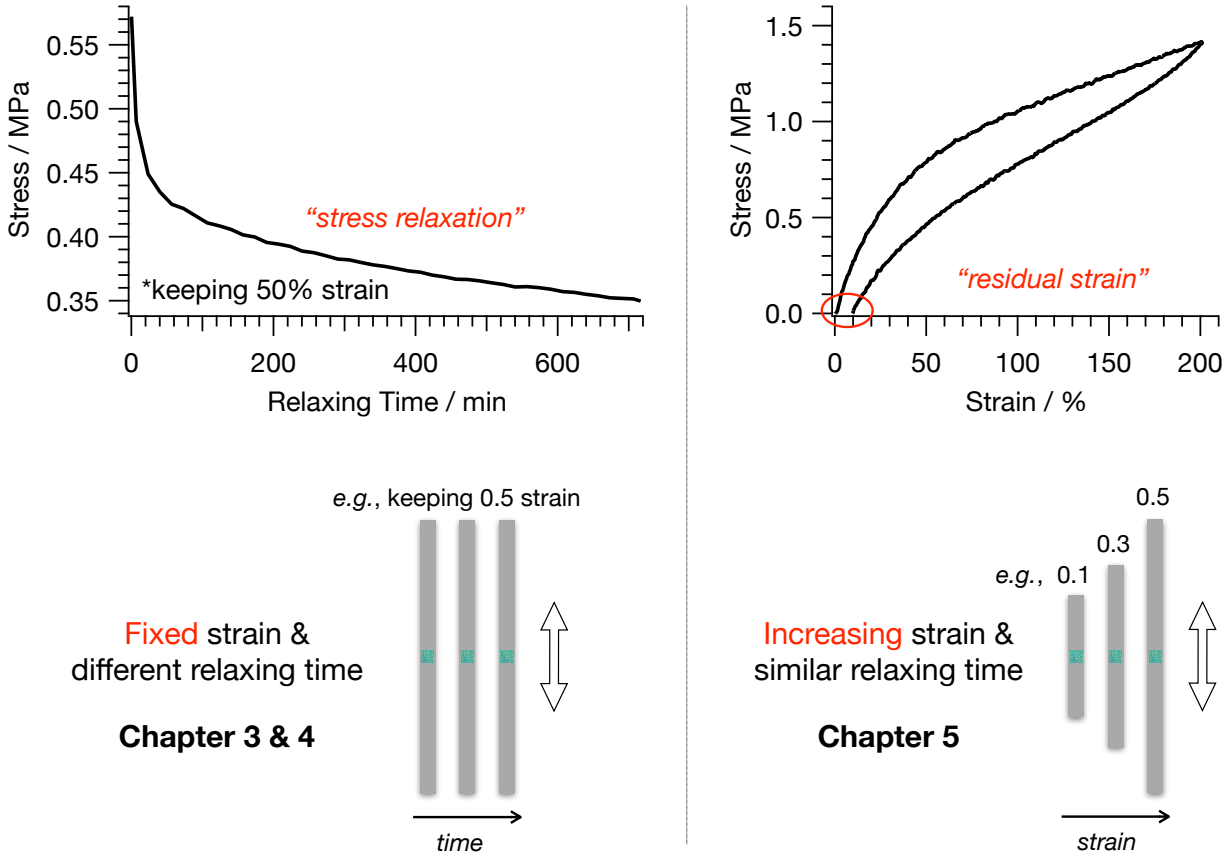

Figure 2.5: Common macroscopic stress-strain characteristics of TPE and the in situ AFM nanomechanics corresponding to them.

2.5 References

[1] Binnig, G., Rohrer, H., Gerber, C. & Weibel, E. Surface studies by scanning tunneling microscopy. *Physical review letters* **49**, 57 (1982).

[2] Binnig, G., Quate, C. F. & Gerber, C. Atomic force microscope. *Physical review letters* **56**, 930 (1986).

[3] Custance, O., Perez, R. & Morita, S. Atomic force microscopy as a tool for atom manipulation. *Nature nanotechnology* **4**, 803–810 (2009).

[4] Nakajima, K. *et al.* Nano-palpation afm and its quantitative mechanical property mapping. *Microscopy* **63**, 193–208 (2014).

[5] Wang, D. & Russell, T. P. Advances in atomic force microscopy for probing polymer structure and properties. *Macromolecules* **51**, 3–24 (2018).

[6] Garcia, R. Nanomechanical mapping of soft materials with the atomic force microscope: methods, theory and applications. *Chemical Society Reviews* **49**, 5850–5884 (2020).

[7] Derjaguin, B. V., Muller, V. M. & Toporov, Y. P. Effect of contact deformations on the adhesion of particles. *Journal of Colloid and interface science* **53**, 314–326 (1975).

[8] Johnson, K. L., Kendall, K. & Roberts, a. Surface energy and the contact of elastic solids. *Proceedings of the royal society of London. A. mathematical and physical sciences* **324**, 301–313 (1971).

[9] Sun, Y., Akhremitchev, B. & Walker, G. C. Using the adhesive interaction between atomic force microscopy tips and polymer surfaces to measure the elastic modulus of compliant samples. *Langmuir* **20**, 5837–5845 (2004).

[10] Li, X., Sun, M., Shan, C., Chen, Q. & Wei, X. Mechanical properties of 2d materials studied by in situ microscopy techniques. *Advanced Materials Interfaces* **5**, 1701246 (2018).

[11] Beaulieu, L., Beattie, S., Hatchard, T. & Dahn, J. The electrochemical reaction of lithium with tin studied by in situ afm. *Journal of the Electrochemical Society* **150**, A419 (2003).

[12] Beaulieu, L., Hatchard, T., Bonakdarpour, A., Fleischauer, M. & Dahn, J. Reaction of li with alloy thin films studied by in situ afm. *Journal of the Electrochemical Society* **150**, A1457 (2003).

[13] Malkin, A., Kuznetsov, Y. G. & McPherson, A. An in situ afm investigation of catalase crystallization. *Surface science* **393**, 95–107 (1997).

[14] Land, T., De Yoreo, J. & Lee, J. An in-situ afm investigation of canavalin crystallization kinetics. *Surface Science* **384**, 136–155 (1997).

[15] Seantier, B., Breffa, C., Felix, O. & Decher, G. In situ investigations of the formation of mixed supported lipid bilayers close to the phase transition temperature. *Nano Letters* **4**, 5–10 (2004).

[16] Wiedemair, J. *et al.* In-situ afm studies of the phase-transition behavior of single thermoresponsive hydrogel particles. *Langmuir* **23**, 130–137 (2007).

[17] Ando, T. *et al.* A high-speed atomic force microscope for studying biological macromolecules. *Proceedings of the National Academy of Sciences* **98**, 12468–12472 (2001).

[18] Ando, T., Uchihashi, T. & Fukuma, T. High-speed atomic force microscopy for nano-visualization of dynamic biomolecular processes. *Progress in Surface Science* **83**, 337–437 (2008).

Chapter 3

Dynamic Stress Network in the TPE

3.1 General

Elastomers' numerous benefits make them useful in a wide range of applications[1;2]. Traditional thermoset elastomers, like filler-reinforced vulcanized rubber, have outstanding mechanical qualities because of their chemical-crosslink network. They can recover almost completely from strain-induced distortion. The irreversibility of the permanent chemical cross-linking, on the other hand, make the material difficult to reprocess or reuse[3]. Because of their high elasticity and processing benefits[4;5], thermoplastic elastomers (TPEs) are currently a preferred substitute to thermoset materials. Noncovalent interactions, including as hydrogen bonding[6], ionic bonding[7;8], and metal-ligand coordination[9], have been used to increase the performance of TPEs. However, the permanent set after deformation remains a key challenge to solve in order to achieve tough TPEs with the same property as thermoset materials.

TPEs are structurally divided into two groups: block copolymers and their blends, both of which contain hard and soft phases in their microstructure. Hard and soft segments along the backbone chain of the polymers develop by microphase separation in block copolymer (BCP)-based TPEs, resulting in hard segmental domains and soft segmental domains, respectively. Soft-segmental rubbery domains (soft matrix) extend in response to strain-induced deformation, whereas hard-segmental glassy domains (hard domains) produce the physical cross-links

required for elastic recovery. To make a robust TPE with little residual strain, the TPE's polymer network must recover almost completely after deformation; consequently, it is worthwhile to investigate the nanoscale structural changes in TPEs during deformation.

Many studies used small angle X-ray scattering (SAXS)[10;11;12;13;14;15], Fourier transform infrared spectroscopy (FT-IR)[16;17;18;19], and transmission electron microscopy to investigate the deformation of BCP-based TPEs (TEM)[14;20;21;22;23;13;24]. They revealed that when BCP-based TPEs were stretched, spherical hard domains were deformed and orientated from an isotropic structure, which exhibited a meaningful association to stress relaxation and fracture of the stretched TPE. SAXS[15] and TEM[14] also revealed that affine deformation occurs in a fully deformed lattice constituted of hard domains when the plane spacing grows proportionately. However, the distribution and evolution of stress, which is a major issue in deformed BCP-based TPEs, have yet to be identified by test procedures and must be explained by direct and real-time viewing methods. AFM-based nanomechanics have been developed in recent years to obtain nanomechanical mapping of soft materials, particularly BCPs[25]. This method allows the mechanical properties of the material surface, including the elastic modulus, adhesion, dissipation, and stiffness, to be simultaneously probed with nanometer resolution. We anticipate that this measuring approach will disclose basic difficulties regarding the deformation process of BCP-based TPEs.

The strain-induced change of microdomains in a TPE specimen composed of a SEBS triblock copolymer was the focus of this chapter. The morphological and mechanical development was seen in-situ using AFM nanomechanics. An inhomogeneous distribution of internal stress was found during stretching using elastic modulus mapping, resulting in deformation, relative displacement, and partial separation of the phase-separated structure.

3.2 Results

3.2.1 Tensile Behavior

The left part of Fig. 3.1 depicts a typical strain-stress curve of TPE obtained from a strain-rate controlled tensile test. Unsurprisingly, when the specimen recovered to zero stress after being stretched to a strain of 200%, a residual strain (∼10%) was formed. The specimen's elastic modulus was determined to be ∼3.2 MPa based on the average slope of the elastic section of the stress-strain curves, which corresponded to strains ranging from 2% to 4%.

In a macroscopic view, the right part of Fig. 3.1 depicts the stress-time curve of the TPE extended to 50%. During a 12-hour period with a fixed 50% strain, tension reduced fast at the start of relaxation (≤1 hour) and then gradually declined with subsequent relaxation. This stress-relaxation process, as described above, implies that some significant structural evolution happened as the stretching period increased, and this structural evolution is thought to be connected to the material's failure to fully elastically recover.

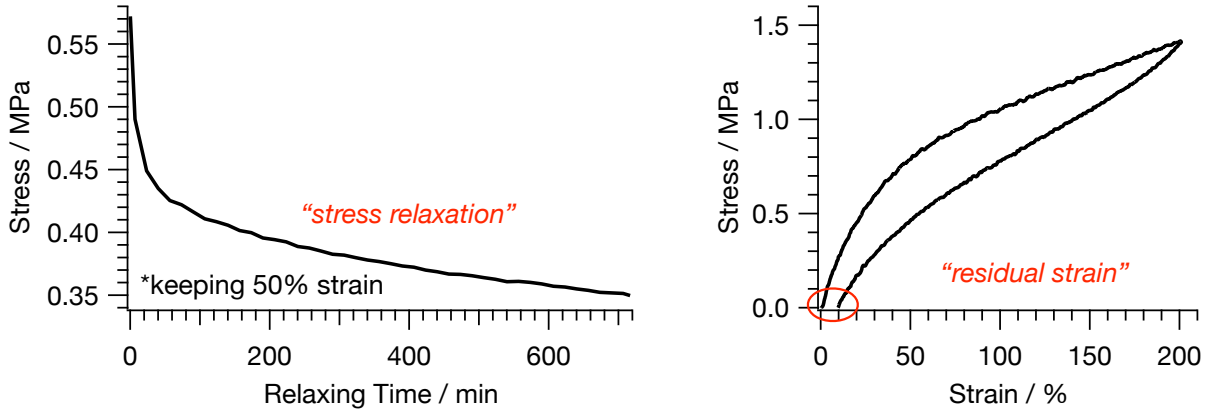

Figure 3.1: Two typical tensile curves for TPE.

3.2.2 AFM Nanomechanical Mapping

SEBS, a triblock copolymer made up of rigid poly(styrene)(PS) segments and poly(ethylene-co-butylene) (PEB) segments, has a phase-separated morphology and has had its nanomechanical

characteristics extensively researched[26;27;28;29;30;31]. Sphere-like PS domains with a high modulus, namely hard-segmental amorphous domains (hard domain), and PEB domains around the hard domains with a low modulus, namely soft-segmental rubbery matrix (soft matrix), were identified in the microstructure of a SEBS sample with a low PS component of 15%, as shown in elastic modulus map in Fig. 3.2. The color bar in the right can be used to estimate the associated elastic modulus values. Similarly, the deformation map depicts the indentation depth for AFM probe tip pushing the specimen surface.The hard domain and soft matrix in the deformation map correspond to low and high deformation regions, respectively, with their typical force-deformation curves (FCs) depicted in the left. Because of the softness of the SEBS with a low PS content, the overlaid elastic theoretical curves accurately duplicate each FC in the retraction section. With values of 4.6 nm, 290 pN, and 8.5 MPa, the FC from the hard domain suggests a low deformation, low adhesive force, and high elastic modulus during the tip-surface interaction. In contrast, with values of 9.4 nm, 435 pN, and 4.3 MPa, respectively, the FC from the soft matrix suggests a high deformation, high adhesive force, and low elastic modulus. Because the influence of the soft matrix beneath the surface could not be avoided, the measured elastic modulus from the hard domain did not reflect its actual value. The neighboring soft matrix buffered the hard domain's deformation, resulting in a lower value.

We firstly have a comparison of elastic modulus maps before and after elongation, as shown in Fig. 3.3. The left part is the modulus map of unstretched TPE as described before. The right part is the stretched TPE with keeping 0.5 strain for 262 minutes. The bottom part are the value distribution of two elastic modulus maps. Although they are in different areas of the same sample, from the value distribution of modulus, we could clearly see a right shift of the modulus after stretching, which means the elastic modulus of the sample has increased after stretching. Furthermore, the peak of the left histogram in appears at $\sim$3.50 MPa, which agrees with the elastic modulus calculated from the strain-stress curve ($\sim$3.2 MPa). However, consistency, which is affected by the tip radius and pushing force and has a strong relationship with the amount of sample deformation[32], could only be achieved through a very delicate operation. The elastic modulus obtained from tensile testing reflected the soft matrix's initial elastic deformation. The elastic modulus obtained from AFM increased in value as the sample

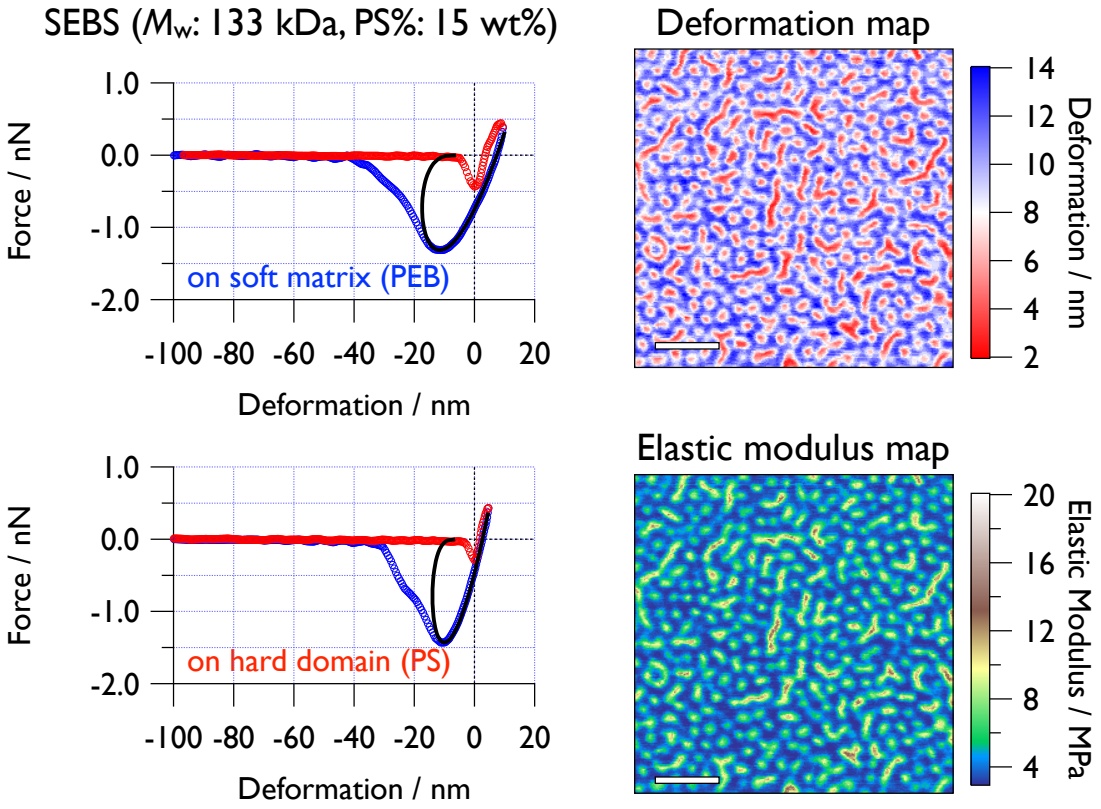

Figure 3.2: (Left) Typical force-deformation curves on hard domain and soft matrix with superimposed elastic theoretical curves. (Right) Deformation and elastic modulus maps of TPE. Scale bar, 100 nm.

underwent additional deformation because the surrounding hard domains were involved when the soft matrix deformed.

Then, if we binarize these two maps to pick up 15% high modulus area, which is the ratio of hard domain, we could obtain the domain numbers in each map, as shown in Fig. 3.4 After elongation, the domain number decrease compared with the unstretched sample. This result could be explained by this illustration that some hard domains get closer in x direction and fused after elongation, as described in Chapter 1.

The nanostructural change depicted in Fig. 3.1 was revealed using AFM nanomechanics. Although the stress decreased rapidly during the initial stage of stretching, which is considered appropriate for study, imaging during this stage was extremely difficult because the sample drifted significantly at the nanoscale. This situation improved approximately 3 hours after we began stretching, and we obtained clear images between 4 and 10 hours. The elastic modulus maps of the TPE stretched 50% that was probed at nearly the same region after 262 and 597

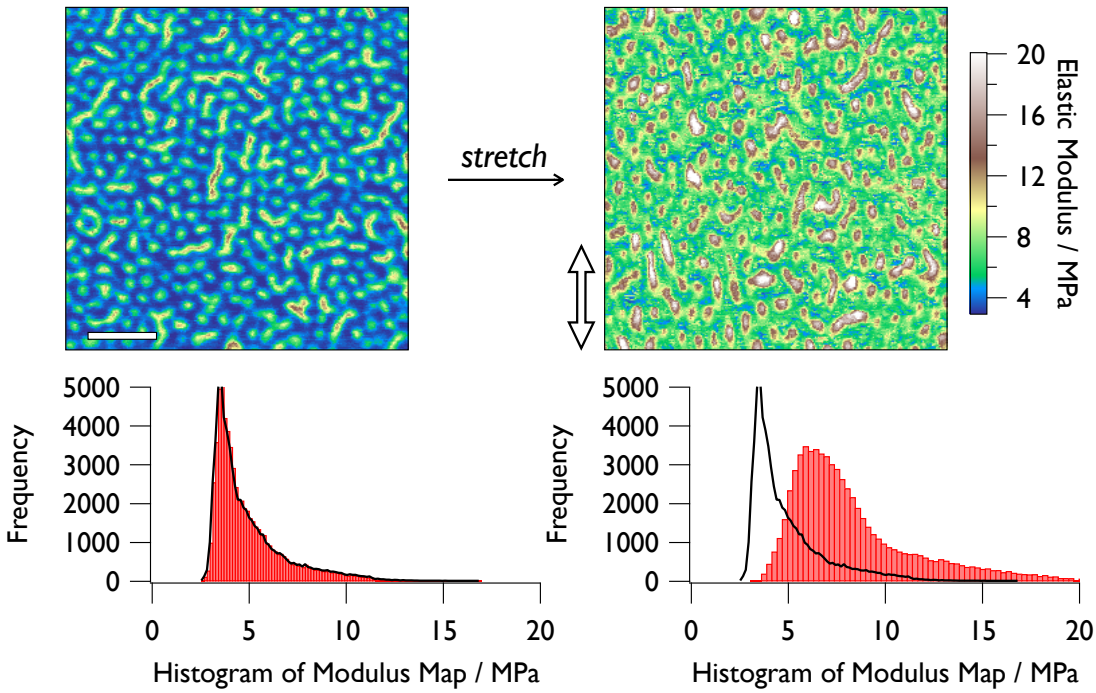

Figure 3.3: The elastic modulus map and its value distribution of (left) unstretched sample and (right) strecthced sample which is kept 0.5 strain for 262 min. Scale bar, 100 nm.

minutes are shown in Fig. 3.5. The stretching direction is represented by the double-headed arrows. Hard domains deformed and oriented parallel to the stretching direction per a comparison with Fig. 3.2, which is a similar result to those reported by SAXS[15] and TEM analyses[13]. Utilizing a two-dimensional (2D) fast Fourier transform (FFT) algorithm implemented in ImageJ, the average separation distance between the hard domains was extracted from each obtained modulus map, as shown in Fig. 3.6. The distance between the hard domains in the unstretched TPE was approximately 23 nm regardless of direction. Interestingly, in the stretched TPE,

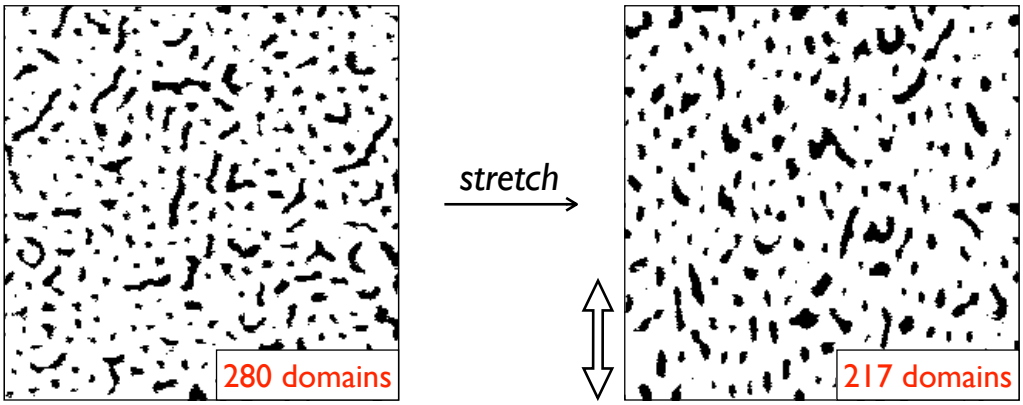

Figure 3.4: Binarized modulus maps and statistics on the number of hard domains.

the average distance of the hard domains in the stretching direction increased from ∼41 nm to ∼38 nm after 262 minutes and decreased from ∼41 nm to ∼38 nm after 597 minutes. At the same time, there was almost no change in the average distance perpendicular to the stretching direction.

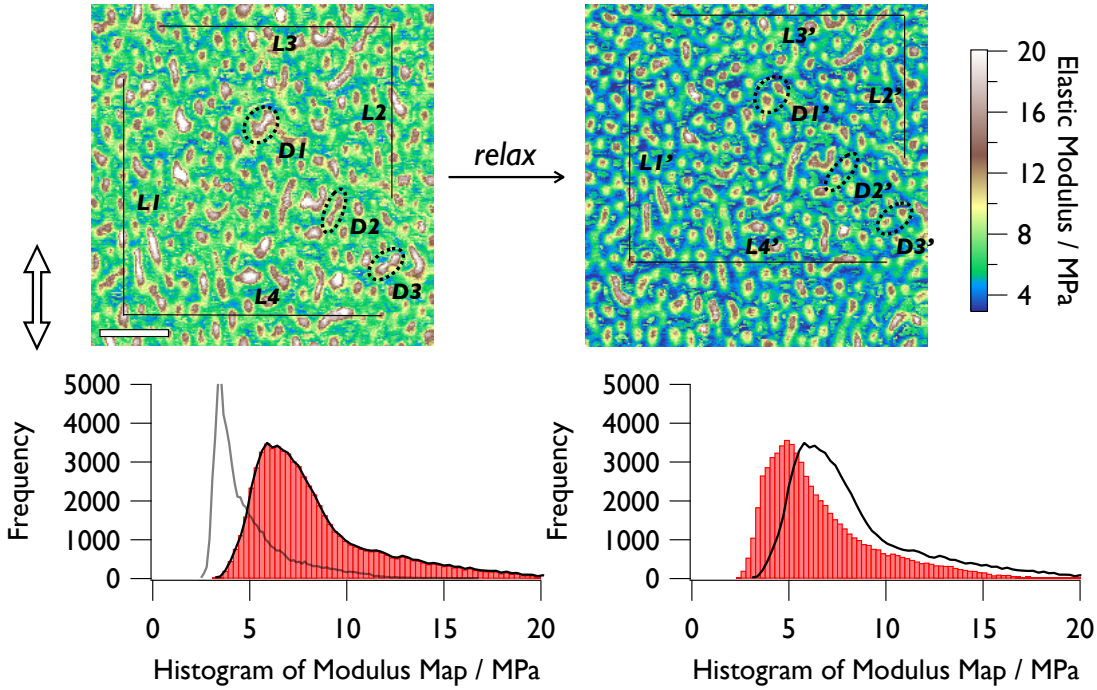

Figure 3.5: The elastic modulus map and its value distribution of strecthced sample which is kept 0.5 strain for (left) 262 min and (right) 597 min. Scale bar, 100 nm.

It is also worthwhile to discuss the modulus distribution of the sample during deformation. The histograms in Fig. 3.3 represent the modulus distribution before and after stretching, respectively, and show peak values of ∼3.50 MPa and ∼4.84 MPa, indicating that the elastic modulus increased after stretching to a strain of 0.5. Furthermore, when compared to the unstretched sample, an increased proportion of the elastic modulus distribution occurred in the high modulus area in the stretched TPE, which was attributed to the formation of a stress chain. In general, a stress chain in BCP-based TPEs is made up of soft matrices within a deformed portion of the material that are held together to form a stress network with hard domains as junction points. As a result of the stress network's contribution, the elastic modulus of some soft matrices increased, resulting in a nonuniform distribution.

With increasing stretching time, the peaks shifted to the left (from ∼5.7 MPa to ∼4.8 MPa), indicating a decrease in the elastic modulus in TPE, as indicated by the color change from left

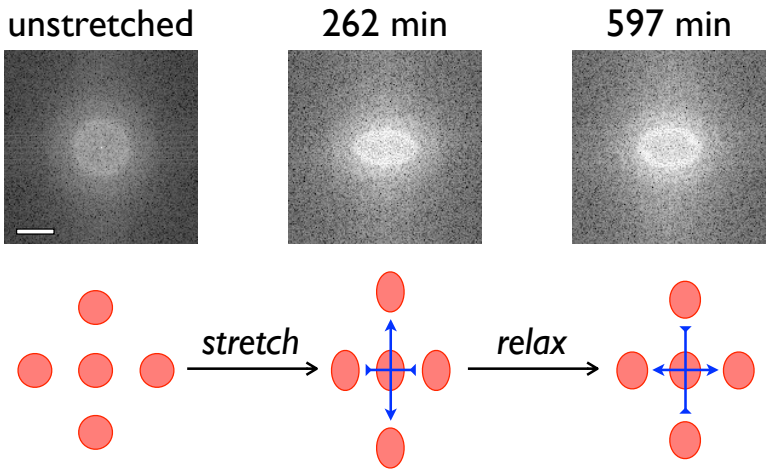

Figure 3.6: (Top) 2D FFT images extracted from obtained modulus maps. Scale bar, 0.1 nm^{-1}. (Bottom) Schematic diagram of the spacing between hard domains when the material is stretched and relaxed.

to right. A modulus decrease is consistent with the tensile test results, as shown in Fig. 3.1. However, the stress decrease in the TPE stretched 50% obtained in the macroscopic stress-time curve, as shown in Fig. 3.1, is ~0.03 MPa from 4 hours to 10 hours, which is much less than the result obtained from AFM (decrease of ~0.9 MPa). A future study will be carried out to estimate the macroscopic stress value from the microscopic change in the elastic modulus in the tensile state.

It was further found that a relative displacement of the hard domains occurs in the stretching direction. We measured the distance between the hard domains distributed parallel and perpendicular to the stretching direction at different relaxation times. In the direction parallel to the stretching direction, as shown in Fig. 3.5, L1 (~398 nm) and L2 (~250 nm) in the left were significantly shortened to L1' (~299 nm) and L2' (~211 nm) in the right; however, L3 (~340 nm) and L4 (~377 nm) in the direction perpendicular to the stretching direction maintained almost the same value as L3' (~339 nm) and L4' (~374 nm). Shrinkage in such a local area along the stretching direction, which should not have happened during a fixed strain relaxation, indicates a nonuniform change in the polymer network within the material. This conclusion could also be drawn from the previous discussion of the hard domain morphology. The average separation distance between the hard domains after 262 minutes of stretching (~41 nm) indicated a 78% elongation compared to the unstretched hard domains (~23 nm) at 50%

of the macroscopic deformation, indicating that other areas were stretched less than 50%.

Despite the fact that the majority of the material retained its morphology, some hard domains separated significantly during the relaxation process, as shown by the marked dotted circles in Figs. 3.5; these areas represent the same hard domains in the microstructure with a different stretching time. A polymer network, also known as a bridge chain, was formed structurally by amorphous hard domains acting as junction points and rubbery soft matrixs bridging these junction points[33]. When a macroscopic strain was applied, the bridge chains stretched first because the hard domains were relatively hard, resulting in an increase in local stress. A local stress in a polymer can be transferred along a stress network. As a result, in order to relieve the local stress, the stretched bridge chains exerted a strong force on the hard domains, causing them to deform and separate at the weak junctions. The split hard domains formed new stress networks, which meant that bridge chains that were previously assigned to one junction point were now assigned to two junction points. Furthermore, if the subordinated hard domain was split into two new domains, the chains that originally belonged to only one hard domain, known as a loop chain, could evolve into a bridge chain. The deformation, separation, and reorganization of microdomains, as well as the stress network, partially reformed the polymer's microstructure. The domain deformation was relatively easy to recover; however, the topological change caused by separation had a long-term impact on the material, and residual strain was present. In a future work that incorporates data assimilation and simulation, a dynamic stress network will be visualized and explored[34].

3.2.3 Dynamic Stress Network

Using continuous AFM observations over a short time period, we investigated the details of the separation behavior. As shown in Fig. 3.7, we chose one hard domain, D1 in 289 min, whose separation was observed as described above, and studied the structural evolution surrounding it before and after the separation. A small hard domain, denoted as D2, grew from 289 to 298 minutes, which could be explained by the aggregation of hard PS segments, and continued to grow at the times shown in 307 and 317 minutes. The elastic modulus of domain D2

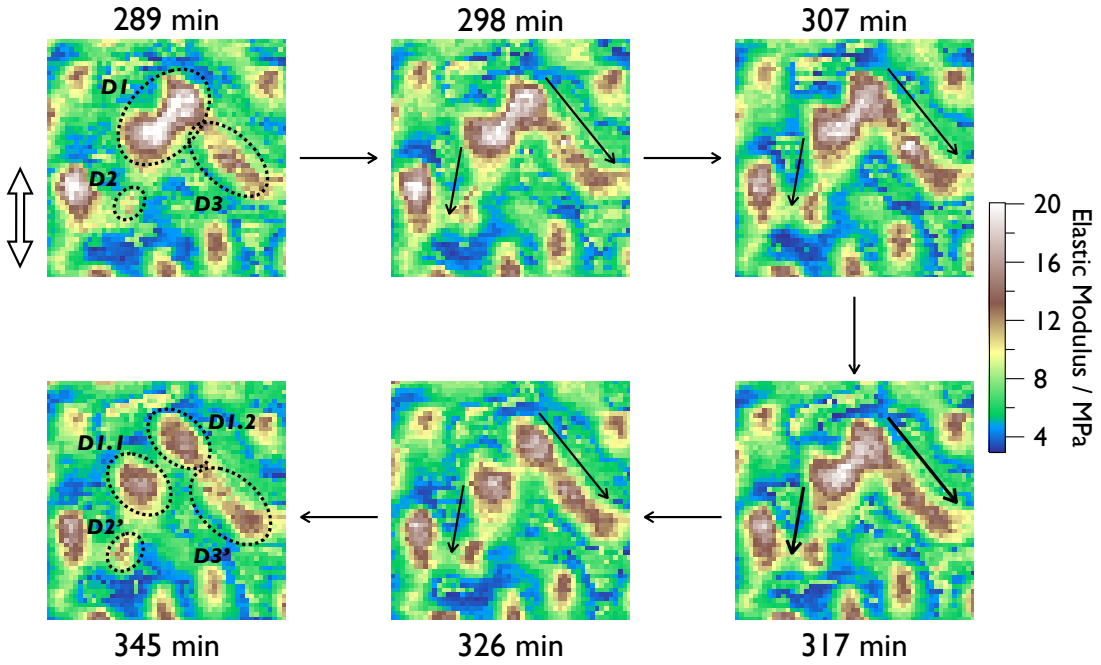

Figure 3.7: Dynamic stress network observed in stretching TPE. Image size, 100 nm.

and its surroundings, which included the area between domains D2 and D1, increased as a result of this growth behavior. The newly formed bridge chains between D1 and D2 gradually separated the soft matrix in the interval of domains D2 and D1. This strain-induced structural evolution resulted in the formation of a new connection between domains D2 and D1 within the soft matrix, known as a stress chain. The stress chain between domains D1 and D3 also had an effect. The arrow in 289-326 min indicates the direction of the stress chain generated by domains D2 and D3. Finally, domain D1 began to split into two smaller hard domains, domain D1.1 and D1.2, that moved away from each other after 345 min of continuous stress from two directions. For the first time, the aggregation and separation of the hard domains, as well as the subsequent generation of stress chains and dynamic changes in the stress network, were observed. The dynamic evolution of the stress network described above is not accidental; besides this region, this phenomenon was also found in other regions in the same time frame, as shown in Fig. 3.8. This overall behavior eventually also leads to a permanent change in the network topology, which in turn causes the annihilation of the stresses in this process, eventually manifesting itself in a macroscopic stress-relaxing behavior.

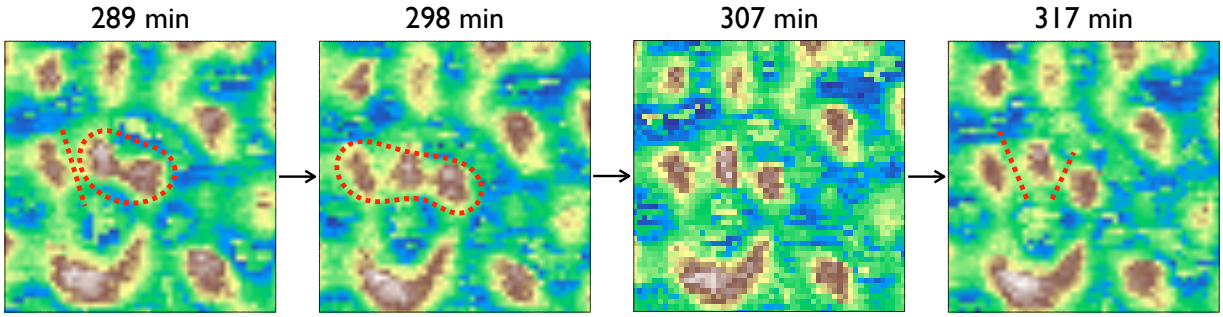

Figure 3.8: Dynamic stress network observed in another region. Image size, 100 nm.

3.3 Summary

This study visualized the strain-induced evolution of the structure and mechanical properties of a SEBS-based TPE material using AFM nanomechanics. Microdomains in the stretched SEBS exhibited deformation, separation, and reorganization during the stress relaxation process, according to the nanoscale elastic modulus maps. The stress network underwent dynamic evolution, which permanently altered the polymer's topological structure. An atomic force microscope was used to take continuous images of the polymer microstructure during deformation, which could be a powerful approach for understanding the continuous morphological changes of various materials under the action of external forces. Furthermore, the deterioration mechanism of polymer materials can be studied further using a combination of mathematical modeling, molecular dynamics simulation, and experimentation. These basic microscopic studies provide the theoretical foundation for the development of high-strength polymer materials. Based on this new technique, more research on polymer morphology will be conducted in the future. The content of this chapter is based on the authors' published paper[35] with additional explanations.

3.4 References

[1] Bhowmick, A. K. & Stephens, H. *Handbook of elastomers* (CRC Press, 2000).

[2] Shanks, R. A. & Kong, I. General purpose elastomers: structure, chemistry, physics and performance. *Advances in Elastomers I* 11–45 (2013).

[3] Akiba, M. a. & Hashim, A. Vulcanization and crosslinking in elastomers. *Progress in polymer science* **22**, 475–521 (1997).

[4] Spontak, R. J. & Patel, N. P. Thermoplastic elastomers: fundamentals and applications. *Current opinion in colloid & interface science* **5**, 333–340 (2000).

[5] Drobny, J. G. *Handbook of thermoplastic elastomers* (Elsevier, 2014).

[6] Kautz, H., Van Beek, D., Sijbesma, R. P. & Meijer, E. Cooperative end-to-end and lateral hydrogen-bonding motifs in supramolecular thermoplastic elastomers. *Macromolecules* **39**, 4265–4267 (2006).

[7] Datta, S., Bhattacharya, A., De, S., Kontos, E. & Wefer, J. Reinforcement of epdm-based ionic thermoplastic elastomer by precipitated silica filler. *Polymer* **37**, 2581–2585 (1996).

[8] Datta, S., De, S., Kontos, E. & Wefer, J. Ionic thermoplastic elastomer based on maleated epdm rubber. i. effect of zinc stearate. *Journal of applied polymer science* **61**, 177–186 (1996).

[9] Rieth, L. R., Eaton, R. F. & Coates, G. W. Polymerization of ureidopyrimidinone-functionalized olefins by using late-transition metal ziegler–natta catalysts: Synthesis of thermoplastic elastomeric polyolefins. *Angewandte Chemie* **113**, 2211–2214 (2001).

[10] Inoue, T., Moritani, M., Hashimoto, T. & Kawai, H. Deformation mechanism of elastomeric block copolymers having spherical domains of hard segments under uniaxial tensile stress. *Macromolecules* **4**, 500–507 (1971).

[11] Séguéla, R. & Prud'Homme, J. Affinity of grain deformation in mesomorphic block polymers submitted to simple elongation. *Macromolecules* **21**, 635–643 (1988).

[12] Prasman, E. & Thomas, E. L. High-strain tensile deformation of a sphere-forming triblock copolymer/mineral oil blend. *Journal of Polymer Science Part B: Polymer Physics* **36**, 1625–1636 (1998).

[13] Honeker, C. C. *et al.* Perpendicular deformation of a near-single-crystal triblock copolymer with a cylindrical morphology. 1. synchrotron saxs. *Macromolecules* **33**, 9395–9406 (2000).

[14] Cohen, Y., Albalak, R. J., Dair, B. J., Capel, M. S. & Thomas, E. L. Deformation of oriented lamellar block copolymer films. *Macromolecules* **33**, 6502–6516 (2000).

[15] Tomita, S. *et al.* Strain-induced deformation of glassy spherical microdomains in elastomeric triblock copolymer films: simultaneous measurements of a stress–strain curve with 2d-saxs patterns. *Macromolecules* **50**, 677–686 (2017).

[16] Zhao, Y. Structural changes upon annealing in a deformed styrene-butadiene-styrene triblock copolymer as revealed by infrared dichroism. *Macromolecules* **25**, 4705–4711 (1992).

[17] Sakurai, S., Sakamoto, J., Shibayama, M. & Nomura, S. Effects of microdomain structures on the molecular orientation of poly (styrene-block-butadiene-block-styrene) triblock copolymer. *Macromolecules* **26**, 3351–3356 (1993).

[18] Kraus, G. & Rollmann, K. Effects of domain and molecular orientations on the mechanical properties of a styrene-butadiene block polymer. *Journal of Macromolecular Science, Part B: Physics* **17**, 407–425 (1980).

[19] Duan, Y. *et al.* Deformation behavior of sphere-forming trifunctional multigraft copolymer. *Macromolecules* **41**, 4565–4568 (2008).

[20] Odell, J. & Keller, A. Deformation behavior of an s-b-s copolymer. *Polymer Engineering & Science* **17**, 544–559 (1977).

[21] Yamaoka, I. & Kimura, M. Effects of morphology on mechanical properties of a sbs triblock copolymer. *Polymer* **34**, 4399–4409 (1993).

[22] Yamaoka, I. Effects of morphology on mechanical properties of styrene-butadiene-styrene triblock copolymer/methyl methacrylate styrene copolymer blends. *Polymer* **37**, 5343–5356 (1996).

[23] Yamaoka, I. Anisotropic behaviour of styrene-butadiene-styrene triblock copolymer/methyl methacrylate-styrene copolymer blends. *Polymer* **39**, 1081–1093 (1998).

[24] Shi, W. *et al.* Mechanics of an asymmetric hard–soft lamellar nanomaterial. *ACS nano* **10**, 2054–2062 (2016).

[25] Nakajima, K. *et al.* Nano-palpation afm and its quantitative mechanical property mapping. *Microscopy* **63**, 193–208 (2014).

[26] McLean, R. S. & Sauer, B. B. Tapping-mode afm studies using phase detection for resolution of nanophases in segmented polyurethanes and other block copolymers. *Macromolecules* **30**, 8314–8317 (1997).

[27] Han, X., Hu, J., Liu, H. & Hu, Y. Sebs aggregate patterning at a surface studied by atomic force microscopy. *Langmuir* **22**, 3428–3433 (2006).

[28] Wang, D., Fujinami, S., Liu, H., Nakajima, K. & Nishi, T. Investigation of true surface morphology and nanomechanical properties of poly (styrene-b-ethylene-co-butylene-b-styrene) using nanomechanical mapping: Effects of composition. *Macromolecules* **43**, 9049–9055 (2010).

[29] Wang, D., Fujinami, S., Nakajima, K. & Nishi, T. True surface topography and nanomechanical mapping measurements on block copolymers with atomic force microscopy. *Macromolecules* **43**, 3169–3172 (2010).

[30] Wang, D. *et al.* Characterization of surface viscoelasticity and energy dissipation in a polymer film by atomic force microscopy. *Macromolecules* **44**, 8693–8697 (2011).

[31] Wang, D. *et al.* Characterization of morphology and mechanical properties of block copolymers using atomic force microscopy: Effects of processing conditions. *Polymer* **53**, 1960–1965 (2012).

[32] Sun, S., Wang, D., Russell, T. P. & Zhang, L. Nanomechanical mapping of a deformed elastomer: visualizing a self-reinforcement mechanism. *ACS Macro Letters* **5**, 839–843 (2016).

[33] Matsumiya, Y., Watanabe, H., Takano, A. & Takahashi, Y. Uniaxial extensional behavior of (sis) p-type multiblock copolymer systems: Structural origin of high extensibility. *Macromolecules* **46**, 2681–2695 (2013).

[34] Morita, H., Miyamoto, A. & Kotani, M. Recoverably and destructively deformed domain structures in elongation process of thermoplastic elastomer analyzed by graph theory. *Polymer* **188**, 122098 (2020).

[35] Liu, H., Liang, X. & Nakajima, K. Direct visualization of a strain-induced dynamic stress network in a sebs thermoplastic elastomer with in situ afm nanomechanics. *Japanese Journal of Applied Physics* **59**, SN1013 (2020).

Chapter 4

Nanoscale Strain-Stress Mapping for the TPE

4.1 General

We previously reported on the development of in situ atomic force microscopy to explore the microphase splitting structure and elastic modulus of BCP-type TPEs in the continuously stretched state[1]. It demonstrated a correlation between the hard domain splitting observed under the microscope and the residual strain observed at the macroscopic level. Furthermore, we argue that the microscopic motion of the hard domains is driven by the visible stress network formed under strain. To understand the dynamic behavior of this network, in this work we employ image segmentation based on the Delaunay triangulation method for finite element analysis (FEA) of a series of in situ AFM images (Fig. 4.2). Microscopic strain-stress distribution maps are used to explain the reasons behind the dynamic evolution of the network structure in BCP-type TPEs.

We were inspired by the work of Jinnai et al.[2], who performed in situ TEM experiments on filled rubber and evaluated the local strain of the material by Delaunay triangulation of the filler particles. In this work, all image processing methods were based on a self-developed Matlab program. The TPE used in this experiment contains a 15 wt% proportion of hard segments;

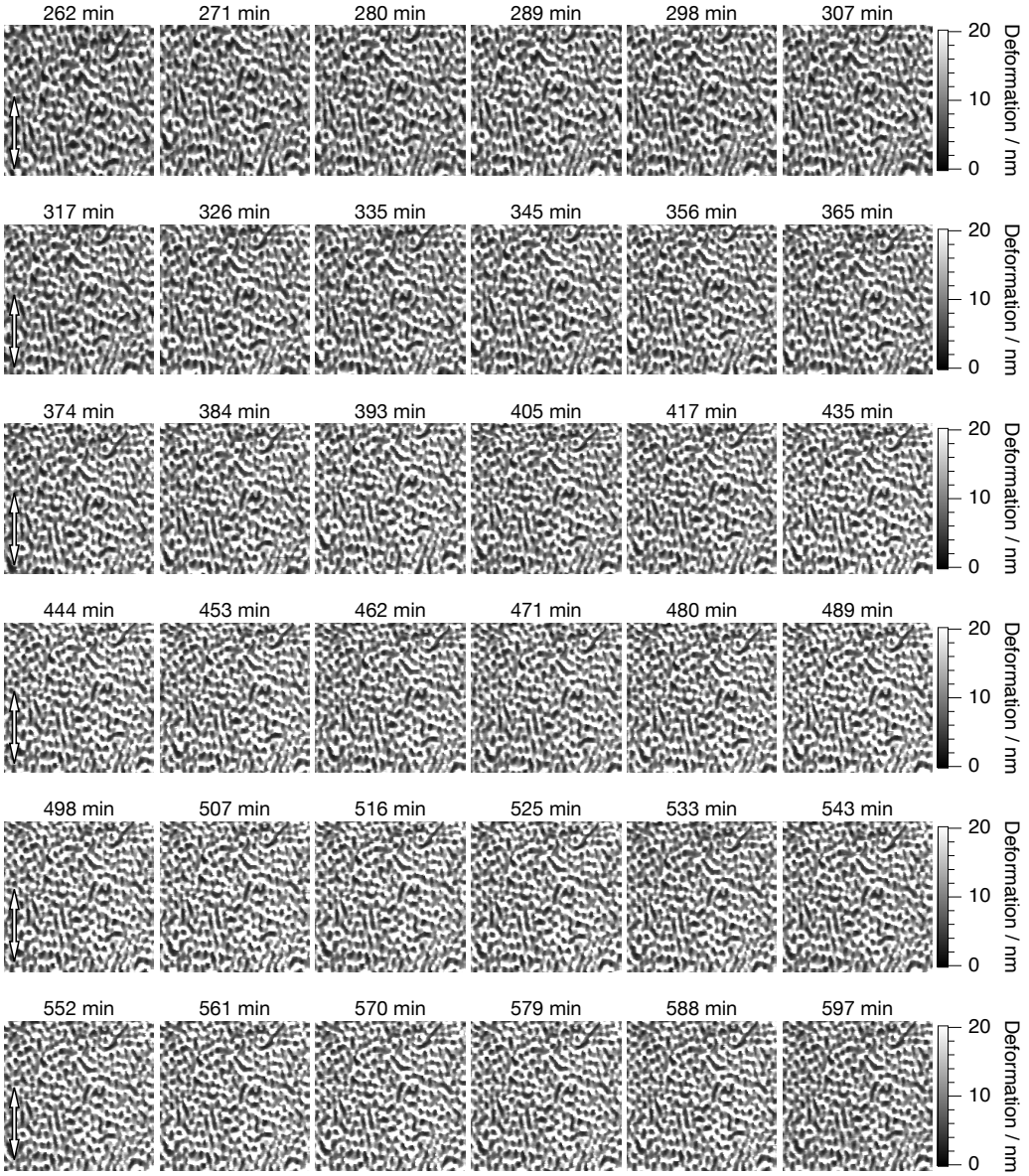

Figure 4.1: AFM deformation maps captured from different relaxing time (Image size: 500 nm), where the observed regions are approximately the same.

therefore, in the AFM deformation map, the small 15% deformation region is considered as a hard phase, which naturally yields a discontinuous set of domains. The geometric center of each domain is chosen as a representative point. the Delaunay triangulation algorithm is modified by Matlab syntax for AFM image processing (Fig. 4.3). Since the Delaunay mesh uses the nearest neighbor rule, the automatically generated mesh is reconstructed accordingly, so that triangles from different images can correspond exactly. The calculation of the individual triangle deformations is shown in Fig. 4.4, which is often used during FEA. linear strains in the x (ε_x) and y (ε_y) coordinates can be derived separately using the strains of the respective

triangles. Note that in all figures, the macroscopic stretching direction is parallel to the y coordinate. To further explore the variation of the nanomechanical properties in the observed regions, the Delaunay mesh obtained from the deformation maps was used to delineate the regions on the corresponding modulus maps so that the modulus variation in each triangle could be evaluated. The median value of the soft matrix modulus in each triangle is taken as the representative modulus. The stress transfer in the network brings about a change in the modulus in the local region; therefore, we treat this change as the nano stress (ΔE) in each triangle.

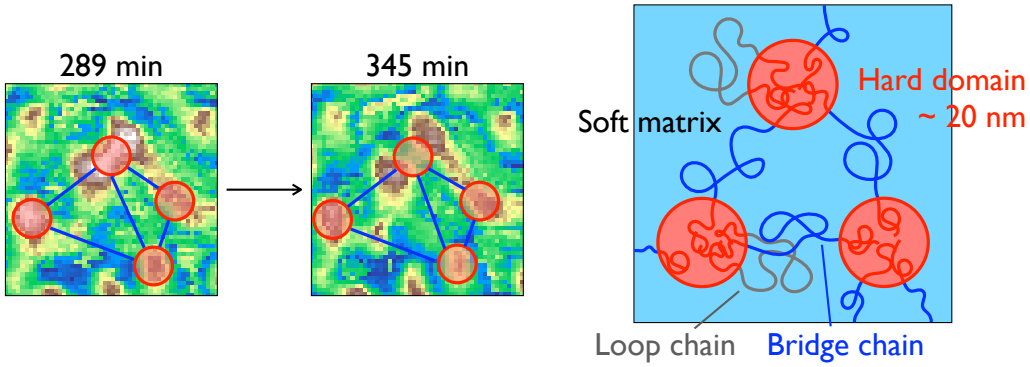

Figure 4.2: Basic FEA principle for AFM images.

As mentioned earlier, potential BCPs for TPE applications must feature a discontinuous microphase-separated structure in the form of spheres or cylinders, which makes the hard phases therein very suitable for abstraction into two-dimensional point sets to provide triangulation treatment. The microstructure of BCP-type TPE is shown schematically in Fig. 4.2. Hard segments of BCP are aggregated into the domain, while soft segments form the bridge chain and loop chain during the packing of the hard domain, which together form the soft matrix. Although how the loop chain affects material's mechanical properties has not been completely solved[3;4], most researchers believe the network formed by bridge chains bears and transmits the stress generated during the material deformation[5;6;7], namely stress network. Fig. 4.3 is a typical AFM deformation map of a TPE captured after holding 50% elongation for 570 min. The details of the experiments have been described in the previous report[1]. We built the Delaunay mesh using the geometric center of each small-deformed hard domain, as shown in Fig. 4.3. Since all captured maps are in similar regions, a series of comparable Delaunay meshes can be generated by this method.

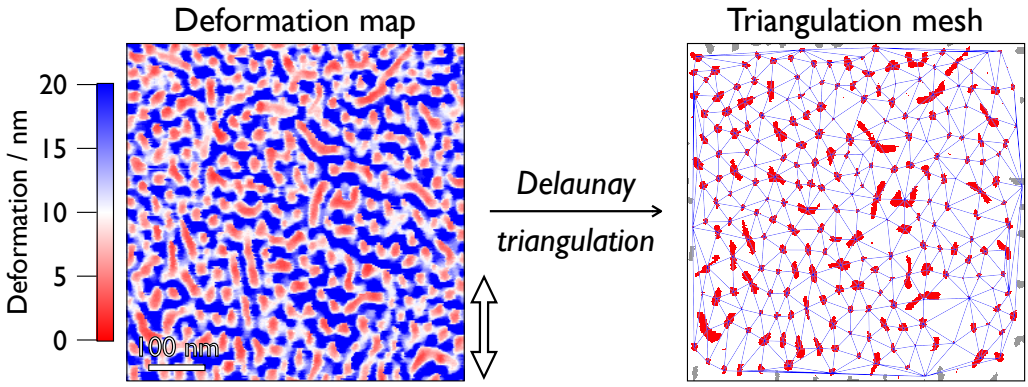

Figure 4.3: (Left) A typical AFM deformation map of BCP-type TPE in the tensile state. The arrow indicates the stretching direction. (Right) Schematic diagram of the Delaunay triangulation.

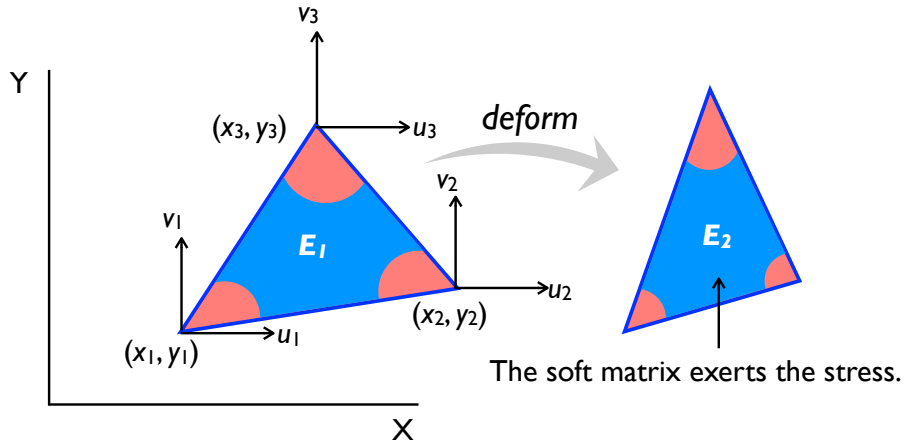

Figure 4.4: Notations for the three-node triangle and the schematic diagram of its deformation.

4.2 Results

4.2.1 Micro Behavior of the Stress-Relaxing Process

Let's first look at the whole stress relaxation process. It is well known that the stress in a TPE decreases when a fixed elongation is maintained[8], and this phenomenon can be observed at the microscopic level. As shown in Fig. 4.5, we plot the average modulus of the soft matrix for each capture during stress relaxation. The modulus undergoes an approximately exponential decay until 400 min, after which it slows down and gradually stabilizes after 500 min.

Things get interesting when we analyze the relationship between the soft matrix modulus and the number of hard domains. Note that the hard domains are the small deformation regions

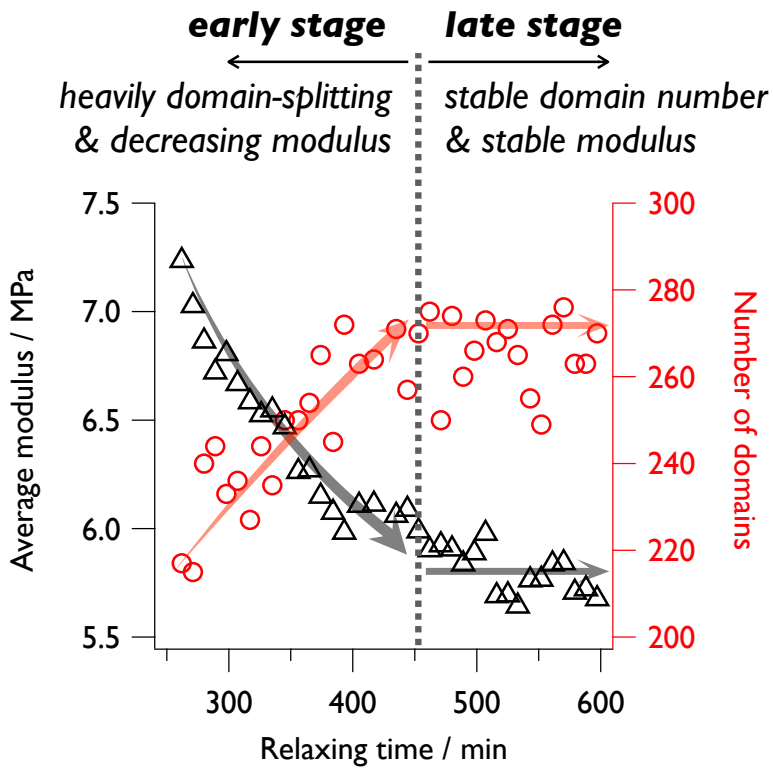

Figure 4.5: Correlation between the average AFM modulus, the number of hard domains, and the relaxing time.

in the AFM deformation map, where we remove the incomplete domains at the edges of the image. During the early relaxation, the number of hard domains increases rapidly as the soft basis modulus decreases. Then, after 500 min, the number of domains and the soft matrix modulus stabilize simultaneously. Although the data at some time points are biased due to some misalignment of the observation area, we can establish a sufficient correlation between the decrease in modulus and the increase in the number of lattices. The increase in the number of domains, i.e., the splitting of some domains, is a finding that is well documented in both experiments[1] and simulations[6;9]. On the other hand, the decrease in modulus of soft substrates is usually considered to be due to the loss of stress tolerance of the bridge chains, accompanied by splitting from the hard phase to form ring chains or pulling out to form dangling chains[10;11]. Also, the higher domain density and closer spacing due to splitting may contribute to the stress relaxation in the bridge chains. The above statement is very reasonable; however, studying the relationship between the kinetic and physical properties of such polymer networks is almost only possible through simulations, which makes us eager to observe these phenomena experimentally.

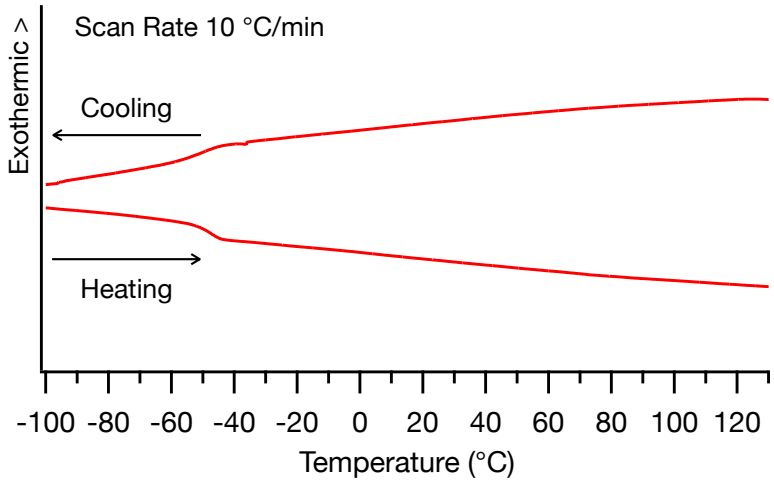

Figure 4.6: DSC profile of SEBS-15.

In fact, the decreasing trend of the modulus under the microscope does not correspond to the macroscopic stress-relaxation curve in the same time period, but is closer to the beginning of the macroscopic relaxation, as shown in Fig. 3.1. Therefore, another concern here is whether the inconsistency in macroscopic and microscopic behavior is due to the difference in temperature. In the AFM experiment, the temperature inside the cavity increased slightly compared to room temperature due to the fact that the sample was in a closed, soundproof container during the scan. The temperature was 27.3 ℃ at the beginning of the scan, i.e. after 262 min of relaxation, while it increased to 28.7 ℃ after 597 min. Compared to the standard room temperature at which the tensile test was performed (25 ℃), we were not able to determine whether this temperature difference could bring about an appreciable change in the sample properties. In addition, as shown in the Fig. 4.6, in the differential scanning calorimetry (DSC) measurement of this sample, we did not succeed in observing the glass transition process due to the hard PS phase, as the PS content was only 15%. In future experiments, we will further develop the in situ AFM test at variable temperature to demonstrate the effect of temperature on AFM measurement of TPE.

It is also worth mentioning that in another set of experiments, at a similar relaxing time, we also observed slightly different results than in Fig. 4.5. As shown in Fig. 4.7, there is a recovery of the modulus rising after the initial decrease, which indicates that the observation of the tiny region of 500 nm produces different results depending on the observation area, and

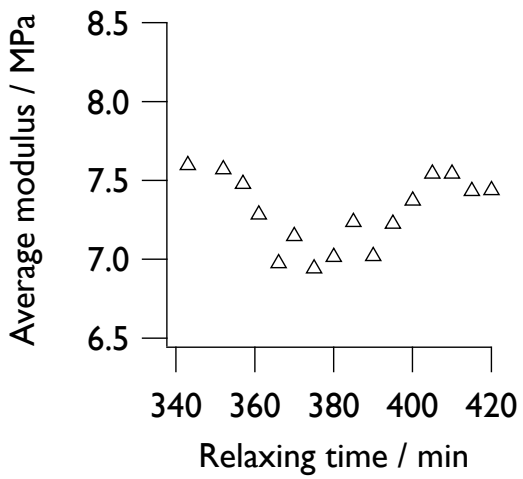

Figure 4.7: Relaxing time versus soft matrix modulus in another set of data.

we believe that this is one of the possible reasons for the inconsistency between macroscopic and microscopic phenomena.

4.2.2 Finite Element Analysis

We chose two time points of early (262 to 326 min) and late (507 to 570 min) captures as the subjects of our study, respectively. As shown in Fig. 4.5, from 262 to 326 min, the soft matrix modulus decreases rapidly and the hard domain splits severely, while from 507 to 570 min, the modulus and the number of domains remain relatively stable. Fig. 4.8 shows the changes of deformation and modulus in the same region in the early stage. Although there is a high degree of similarity between the images before and after the one-hour relaxation, the motion of each particular hard domain can be amplified by triangulation. Negative strain, i.e., shrinkage, occurs in most of the grid region along the stretch direction, with an average value of -6.4% for all $varepsilon_y$. As an experiment with fixed elongation throughout, such negative strain values require splitting the hard phase to compensate for the new area caused by shrinkage. Admittedly, there are still regions where positive strain occurs and appear to show a hierarchical structure along the x-direction, as indicated by the purple band in the figure. A similar heterogeneous behavior of the block copolymer has been demonstrated in the case of high elongation,[12;7], and we found that long-term maintenance of this behavior also occurs at low elongation rates of 50%. Moreover, during deformation, the TPE network

transfers externally applied stresses to each other through physical bridging points, i.e., using the hard domain as a medium, and also overcomes topological constraints that cause the mesh to develop mutually perpendicular strain trends in the x and y directions[13;14]. Such a trend can also be observed during the later relaxation process and we will discuss it later.

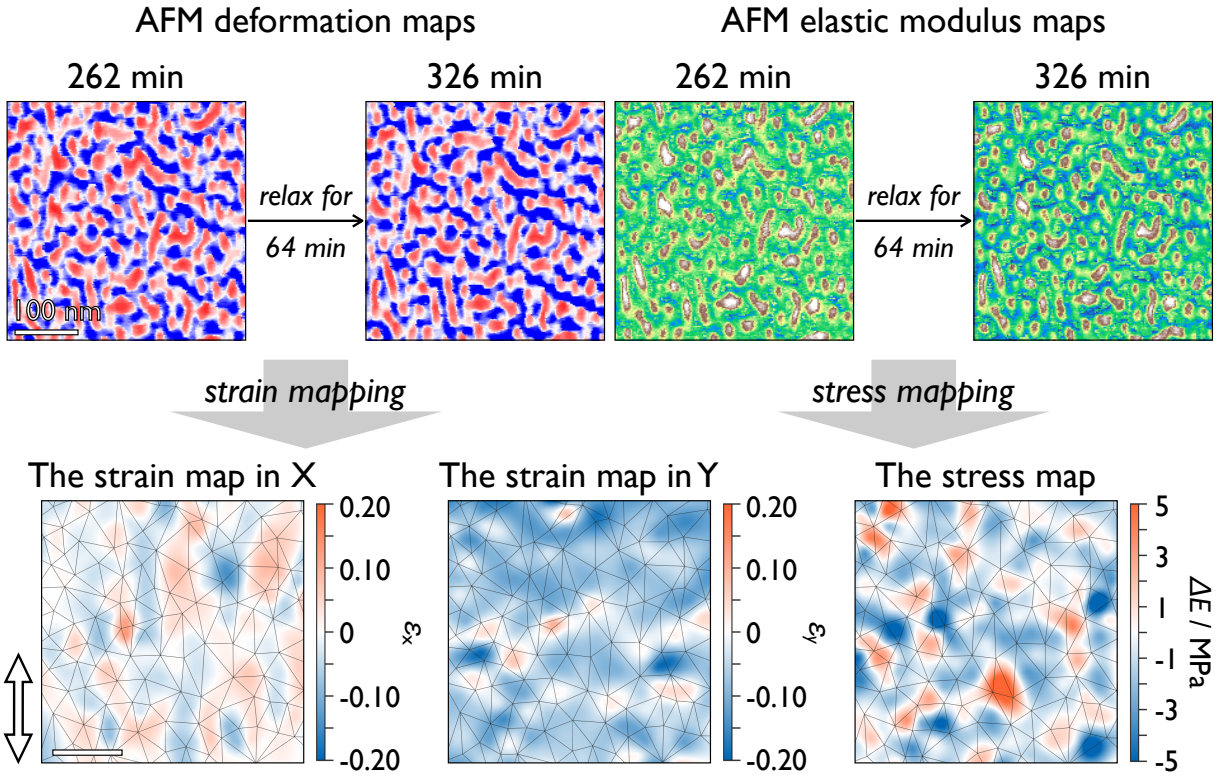

Figure 4.8: (Top) AFM deformation and modulus map of TPE after keeping elongation for 262 and 326 min. (Bottom) Linear-strain maps in the x and y coordinate derived from deformation maps with the stress map derived from modulus maps.

As shown in Fig. 4.9, we use a simple schematic diagram to explain the relationship between hard-domain splitting and local strain, although the realistic situation would be more complex. The external stretching deforms the hard domain and imposes stress on the bridge chain, while stretching the network in the y-direction and compressing it in the x-direction. After reaching the stress limit, the hard domain splits, and the bridge chain is then relaxed, causing a network recovery in the y-direction. Finally, the network in x-direction is also recovered due to the packing requirement. The above behavior makes the splitting of the hard domain does not have a large impact on the x-direction, and its average ε_x is only -0.2%. This result can also be related to the FFT analysis in Chapter 3. Comparing with Fig. 3.6, it can be found that the strain is mostly negative in the Y-direction parallel to the stretch, and the ellipse in the

FFT image has some recovery after relaxing, indicating that the domains' distances are also approaching each other. In contrast, in the X direction perpendicular to the tensile direction, there is no significant change in either the strain map or the FFT image.

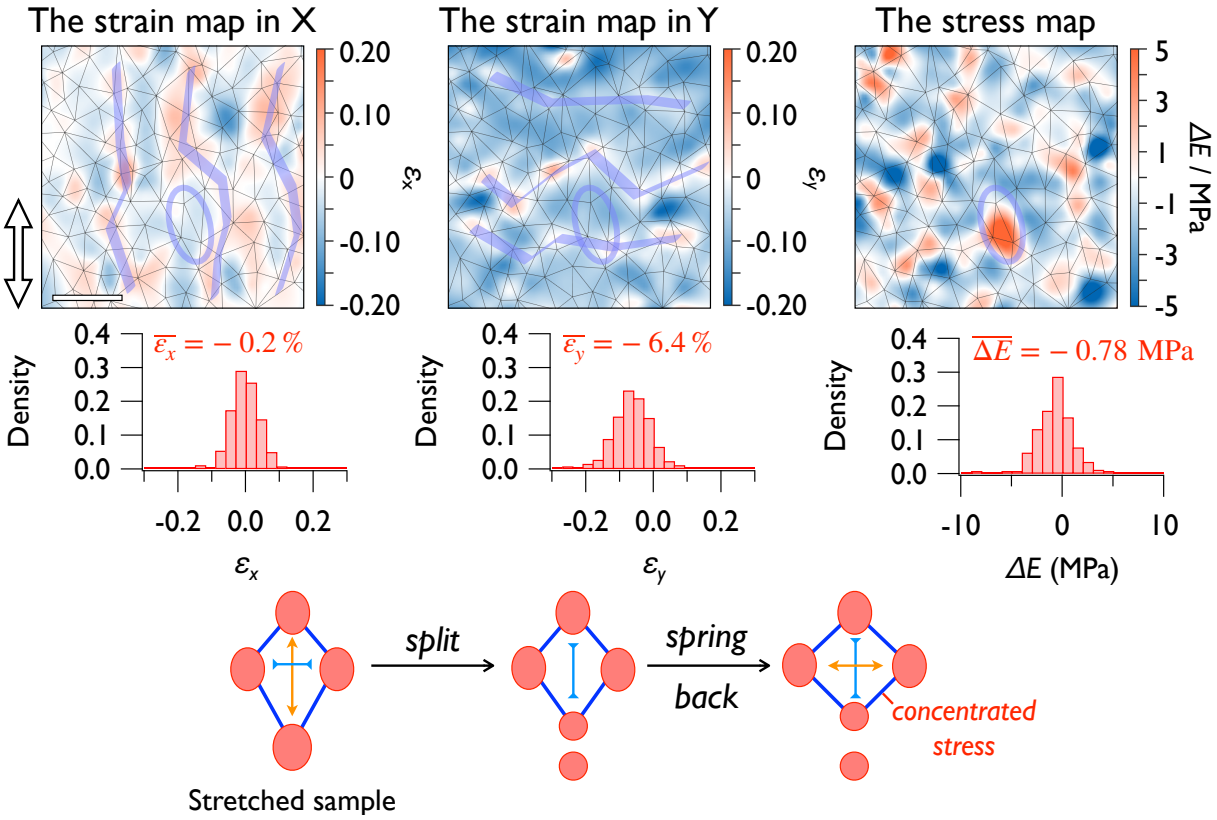

Figure 4.9: (Top) Value distribution of local strain and local stress. (Bottom) Schematic diagram of domain splitting during elongation and its effect on the strain.

The stress distribution shown in Fig. 4.8 is obtained by combining two modulus maps with the Delaunay mesh. Although 0.7 MPa reduces the average stress in the grid, we observe a stress concentration zone in the purple circle, which corresponds to the strain interface region. Such a stress concentration zone is detrimental to the stability of the network, and it seems reasonable to establish its correlation with the local strain. However, not all strain interfaces produce considerable stress concentrations, so we do not have enough evidence to prove whether the presence of strain interfaces is a sufficient condition for stress concentrations to occur. Then, we studied the strain and stress distributions in the late stage and compared them with the early stage. Numerically, ε_y and ΔE derived from Fig. 4.10 are -0.3% and -0.2 MPa, respectively, which are moderated compared to the early stage. The ε_x yields a value of -0.5%, which is similar to the results obtained from Fig. 4.5. We also observe a similar hierarchy in the strain

distribution in Fig. 4.10 as in the early stages. Such a before-and-after variation originates from the stress relaxation obtained through the early domain splitting, which is also evidenced by the stress diagram: no stress concentration similar to that in Fig. 4.10 is observed in the same region of Fig. 4.5.

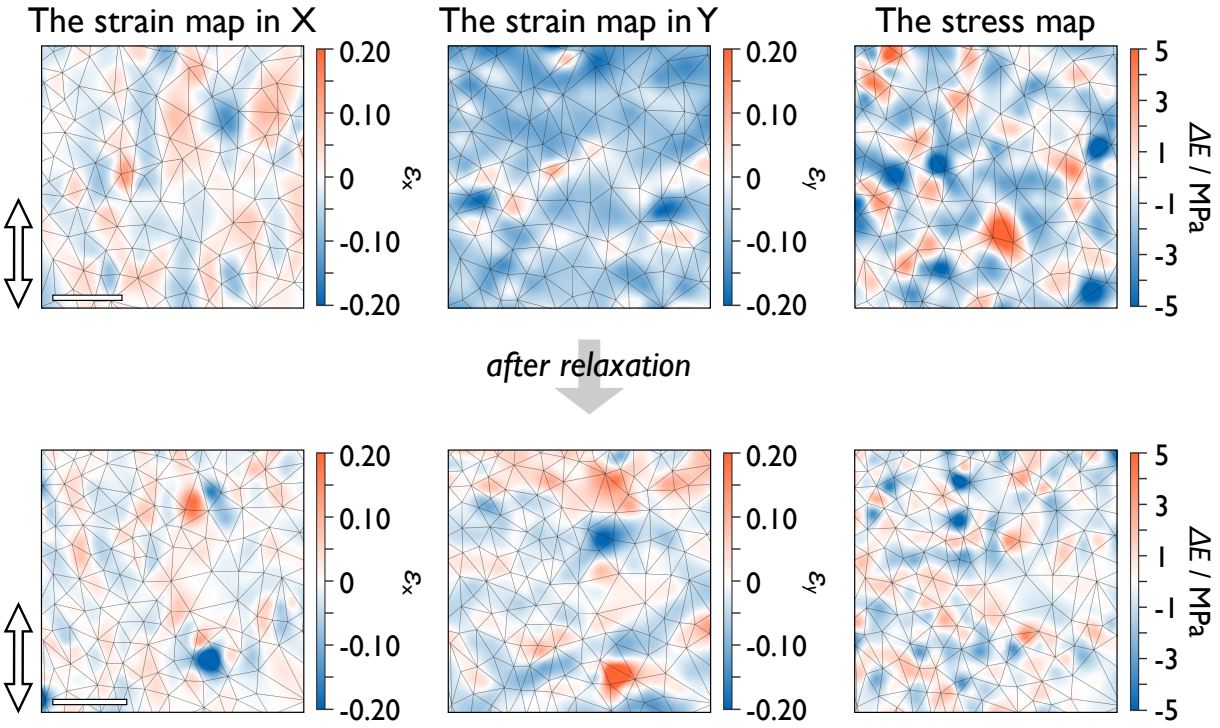

Figure 4.10: Linear-strain maps in the x and y coordinates derived from deformation maps with the stress map derived from modulus maps in (top) early and (bottom) late stages.

We further analyzed the numerical distribution of stresses and strains for all triangles in the early and late meshes. These values were normalized due to the large increase in the number of triangles through domain splitting in the early stages. Fig. 4.11 shows the strain distribution in the x-direction. In the later stages, the presence of large strains is reduced and the distribution becomes more concentrated at zero. For the y-direction shown in Fig. 4.5, although the concentration of values is not as pronounced as in the x-direction, the distribution is clearly shifted to the right and the center approaches zero, indicating that the strain behavior in the y-direction gradually approaches that of the x-direction. Considering that the y-direction is the elongation direction, this similarity between the strains in the x and y directions indicates that the network has been sufficiently moderated and converged to a stable state under prolonged elongation. However, such a steady state is not static, and the uniform distribution of strains

in the late x and y directions on either side of the zero point means that the entire network is still in a state of elastic fluctuation, as shown schematically in Fig. 4.11. As mentioned before, the stress concentration may be related to the interface of strains. At a later stage, the reduction of large local strains makes the stress concentration disappear, as shown in Fig. 4.5. By comparing the stresses, it is found that their distribution undergoes a clear convergence to zero at a later stage.

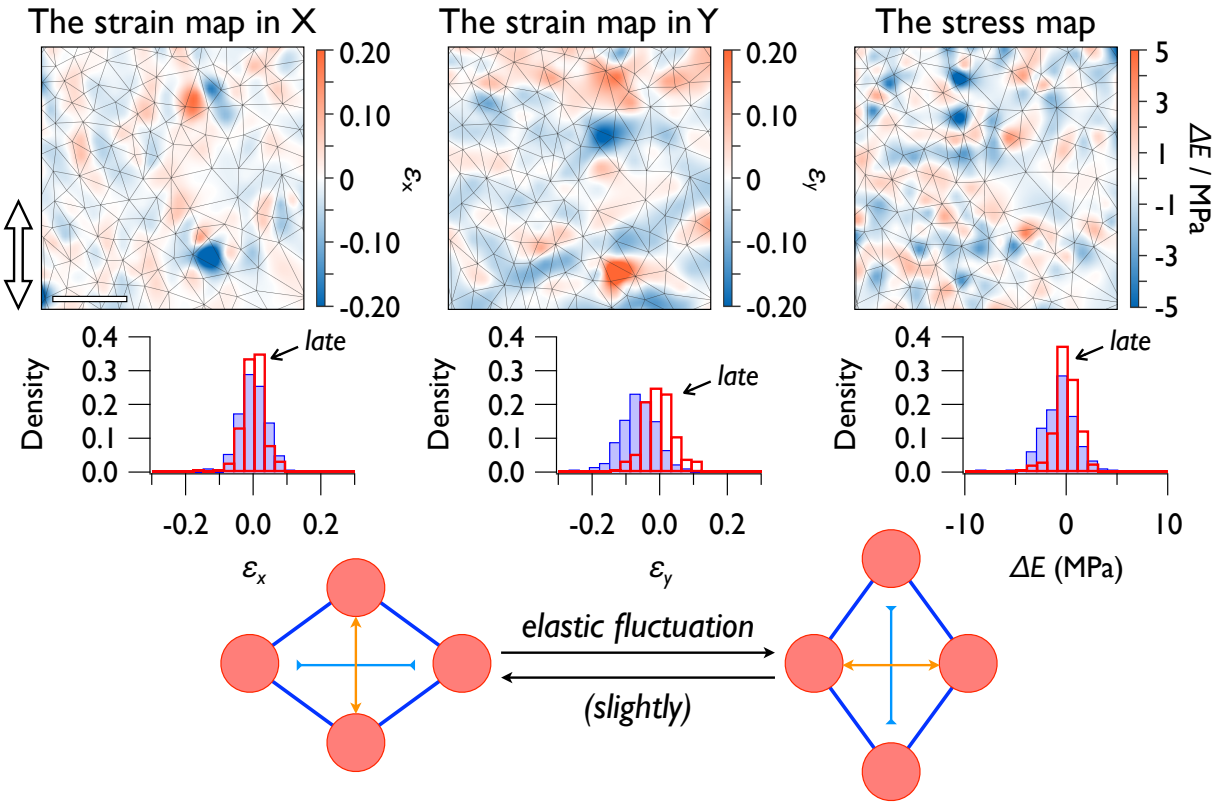

Figure 4.11: (Top) The distribution of ε_x, ε_y, and ΔE at the early and late stages. (Bottom) Schematic diagram of the dynamic fluctuations of the stress network in the late relaxation period.

The above discussion shows that the TPE network has dynamic and stable elasticity in the later stages after the early hard domain splitting. Although strain still occurs in each local region, the effective stress transfer of the bridge chain avoids stress concentration and thus prevents further domain splitting in the later stages. When designing high strength TPE materials with small residual strains, the topic often discussed is how to increase the strength of the hard domains to reduce the likelihood of hard domain splitting, and this is certainly true. However, assuming that the concentrated stress can be efficiently transferred through bridge chains in the

network, possible solutions in this case, such as increasing the elasticity of the soft segments in the block copolymer, i.e. bridge chains, or reducing the formation of ring chains by molecular design, may also be able to protect the hard domains themselves. To verify the correctness of the above deduction, the relevant molecular design is already in progress.

4.3 Summary

We developed a tool that combines in situ AFM nanomechanics and Delaunay triangulation to analyze topological changes in materials. When applied to the mechanical analysis of TPEs, we discovered the microscopic causes of macroscopic stress relaxation in TPEs during holding stretching. The internal stress network was sufficiently moderated to achieve stress and strain homogenization and dynamic elasticity after the dramatic evolution of the early phases. The hard phase in the microphase-separated structure relieves the local stress concentration by splitting, but at the same time, this irreversible change induces a permanent deformation of the material. This technique is also being applied to study other polymeric materials, such as filled rubber. Related work will be reported in the near future.

4.4 References

[1] Liu, H., Liang, X. & Nakajima, K. Direct visualization of a strain-induced dynamic stress network in a sebs thermoplastic elastomer with in situ afm nanomechanics. *Japanese Journal of Applied Physics* **59**, SN1013 (2020).

[2] Miyata, T. *et al.* Nanoscale stress distribution in silica-nanoparticle-filled rubber as observed by transmission electron microscopy: Implications for tire application. *ACS Applied Nano Materials* **4**, 4452–4461 (2021).

[3] Watanabe, H., Sato, T., Osaki, K., Yao, M.-L. & Yamagishi, A. Rheological and dielectric behavior of a styrene- isoprene- styrene triblock copolymer in selective solvents. 2. contribution of loop-type middle blocks to elasticity and plasticity. *Macromolecules* **30**, 5877–5892 (1997).

[4] Watanabe, H., Matsumiya, Y., Sawada, T. & Iwamoto, T. Rheological and dielectric behavior of dipole-inverted (sis) p-type multiblock copolymers: estimates of bridge/loop fractions for respective i blocks and effect of loops on high extensibility of bridges. *Macromolecules* **40**, 6885–6897 (2007).

[5] Parker, A. J. & Rottler, J. Molecular mechanisms of plastic deformation in sphere-forming thermoplastic elastomers. *Macromolecules* **48**, 8253–8261 (2015).

[6] Morita, H., Miyamoto, A. & Kotani, M. Recoverably and destructively deformed domain structures in elongation process of thermoplastic elastomer analyzed by graph theory. *Polymer* **188**, 122098 (2020).

[7] Dechnarong, N. *et al.* In situ synchrotron radiation x-ray scattering investigation of a microphase-separated structure of thermoplastic elastomers under uniaxial and equi-biaxial deformation modes. *Macromolecules* **53**, 8901–8909 (2020).

[8] Hsiue, G.-H., Chen, D.-J. & Liew, Y.-K. Stress relaxation and the domain structure of thermoplastic elastomer. *Journal of applied polymer science* **35**, 995–1002 (1988).

[9] Aoyagi, T., Honda, T. & Doi, M. Microstructural study of mechanical properties of the aba triblock copolymer using self-consistent field and molecular dynamics. *The Journal of Chemical Physics* **117**, 8153–8161 (2002).

[10] Shen, J., Liu, J., Gao, Y., Li, X. & Zhang, L. Elucidating and tuning the strain-induced non-linear behavior of polymer nanocomposites: a detailed molecular dynamics simulation study. *Soft Matter* **10**, 5099–5113 (2014).

[11] Ozmusul, M. S., Picu, C. R., Sternstein, S. & Kumar, S. K. Lattice monte carlo simulations of chain conformations in polymer nanocomposites. *Macromolecules* **38**, 4495–4500 (2005).

[12] Inoue, T., Moritani, M., Hashimoto, T. & Kawai, H. Deformation mechanism of elastomeric block copolymers having spherical domains of hard segments under uniaxial tensile stress. *Macromolecules* **4**, 500–507 (1971).

[13] Di Lorenzo, F. & Seiffert, S. Nanostructural heterogeneity in polymer networks and gels. *Polymer Chemistry* **6**, 5515–5528 (2015).

[14] Ronca, G. & Allegra, G. An approach to rubber elasticity with internal constraints. *The Journal of Chemical Physics* **63**, 4990–4997 (1975).

Chapter 5

Heterogeneously Formation of the Stress Network in the TPE

5.1 General

Materials science has been pursuing intuitive, efficient, and high-resolution characterization techniques to visualize the structure and properties of target samples. Among them, in situ microscopy is a particularly popular approach because of its ability to witness the dynamic behavior under externally stimulating conditions, such as strain, temperature, and the introduction of other substances[1]. However, in situ measurement means that the window displacement induced by the external stimuli need to be overcomed. Very noteworthy in this field is the high-speed AFM, which, although often not titled with 'in-situ', explains many dynamic processes of biomolecules[2;3]. As for the block copolymer with nanoscale microphase-separated structure, when stemming the macroscopic strain, such window displacment could make the in-situ observation much more difficult. In this chapter, I will use a newly-developed in-situ jig combined with AFM nanomechanics to investigate the initial elongation of the BCP-type TPE.

5.2 Results

5.2.1 In-Situ AFM Nanomechanical Mapping

Fig. 5.1 shows modulus maps of BCP-type TPE using in-situ AFM nanomechanics. Some feature hard domains are helpful to distinguish the similar observing area. With the increasing of macroscopic strain, yellow/brown hard domains are gradually connected by formed stress chain from the soft matrix. In the initial stage of elongation, easily-deformed soft segments of the block copolymer bear the imposed strain, and thus increases their stress. The dynamic behavior of stress network has already been well-discussed in Chapter 3 and Chapter 4. However, the formation of stress network, which was predicted[4;5;6] and simulated[7;8] for a long time, was first observed by in-situ AFM nanomechanics.

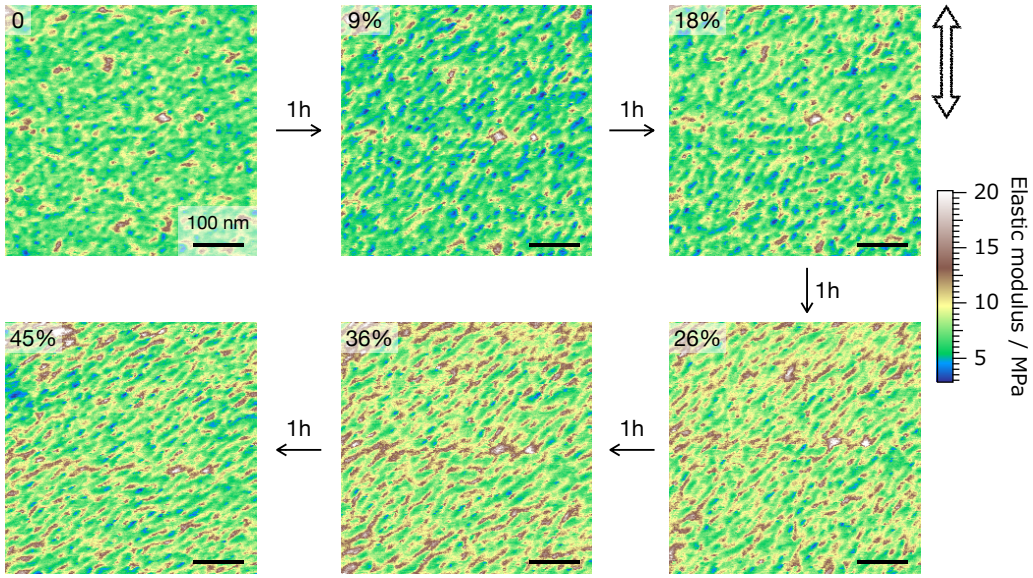

Figure 5.1: AFM modulus maps of BCP-type TPE under different strains. All the images are in the similar observing area.

The calculated microscopic strain shown in Fig. 5.1 is obtained from in-situ jig itself. However, the strain was also calculated by the camera window, the value comes to be a bit different.

Fig. 5.2 shows the photos of each stretched state. The difference of these two calculated valves increase with the increase of strain. It should be mentioned that due to the positioning and AFM capturing time, each photo was taken about an hour apart. Combining the above phenomena,

it can be learned that the polished surface in the figure undergoes a relative shrinkage with increasing strain, accompanied, of course, by an elongation of the area beyond the polished area. Such an inhomogeneous variation will be fully discussed in the subsequent analysis.

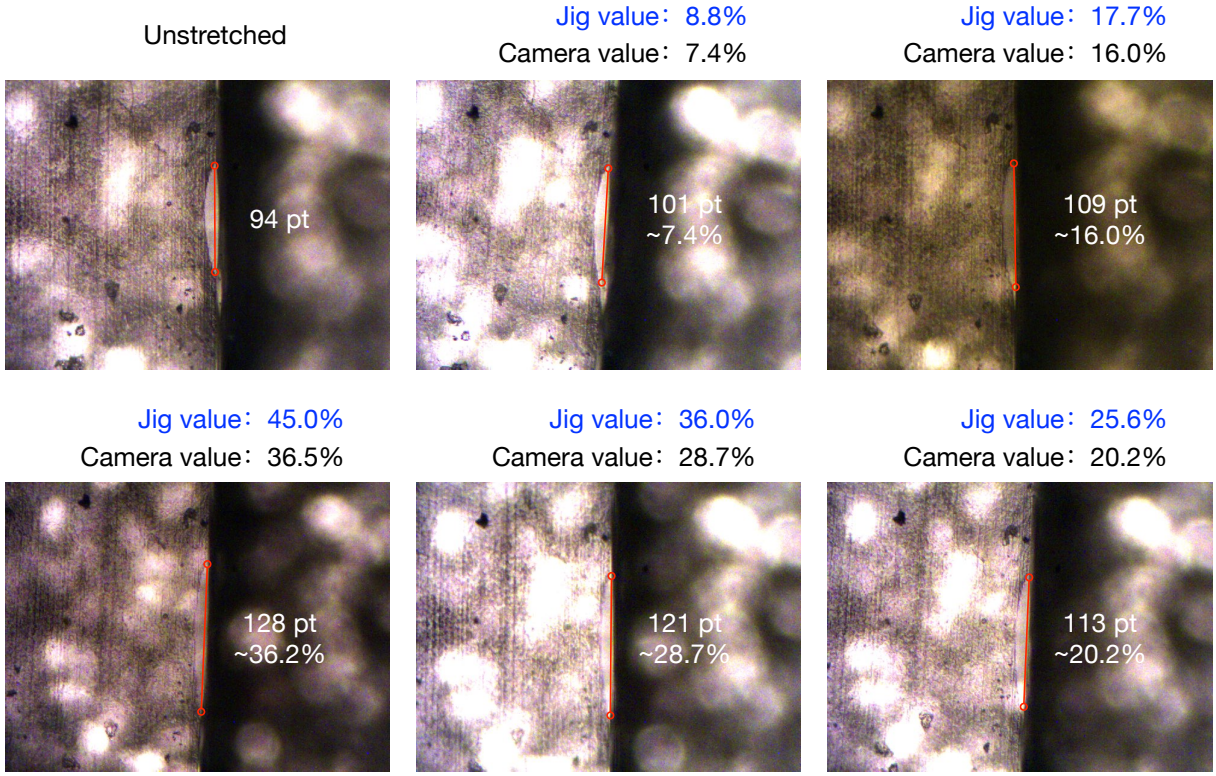

Figure 5.2: Microscopic strain of each stretched state calculated from jig and camera, respectively.

The distribution of elastic modulus of above AFM modulus images are then produced in Fig. 5.3. The maximum value of the modulus shows an overall nonlinear variation. From 0 to 9% , the overall modulus distribution remains basically the same, even the maximum value has some left shift with stretching. This indicates that at the earliest elongation, the bridge chain formed by soft segment was not fully stretched. From 9% to 26%, the maximum value continues to move to the right, indicating that the bridge chain has carried the stress adequately. Then, unexpectedly, after 26%, the maximum value of the modulus decreases again. This phenomenon is interesting so I tried to reproduce the experimental flow of the AFM on a macroscopic level.

As shown in Fig. 5.3, macroscopic staged tensile test was performed and each stage is held for one hour after stretching to approximate the AFM experimental procedure. The starting stress of each segment is summed with the slope of the curve of that stage as the representative

modulus. Interestingly, although the absolute values of the macroscopic and microscopic moduli are not comparable with each other, both of them show similar nonlinear variations, which suggests that the AFM results are reasonable and warrant further analysis.

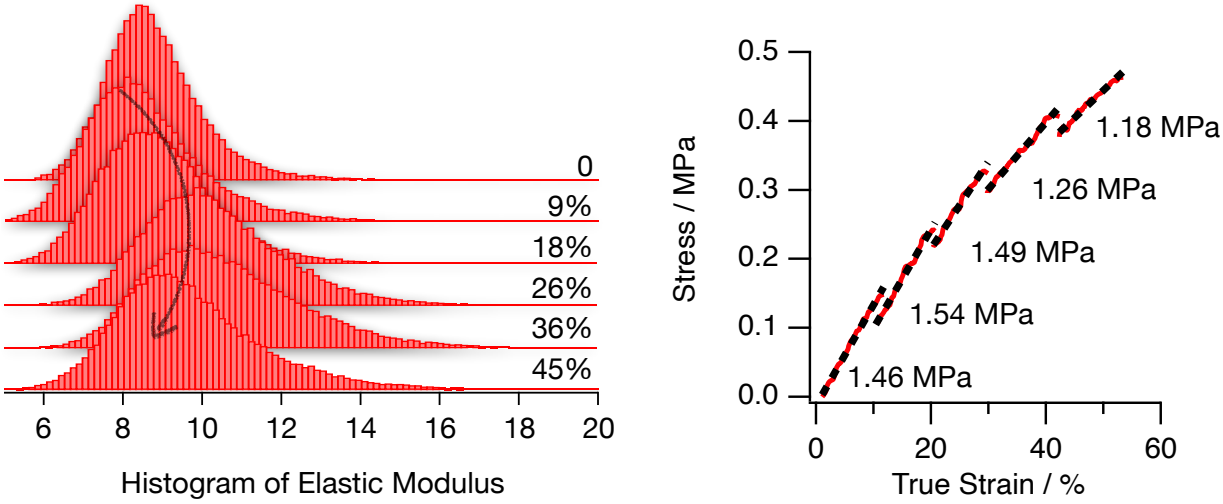

Figure 5.3: (Left) Distributions of elastic modulus in each image of Fig. 5.1. (Right) A macroscopic reproduction for in-situ AFM procedure.

5.2.2 Finite Element Analysis

FEA analysis gives a detailed explanation of AFM results. In the previous chapters, the sample were sufficiently relaxed to become very stable for AFM capture; thus, most of the domains could be used for the vertices of the triangulation. However, in this test, if every image is capture after enough relaxation (which usually takes more than three hours), not only the image positioning will become extremely difficult, but also the ultrathin samples used in the experiment are at great risk of breaking. Therefore, this time, only domains that are sufficiently distinct are used as vertices for triangular segmentation to the extent that relatively few regions are segmented. As shown in Fig. 5.4, in this chapter, The points were selected in such a way that all resolvable areas were taken into account as much as possible, and all points with significant splitting or fusion were excluded. For example, we exclude the region in the red box where fusion occurs after stretching, even though it is very easy to identify in the modulus map.

As shown in Fig. 5.5, I divided the six diagrams into three groups for image resolution, and

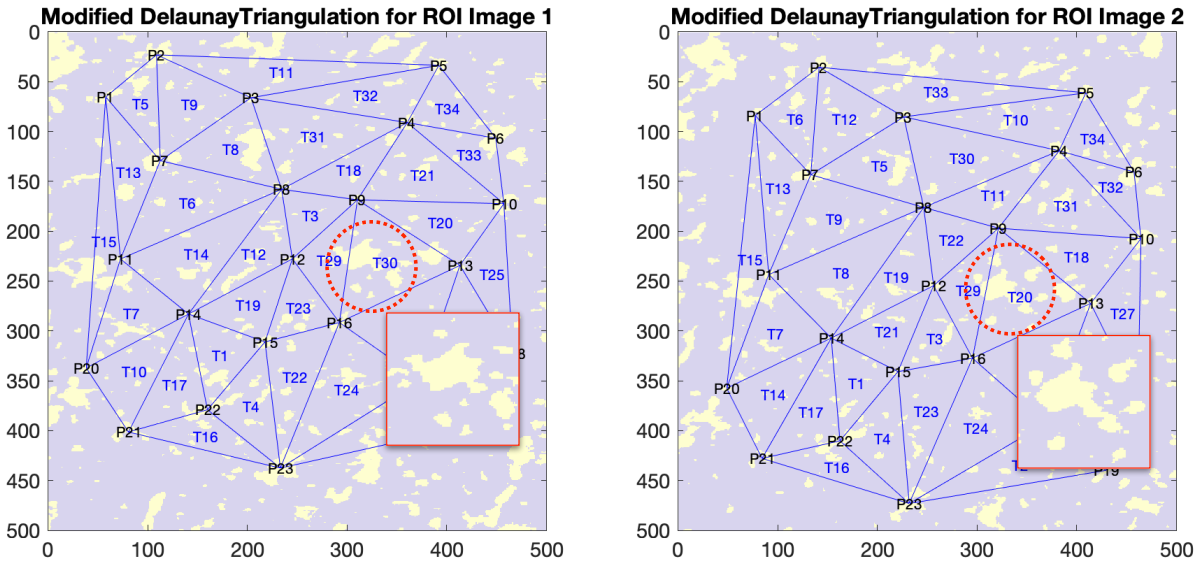

Figure 5.4: An example of selecting vertices.

calculated the strain and stress changes for each group separately. In the first stage, i.e., from 0 to 9%, almost all triangular meshes undergo regular triangular deformation. The Y-direction of the stretching is positive strain and the corresponding X-direction is negative strain. Such deformation indicates that the entire stress network is still in the elastic range. If the load is released at this point, then the material will fully recover its original length without permanent deformation. At the same time, the deformation of the network does not completely offset the external macroscopic deformation in stress, causing the creation of a stress concentration region.

The second stage i.e., from 18% to 26% shows a different change from the first stage. While the x-direction still presents negative strain throughout, which seems to be inevitable in a uniaxial stretching. In the y-direction, on the other hand, positive and negative strains alternate in the direction perpendicular to the stretching. The generation of inhomogeneous strain indicates the loss of the previous stability of the polymer network and the onset of hard phase splitting. However, the hard-domain splitting does not fully compensate for the external macroscopic strain, which causes an increase in stress in all regions at this stage.

The last stage, i.e. the leftward shift of the maximum value of the modulus distribution, is also reflected in the stress map where all regions are negative. The y-direction strain also shows all negative values at this point, indicating that the hard domain has produced a large number of

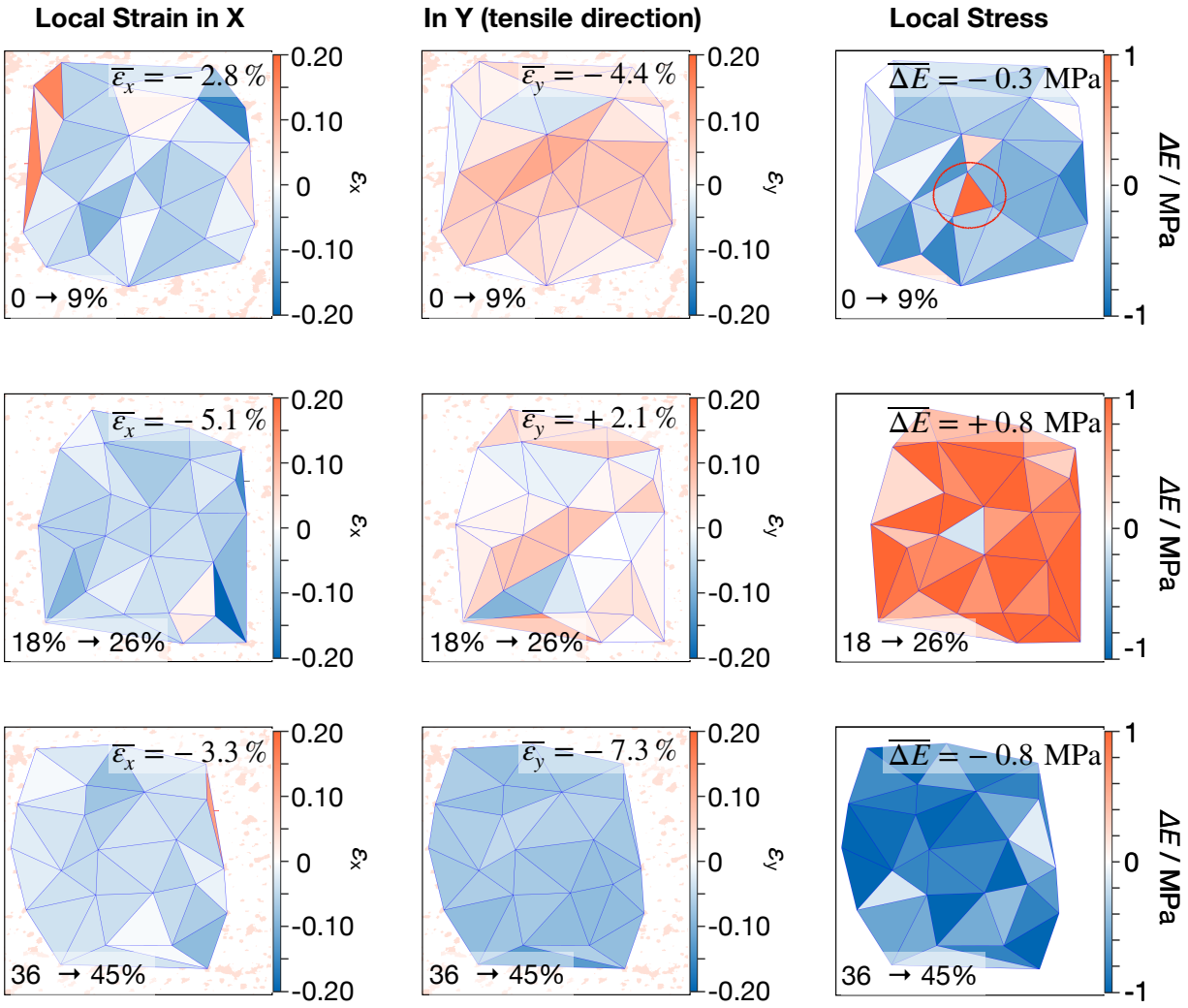

Figure 5.5: FEM analysis result on each stage of elongation.

splits and caused permanent and irreversible topological changes to the polymer network. At the macroscopic level, a permanent deformation of the material has been created.

5.2.3 The Origin of Permanent Deformation

In the previous section, we argued through FEM analysis that stress concentration occurs in the TPE during the stretching process, accumulating and eventually leading to massive splitting of the hard-domain. Another experiment was conducted to verify the full correlation between the domain splitting and the permanent deformation of the TPE during cyclic stretching. A TPE specimen was released after being held in 50% tension for two hours, and in situ AFM nanomechanics was used to test the structural and physical properties of the sample afterwards.

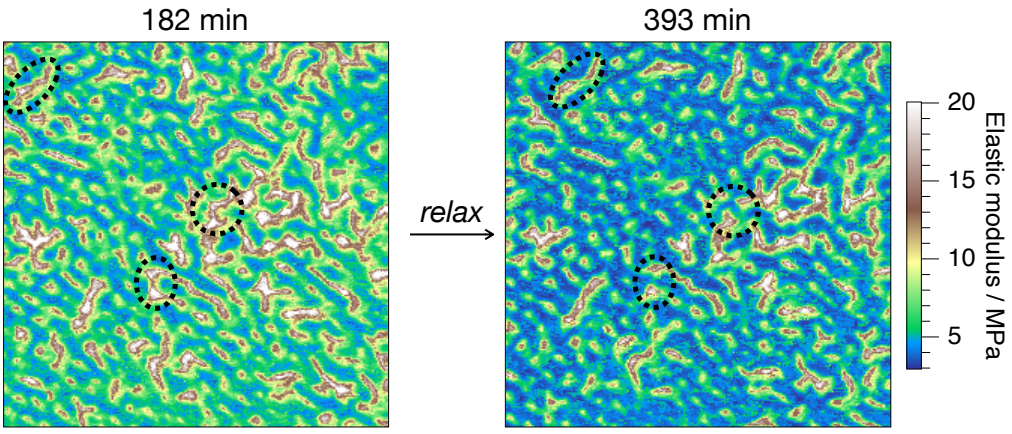

Figure 5.6: Elastic modulus maps of the sample after releasing the load and relaxing 182 and 393 min.

Fig. 5.6 shows elastic modulus maps of the sample after releasing the load and relaxing 182 and 393 min. The modulus of the soft matrix undergoes a significant decrease in the relaxing process. In addition, as shown in the circled position, the hard domain inevitably splits even at 0 load. We used a central hard domain as a reference and analyzed the relative movement of the

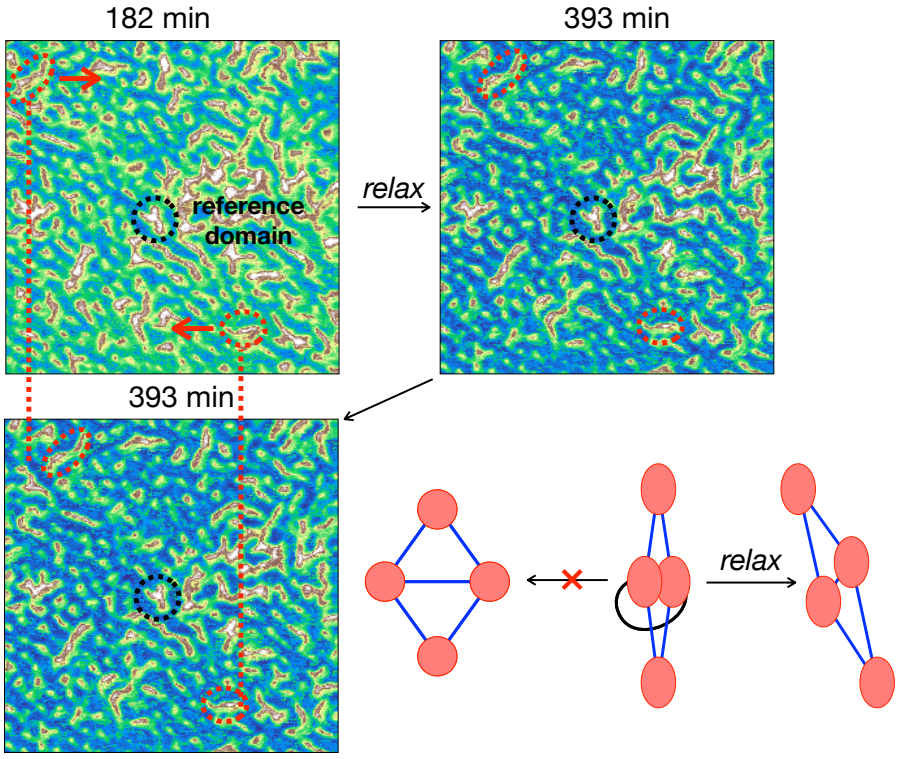

Figure 5.7: The analysis of the hard domain motion during the relaxing process and its schematic diagram.

domain during the relaxing process, and the results are shown in Fig. 5.7. Surprisingly, unlike the expected behavior of network recovery, the hard domains did not approach each other

along the stretching direction due to stress relaxing, but instead underwent relative motion perpendicular to the stretching direction. Such a phenomenon indicates that the topology of the material has been irreversibly changed during the stretching process, which has also been derived in the mathematical model[9]. During the stretching process, the bridge chain becomes loop chain due to domain fusion, or breaks away from the hard domain to form a free hard segment. During the relaxing, along with the splitting of the domain again, the bridge bond undergoes a recombination for the belonging relationship of the hard domain, i.e., a permanent topological change. Graph theory can also give a parsimonious explanation of this process[7].

5.3 Summary

We use a novel in-situ AFM nanomechanics combined finite element analysis to investigate the initial elongation of a BCP-type TPE. It has been proven that the nonlinear curves in the initial stage of tensile test as well as AFM modulus images are driven by internal hard-domain splitting. In addition, such a splitting brings permanent topological changes to the material, which affects the macroscopic mechanical properties.

5.4 References

[1] Li, X., Sun, M., Shan, C., Chen, Q. & Wei, X. Mechanical properties of 2d materials studied by in situ microscopy techniques. *Advanced Materials Interfaces* **5**, 1701246 (2018).

[2] Ando, T. *et al.* A high-speed atomic force microscope for studying biological macromolecules. *Proceedings of the National Academy of Sciences* **98**, 12468–12472 (2001).

[3] Ando, T., Uchihashi, T. & Fukuma, T. High-speed atomic force microscopy for nano-visualization of dynamic biomolecular processes. *Progress in Surface Science* **83**, 337–437 (2008).

[4] Rubinstein, M. & Panyukov, S. Elasticity of polymer networks. *Macromolecules* **35**, 6670–6686 (2002).

[5] Meng, F., Pritchard, R. H. & Terentjev, E. M. Stress relaxation, dynamics, and plasticity of transient polymer networks. *Macromolecules* **49**, 2843–2852 (2016).

[6] Hölzl, T., Trautenberg, H. L. & Göritz, D. Monte carlo simulations on polymer network deformation. *Physical review letters* **79**, 2293 (1997).

[7] Morita, H., Miyamoto, A. & Kotani, M. Recoverably and destructively deformed domain structures in elongation process of thermoplastic elastomer analyzed by graph theory. *Polymer* **188**, 122098 (2020).

[8] Aoyagi, T., Honda, T. & Doi, M. Microstructural study of mechanical properties of the aba triblock copolymer using self-consistent field and molecular dynamics. *The Journal of Chemical Physics* **117**, 8153–8161 (2002).

[9] Kodama, H. & Yoshida, K. A mathematical model of network elastoplasticity. *arXiv preprint arXiv:2107.04310* (2021).

Chapter 6

AFM Characterization of Triptycene-Appended Polymers

6.1 General

This chapter uses AFM to measure triptycene-appended polymers for phase structure and nanomechanical properties. As shown in Fig. 6.1, tripodal triptycenes, a member of tripthcene family, could have a 2D nested hexagonal packing with a 1D stacking layers[1]. This so-called '2D + 1D' structure has also been found in polymers where tripodal triptycene is appended in main chain[2], side chain[3], and two terminals[4]. However, this structural feature has not been visualized in AFM measurement. Therfore, the purpose of this chapter is to analyze the local characteristics of '2D + 1D' structure at the nanoscale and the effects on the structure and physical properties of the polymer.

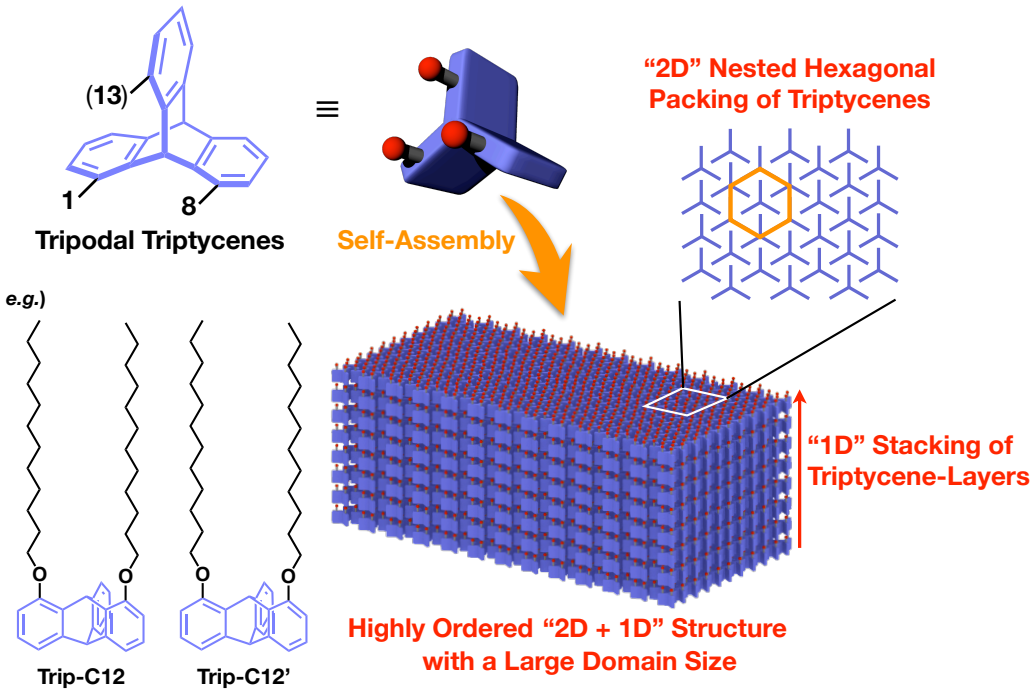

Figure 6.1: Schematic of triptycenes and their '2D + 1D' structure.

6.2 Results

Fig. 6.2 shows the chemical structures of triptycene-appended polymers used for AFM characterization. Among them, the control polymer using the same backbone without appending triptycene is liquid in 25 ℃, making it impossible to be measured. I will talk about the details of other three functional polymers.

6.2.1 Polymer with Appended Triptycene in the Side Chain

Trip-Block and Trip-Random are two polymers with appended triptycene in their side chains. The order of the monomers results in two polymers with very different phase structures. Fig. 6.3 shows the height and phase images of Trip-Block capturing in AFM tapping mode. Unlike the conventional spherical, cylinder or lamellar microphase-separation structures[5], the phase separation structure induced by triptycene seems to be slightly more complex. However, localized lamellar structures can be observed and the interlamellar distances are consistent with the SAXS results (not shown in this thesis). Note that this film has not been annealed over its melting point. Although we believed that the observed '1D' structure would be clearer

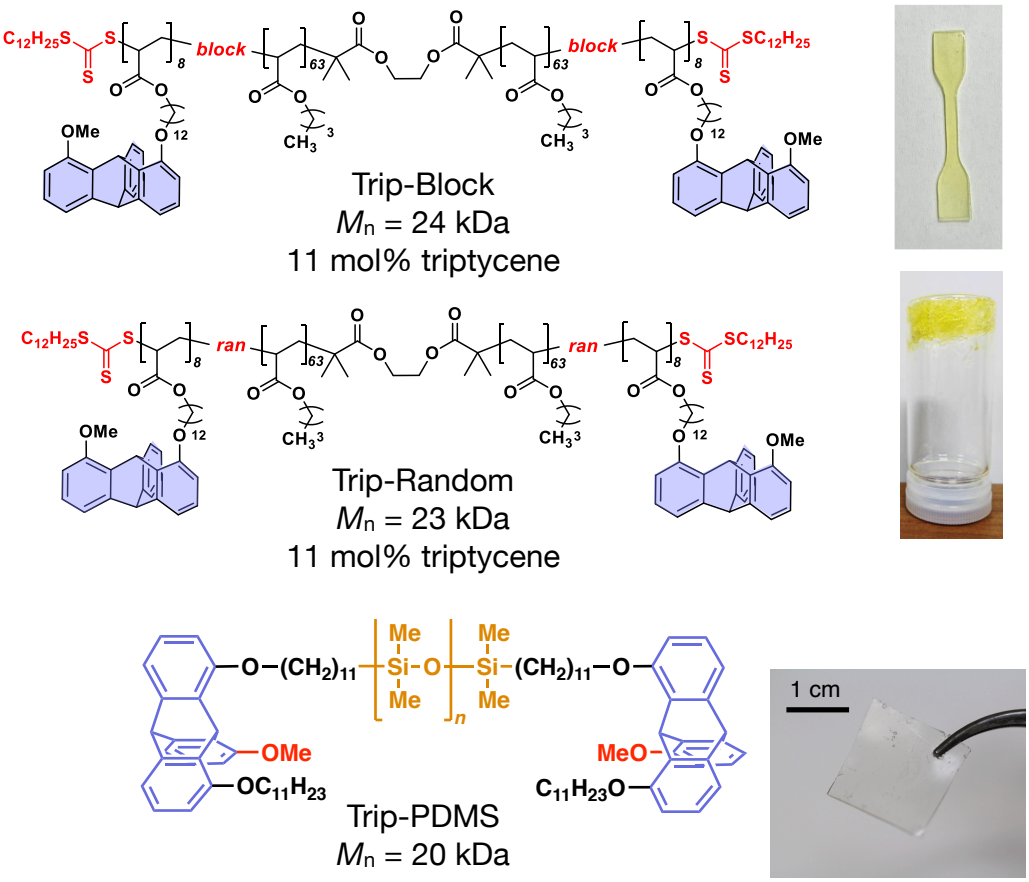

Figure 6.2: Chemical structures of triptycene-appended polymers.

and more orderly after annealing, the main chains of the polymer tend to float to the surface, causing the triptycene induced phase structure to be difficult to observe[6].

Trip-Random shows totally different behavior compared with Trip-Block. As shown in Fig. 6.4, previously unseen sheet-like microphase-separated structures were observed. There is no doubt that phase separation are more difficult to form in random copolymers that possess lower order compared to block copolymers. Another speculation here is that the melting point of Trip-Random is lower than 25℃, so the film is annealed for a long time after it is made. Because of the higher degree of freedom of the main chain in the random copolymer, the triptycene has a higher probability of forming microcrystals. In order to verify this speculation, there is a plan to make a higher resolution observation of the sheet portion in the figure.

AFM nanomechanics was then performed in Trip-Block and Trip-Random. As shown in Fig. 6.5, similar layer structure is also observed in the modulus map of Trip-Block. As for Trip-Random, part of the high modulus region can also be observed, which also illustrates the

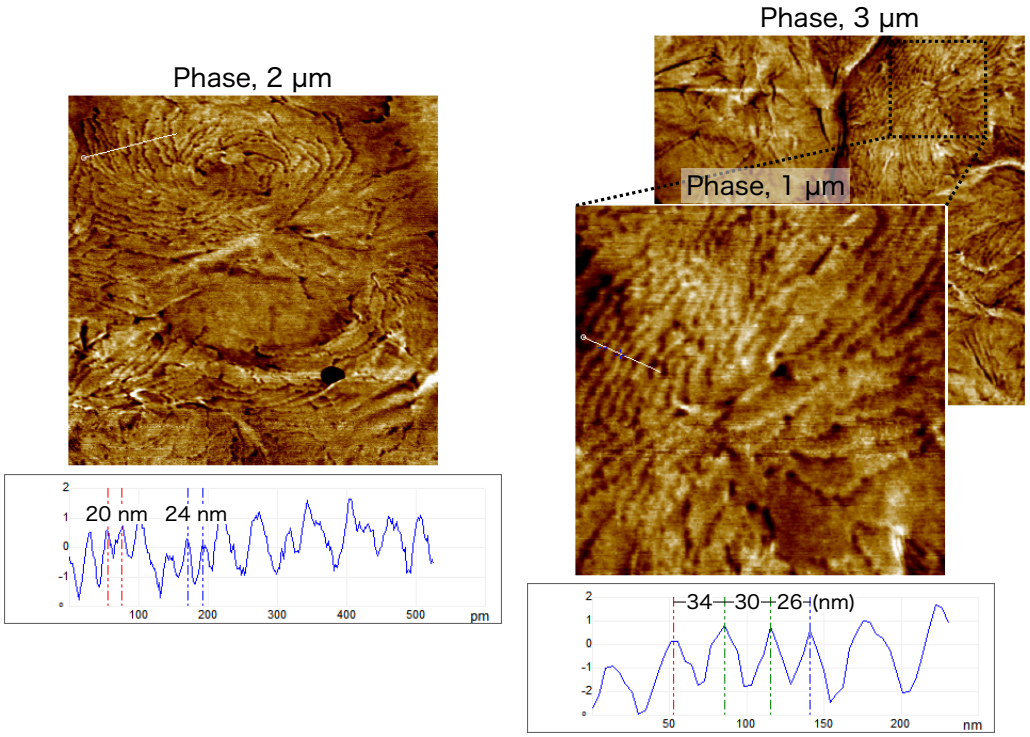

Figure 6.3: Height and phase images of Trip-Block obtained in AFM tapping mode.

possibility of microcrystalline formation as described above. The modulus distributions of the two polymers can give a visual comparison of the nanomechanical properties. Both have the same interval in the low modulus region, while Trip-Block has more components in the high modulus region compared to Trip-Random, which suggests that the formation of self-assembled structures with more triptycene in Trip-Block contributes to the mechanical strength of the material. We still want to emphasize that the unannealed samples have a high probability of being in a non-equilibrium state, so additional experiments will be performed in the future.

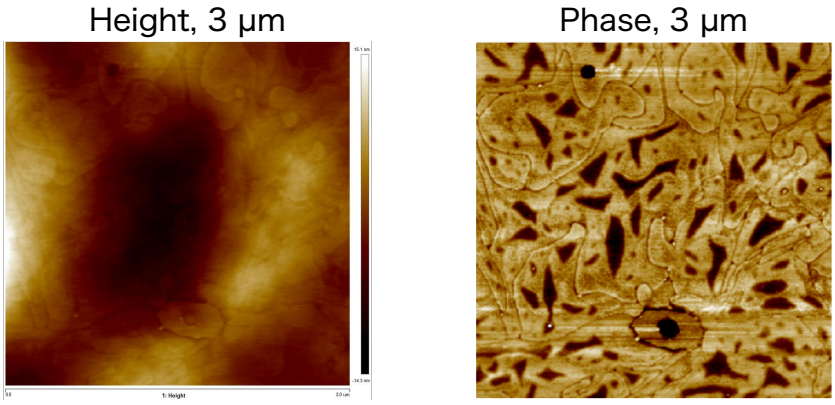

Figure 6.4: Height and phase images of Trip-Random obtained in AFM tapping mode.

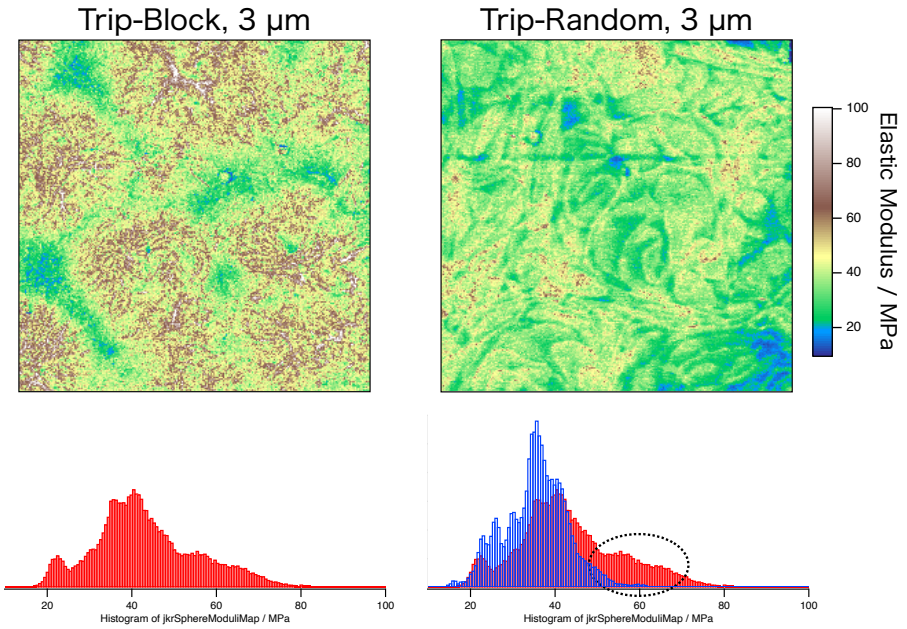

Figure 6.5: Nanomechanical mappings with the distribution of modulus of Trip-Block and Trip-Random.

6.2.2 Polymer with Appended Triptycene in Two Terminals

Another polymer in a more extreme form, namely Trip-PDMS with just one triptycene unit added to each end of Polydimethylsiloxane (PDMS), will also be discussed. It has been shown that PDMS with bipodal triptycene at both ends can form long-range ordered structures and substantially increase the viscosity and modulus of PDMS[4]. Tripodal triptycene has a stronger tendency to self-assemble compared with the former, so it is expected to further enhance the mechanical properties of PDMS.

We first characterized Trip-PDMS using a small scan size. As shown in Fig. 6.6, some strip-like structure was observed and it was traced by window displacement. Interestingly, we found that these strips are kept connected all the time, which prompted us to scan a larger size to grasp the overall morphology of this phase structure. Therefore, we replaced an AFM with a larger scan size to re-characterize it. The result is shown in Fig. 6.7.

We observed a large area of continuous mesh structure at a scan size of 20 μm, as shown in Fig. 6.7. This result is undoubtedly surprising because the change in this polymer compared to the original amorphous PDMS is only two small molecules at each end. The self-assembly of this small molecule, i.e., tripodal triptycene, drives the formation of a network-like phase separation

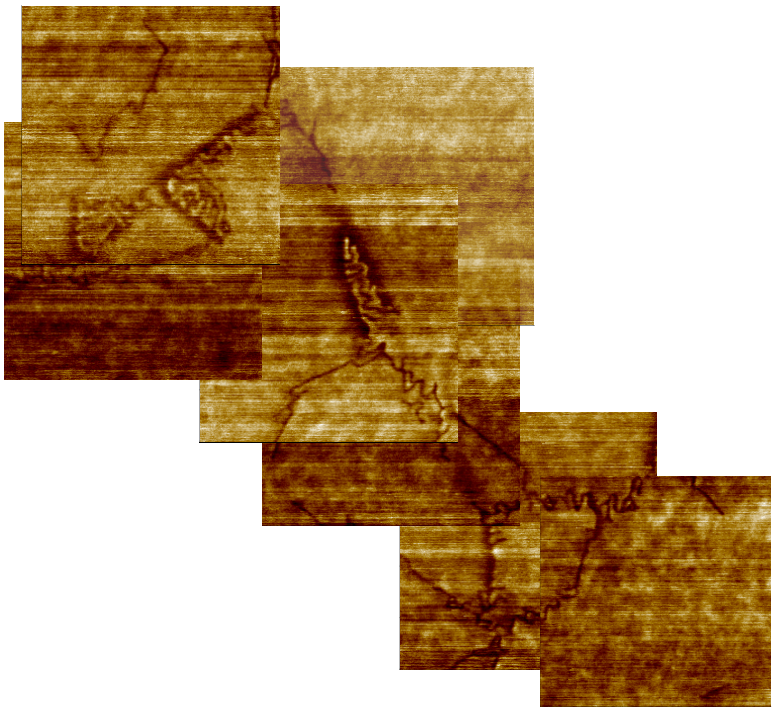

Figure 6.6: A first attempt at trip-PDMS in a small scan size. (phase images in tapping mode, 500 nm)

structure inside the polymer and greatly increases the mechanical properties of PDMS. The macroscopic manifestation of this enhancement is the transformation of PDMS, which was a liquid at room temperature, into a stretchable solid (Fig. 6.2). The cross-section drawn in its height image shows a layer spacing of ∼25 nm, which is consistent with previous reports and SAXS data (not shown in this thesis).

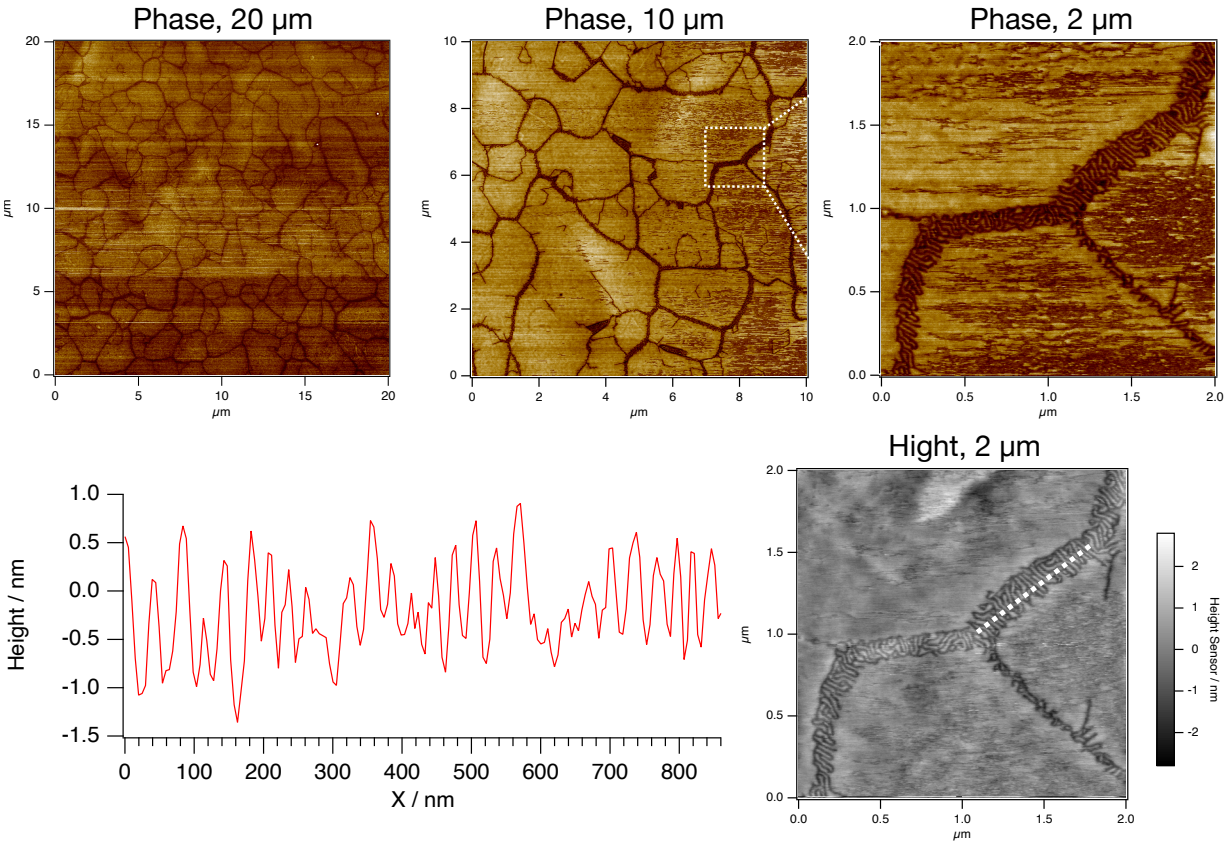

Figure 6.7: Phase and height images of Trip-PDMS with its layer spacing from the cross-section.

6.3 Summary

Polymers with appended triptycene in side chain and two terminals were investigated by AFM. The introduction of triptycene allows the polymer to form special phase separation structures. Meanwhile, triptycene as a hard phase in the phase separation structure helps to improve the macroscopic mechanical strength of the material. As a future plan, higher resolution AFM characterization is expected to be implemented, thus challenging the de-observation of the complete '2D + 1D' structure.

6.4 References

[1] Seiki, N. *et al.* Rational synthesis of organic thin films with exceptional long-range structural integrity. *Science* **348**, 1122–1126 (2015).

[2] Ishiwari, F., Okabe, G., Kajitani, T. & Fukushima, T. Introduction of triptycene with a particular substitution pattern into polymer chains can dramatically improve the structural and rheological properties. *ACS Macro Letters* **10**, 1529–1534 (2021).

[3] Liu, H. Synthesis, structure, and physical properties of tripodal triptycene-appended vinylic polymers and copolymers. *Master Thesis of Tokyo Institue of Technology* (2019).

[4] Ishiwari, F. *et al.* Terminal functionalization with a triptycene motif that dramatically changes the structural and physical properties of an amorphous polymer. *Journal of the American Chemical Society* **140**, 13497–13502 (2018).

[5] Matsen, M. W. Effect of architecture on the phase behavior of ab-type block copolymer melts. *Macromolecules* **45**, 2161–2165 (2012).

[6] Saito, M., Ito, K. & Yokoyama, H. Mechanical properties of ultrathin polystyrene-b-polybutadiene-b-polystyrene block copolymer films: Film thickness-dependent young' s modulus. *Macromolecules* **54**, 8538–8547 (2021).

Chapter 7

Summary and Open Questions

7.1 Summary of Thesis

In this PhD thesis, in-situ AFM nanomechanics was developed using TPE as the object of study and the formation and dynamic evolution of the stress network inside the TPE was observed. Also, in the local stress-strain analysis of AFM maps using FEA, we found that the topology inside the TPE is permanently changed under the influence of the stress network and directly affects the macroscopic physical properties of the TPE. As a tool for microscopic characterization combined with image analysis, the method described in this thesis gives a nano-scale mechanism for the macroscopic physical behavior of the material, which may be widely used in the in situ analysis of other structural polymer materials.

7.2 Open Questions

In addition to the study of methodology, the starting point of this thesis is how to guide the development of new TPE materials by solving the deformation mechanism of TPE. In fact, in addition to the research documented in the thesis, research on TPE materials based on novel polymers or polymer blends is already being implemented. It must be acknowledged that

the development of new materials is a complex process and that the molecular design from the principles or the polymer blending ratios from the simulations can be easily influenced by the subsequent processes, impurities, processing temperatures, and testing methods. On the other hand, there may be potential to improve traditional industrial practices, such as increasing molecular weight, improving the purity of raw materials, etc. For this complex object of research, I hope that one day experiments, simulations and mathematical models will cooperate perfectly to truly understand the nature of the structure and properties of materials.

7.3 List of Achievements

Original Papers

Papers Related to This Thesis

1. Chapter 3: Direct Visualization of a Strain-Induced Dynamic Stress Network in a SEBS Thermoplastic Elastomer with In Situ AFM Nanomechanics

   Haonan Liu, Xiaobin Liang, and Ken Nakajima, *Japanese Journal of Applied Physics* **2020**, *59*, SN1013. DOI: 10.35848/1347-4065/ab948a.

2. Chapter 4: Nanoscale Strain-Stress Mapping for Thermoplastic Elastomer Revealed Using a Combination of In-Situ AFM Nanomechanics and Delaunay Triangulation

   Haonan Liu, Xiaobin Liang, and Ken Nakajima, *submitted to Physical Review Letters.*

3. Chapter 5: Heterogeneously Formation and Dynamic Evolution of a Stress Network during the Initial Elongation of a SEBS Thermoplastic Elastomer, *in preparation.*

Papers not Related to This Thesis

1. Direct visualization of interfacial regions between fillers and matrix in rubber composites observed by atomic force microscopy-based nanomechanics assisted by electron tomography

Makiko Ito, Haonan Liu, Akemi Kumagai, Xiaobin Liang, Ken Nakajima, and Hiroshi Jinnai, *Langmuir* **2022**, DOI: 10.1021/acs.langmuir.1c02788

2. Tracking the evolution of the morphology and stress distribution of SIS thermoplastic elastomers under tension using atomic force microscopy

   Ling Gao, Haonan Liu, Xiaobin Liang, Makiko Ito, and Ken Nakajima, *submitted*.

3. Programmable Reversible Shape Transformation of Hydrogels Based on Transient Structural Anisotropy

   Kangkang Liu, Yue Zhang, Heqing Cao, Haonan Liu, Yuhui Geng, Wenhua Yuan, Jian Zhou, Zi Liang Wu, Guorong Shan, Yongzhong Bao, Qian Zhao, Tao Xie, and Pengju Pan, *Advanced Materials* **2020**, *32*, 2001693. DOI: 10.1002/adma.202001693.

Awards and Recognitions

1. Best Poster Award, 27th International Colloquium on Scanning Probe Microscopy, 2019
2. Tokyo-Tech Pioneering Doctoral Research Program, 2021-2022
3. Tokyo Tech Tsubame Scholarship, 2019-2021
4. Monbukagakusho Honors Scholarship, 2017-2018, 2021-2022

Conferences and Presentations

International Conferences in PhD Course

1. Local Strain-Stress Evolution of Polymeric Materials Revealed by In-Situ AFM Nanomechanical Mapping

   Haonan Liu, Xiaobin Liang, and Ken Nakajima, *29th International Colloquium on Scanning Probe Microscopy*, 9-10 December **2021**, Online

2. AFM Nanomechanical Studies on Dynamic Stress Networks of Stretched Thermoplastic Elastomer (*Best Poster Award*)

   Haonan Liu, Xiaobin Liang, and Ken Nakajima, *27th International Colloquium on Scanning Probe Microscopy*, 5-7 December **2019**, Shizuoka, Japan

3. Direct Visualization of Dynamic Stress Networks of TPE Based on AFM Nanomechanics

   Haonan Liu, Xiaobin Liang, and Ken Nakajima, *13th China-Japan Seminar on Advanced Engineering Plastics, Polymer Alloys and Composites*, Shandong, China, , 19-23 November **2019**

Domestic Conferences in PhD Course

1. 熱可塑性エラストマーの初期伸長過程における応力ネットワークの形成とその動的挙動

   劉　浩男・梁　暁斌・中嶋　健　第３２回エラストマー討論会　2021年11月24日～25日　九州大学稲盛財団記念館

2. Self-assembling Behavior and Mechanical Properties of Triptycene-Appended Block Copolymers

   Ayami Itagaki, Fumitaka Ishiwari, Tomoya Fukui, Takashi Kajitani, Haonan Liu, Xiaobin Liang, Ken Nakajima, Takanori Fukushima　第７０回高分子討論会　2021年9月6日～8日　オンライン

3. ドロネー三角形分割に基づく応力下の熱可塑性エラストマーにおける動的ネットワークの構造解析

   劉　浩男・梁　暁斌・中嶋　健　第７０回高分子学会年次大会　2021年5月26日～28日　オンライン

4. In situナノ触診AFMによるブロックコポリマー型TPEの変形挙動解析

   劉　浩男・梁　暁斌・中嶋　健　日本ゴム協会２０２０年年次大会　2020年5月21日～22日　中止

5. ナノ触診原子間力顕微鏡によるブロックコポリマー型TPEの変形挙動解析

   劉　浩男・梁　暁斌・中嶋　健　第２９回日本ＭＲＳ年次大会　2019年11月27日～29日　横浜情報文化センター

6. ナノ触診原子間力顕微鏡による熱可塑性エラストマーの変形挙動解析

   劉　浩男・梁　暁斌・中嶋　健　第６８回高分子討論会　2019年9月25日～27日　福井大学文京キャンパス

Domestic Conferences in Master Course

7. 三脚型トリプチセン含有ビニルポリマーおよびコポリマーの合成と自己集合化挙動

   劉　浩男・石割　文崇・梶谷　孝・福島　孝典　第６７回高分子学会年次大会　2018年5月23日～25日　名古屋国際会議場

8. 三脚型トリプチセン含有ビニルポリマーおよびコポリマーの合成と自己集合高分子の自己集合挙動と物性に影響を与える三脚型トリプチセンユニットの特異な効果

   石割　文崇・岡部　玄・劉　浩男・荻原　響・山下　幸大・木村　忠弘・梶谷　孝・福島　孝典　日本化学会第９８春季年会　2018年3月20日～23日　日本大学船橋キャンパス

Other Presentations

1. (Invited, online) Study of Polymer Nanomechanics Based on Atomic Force Microscopy, 3 June **2021**, Invited Lecture for State Key Laboratory of Chemical Engineering of Zhejiang University, online

2. (若手発表) ドロネー三角形分割に基づく応力下の熱可塑性エラストマーにおける動的ネットワークの構造解析　JST CREST 革新材料開発第５回領域会議　2020年11月14日　オンライン

3. AFM Nanomechanical Studies on Dynamic Stress Networks of Deformed Thermoplastic Elastomer, 2020 Dalian University of Technology-Tokyo Institute of Technology Joint Workshop on Advanced Materials, 21 November **2020**, online

4. Direct Visualization of Dynamic Stress Networks of TPE Based on AFM Nanomechanics, Tokyo Tech-Imperial College London 3rd Workshop on Plastic Electronics and Related Science and Technology, 18 November **2019**, Tokyo Tech Front

Appendix A

Materials and Methods

A.1 Materials and Instruments

A.1.1 Materials

Unless otherwise stated, all commercial reagents were used as received. The specimen used in Chapter 3-5, i.e., SEBS triblock copolymer (JSR Dynaron 8600P, styrene content = 15 wt%), namely, SEBS15, was purified by reprecipitation from a toluene solution into methanol. The sample was dried under vacuum at 50 ℃ for three days to remove the residual solvent. The triptycene-related block polymers were obtained from Fukushima group, Department of Chemical Science and Engineering, Tokyo Institute of Technology.

A.1.2 AFM Probe

This thesis used two probes, OMCL-AC160TS with high resonance frequency for observing the basic material phase structure in tapping mode, and ScanAsyst-Air for observing the nanomechanical properties of materials with higher resolution and more accurate physical properties. The basic information for them is shown in Table A.1. The radius R of the ScanAsyst-Air probe was evaluated by scanning a Nioprobe TipCheck sample (Aurora NanoDevices Inc., Canada)

in QNM mode with a scan rate, scan size, and image resolution of 0.5 Hz, $400 \times 400\ nm^2$, and $1024 \times 1024\ pixels$, respectively, and the probe radius was determined to be 2∼5 nm from the obtained height maps following the method in the previous report[1]. The spring constant k of the cantilever was measured to be 0.4∼0.5 N/m using the thermal tuning method[2].

	ScanAsyst-Air	OMCL-AC160TS
Brand and origin	Bruker, USA	Olympus, Japan
Geometry	Triangular	Rectangular
Normal tip radius (nm)	2	7
Normal frequency (KHz)	70	300
Normal spring constant (N/m)	0.4	26

Table A.1: AFM probe information

A.1.3 Instruments

The basic information of all scientific instruments used in this thesis is shown in Table A.2.

Instrument name	Brand and origin	Model
Atomic force microscope	Bruker, USA	MultiMode 8
Atomic force microscope	Bruker, USA	Dimension Icon
Ultramicrotome	Leica Microsystems, Germany	EM UC6
Tensile tester	Shimadzu, Japan	EZ-S
Thickness gauge	Asker, Japan	SDA-25
Vacuum drying oven	Yamato Scientific, Japan	ADP200
Spin Coater	Mikasa, Japan	MS-B100
Analytical balance	Shimadzu, Japan	AUX120
Mini test press	Toyoseiki, Japan	MP-2F

Table A.2: Instrument information

A.2 Methods

A.2.1 Sample Preparation

Three preparation methods were used to observe the surface and internal structure and physical properties of the samples. The surface structure was observed by spin coating into a film, and

the internal structure was observed by hot pressing (for SEBS) or solvent casting (for others).

Spin Coating

The sample was configured as a 5 mg/ml solution of toluene. 0.5 ml of the solution was added dropwise to a 10 mm diameter glass substrate and spin-coated at 2000 rpm for 30 seconds. The prepared films were glued to a 15 mm diameter stainless steel base with carbon tape for the subsequent annealing step. The annealing temperature varies depending on the sample and will be described in each chapter.

Hot Press

The SEBS15 film was then prepared by a hot-press casting procedure. The sample is first preheated at 150 ℃ for 5 min and hot pressed at 10 MPa for 1 min. Then presure released and cold pressed again at 10 MPa for 2 min. The thickness of the sample was made to be 0.2 mm or 1 mm depending on the application.

Solvent Casting

2 g of sample was dissolved in 10 ml of toluene solution and poured in a 75 mm round Teflon Petri dish. The film was dried in a fume hood at 25 ℃ for one week and then vacuum dried at 80 ℃ for one week to obtain a final thickness of 0.3 mm to 0.6 mm.

A.2.2 Tensile Test

All tensile tests were carried out at a temperature of 25 ℃. The specimen was cut into a dumbbell shape (20 mm gauge length and 2 mm width) and uniaxially stretched at 40 mm/min crosshead speed. To obtain comparable results, the same experiment was repeated at least three times on different specimens.

A.2.3 Sample's Pre-Polishing for AFM

To create a polished sample for AFM investigation, the bulk specimen was cut into an ultrathin section with a thickness of 300 nm at -120 ℃.

A.2.4 AFM Nanomechanical Mapping

Elastic modulus maps were recorded at 25 ℃using the PeakForce quantitative nanomechanical mapping (QNM) mode. A Nanoscope V controller and version 9.1 of the Nanoscope software were used. Force-deformation curves (FCs), which were converted from the original deflection-displacement curves[3], were obtained during a typical AFM nanomechanical mapping process by moving the AFM cantilever-probe tip assembly forward and backward along a randomly selected surface while measuring the relationship between the force and deformation. Meanwhile, an E-type Z-piezo scanner's oscillated the sample at frequencies, peak forces, and peak force amplitudes of 1 kHz, 0.5 nN, and 100 nm, respectively. The FCs were gathered at a digital resolution of 256 x 256 pixels. Each FC was subjected to topographical imaging and simultaneous mapping of mechanical properties. Johnson-Kendall-Roberts (JKR) contact mechanics were applied to the retraction part of the FCs during data analysis to account for the corresponding Young's modulus E[4]. Chapter 2 contains specifics.

Appendix B

Description for *SSMapping*

B.1 General

A Matlab-based program *SSMapping* was developed and used to analyze in-situ AFM images. I was inspired by the work of Jinnai et al[5], who performed in-situ TEM experiments on filled rubber and evaluated the material's local strain by Delaunay triangulation of the filler particles. Fig. B.2 shows the flow chart of *SSMapping*. For example, if the TPE contains a 15 wt% proportion of hard segments, in the AFM deformation map, the 15% small-deformed area is regarded as the hard phase and the discontinuous set of domains is naturally obtained. The geometric center of each domain was selected as the representative point. The Delaunay triangulation algorithm was modified from Matlab syntax to apply to the processing of AFM images. Since the Delaunay mesh adopts the nearest neighbor rule, the auto-generated mesh is reconstructed accordingly so that the triangles from different images can correspond exactly. The calculation of a single triangular deformation is shown in Fig. B.1, which is often used in the FEA process. The strain in the x (ε_x) coordinate, strain in y (ε_y) coordinate, and shear strain (γ_{xy}) can be derived separately using the strains of the respective triangles:

$$\varepsilon_x = \frac{(y_2 - y_3)u_1 + (y_3 - y_1)u_2 + (y_1 - y_2)u_3}{x_2y_3 + x_1y_2 + x_3y_1 - x_2y_1 - x_3y_2 - x_1y_3}, \tag{B.1}$$

$$\varepsilon_y = \frac{(x_3 - x_2)v_1 + (x_1 - x_3)v_2 + (x_2 - x_1)v_3}{x_2y_3 + x_1y_2 + x_3y_1 - x_2y_1 - x_3y_2 - x_1y_3}, \tag{B.2}$$

$$\gamma_{xy} = \frac{(y_2 - y_3)v_1 + (y_3 - y_1)v_2 + (y_1 - y_2)v_3 + (x_3 - x_2)u_1 + (x_1 - x_3)u_2 + (x_2 - x_1)u_3}{x_2y_3 + x_1y_2 + x_3y_1 - x_2y_1 - x_3y_2 - x_1y_3}. \tag{B.3}$$

Note that the macroscopic stretching direction is parallel to the y coordinate in all figures. To further explore the variation of nanomechanical properties in the observed regions, the Delaunay mesh obtained from the deformation map was used to divide the areas on the corresponding modulus map so that the modulus variation for each triangle could be evaluated. The median value of the soft-matrix modulus in each triangle is treated as the representative modulus. The stress transfer of the network brings about the modulus variation in a local area; thus, I treat this variation as the nano stress (ΔE) in each triangle.

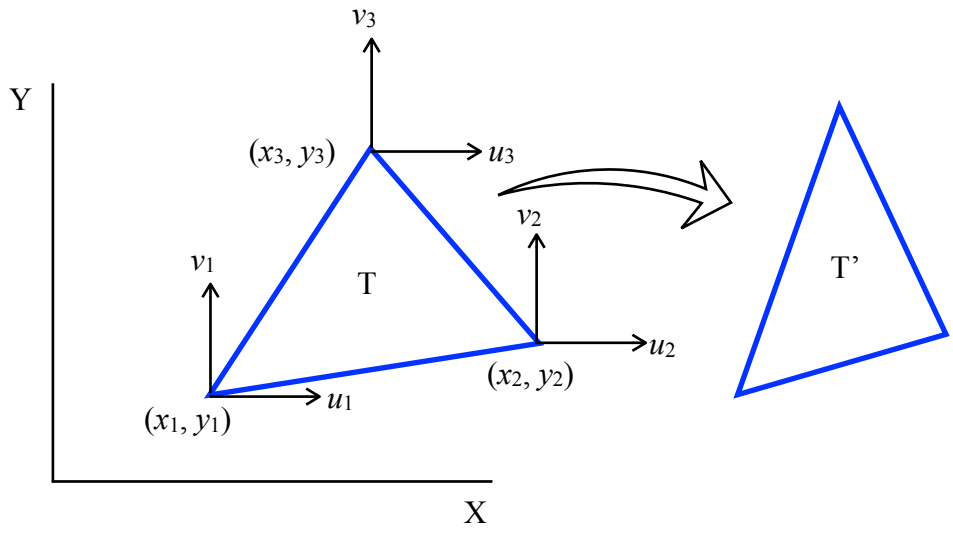

Figure B.1: Notations for the three-node triangle and the schematic diagram of its deformation.

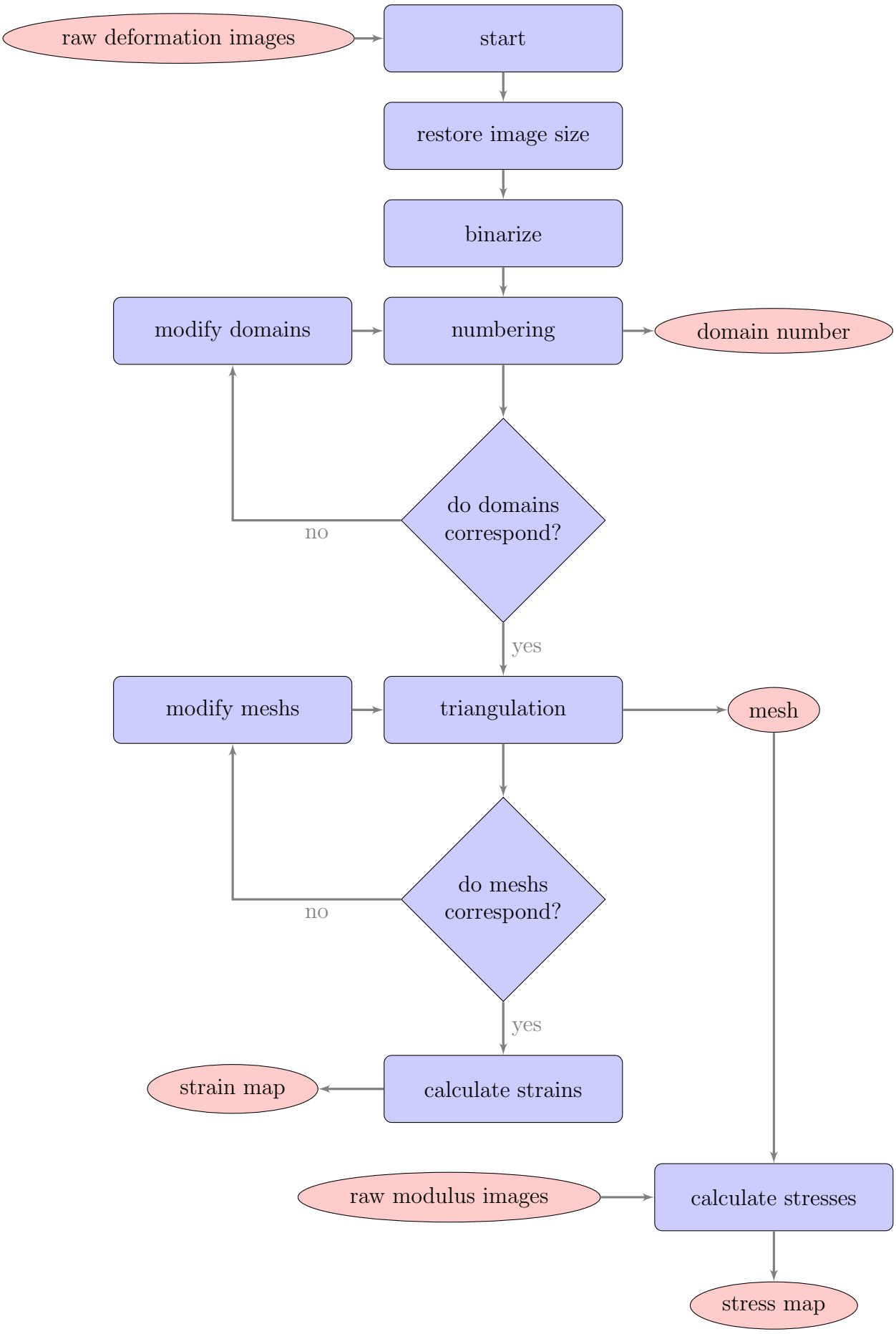

Figure B.2: Flow chart of the program *SSMapping*.

B.2 Step-by-Step Explanation

Input

Two AFM deformation maps are imported into the program. If stresses will also be calculated, the corresponding modulus maps need to be imported at the same time (no necessary in the strain mapping). Since only the resolution of the images (e.g., 256×256 *pixels*) is identified during import, their true size (e.g., 500×500 nm^2) needs to be artificially specified. In order to obtain the true modulus, the modulus range used in the original modulus diagram also needs to be defined manually. The specific code for the above operation is as follows.

```
clc, clear, close all
% image informaton
ImageSizeInNm        = 500;              % Size of AFM images (nm)
ResolutionInPixel    = 256;              % Resolution of AFM images (nm)
% deformation maps (only 'gray color' can be used)
OriginalROI1         = imread('507');    % Read deformation maps
OriginalROI2         = imread('570');
ROIRatio1            = 0.15;             % ROI ratio of deformation maps
ROIRatio2            = 0.15;
% modulus maps (only 'gray color' can be used)
OriginalModulusMap1 = imread('507m'); % Read modulus maps
OriginalModulusMap2 = imread('570m');
% for moving out interface moduli
ModuROIRatio1        = 0.15;             % ROI ratio of modulus maps
ModuROIRatio2        = 0.15;
% set modulus scale for converting color values to moduli values
ModulusMin           = 3000000;          % default color scale of gray image:
ModulusMax           = 20000000;         % [0 65535]
% for domain renumbering (will be used later)
TargetDN1 = {[5];[22  23];[19];[48];...}
TargetDN2 = {[4];[23];[19];[46];[54];...}
% for mesh modification (will be used later)
PreModifiedTN1  = [124;      129;...];
```

```
VertexesOfPMTN1 = [39  48  49;38  39  48;...];
PreModifiedTN2  = [271;          285;...];
VertexesOfPMTN2 = [155  156  185;154  156  185;...];
```

Part 1: The input and definition of AFM images.

Binarization and Domain Numbering

The program will binarize the deformation images to obtain a set of discontinuous domains. The center of each domain is calculated to obtain a set of discrete points. These points will be numbered for post-processing. The results are shown in the Fig. B.3.

```
[ExpandROI1,DomainCenter1,CDSize1] = DomainNumbering(ImageSizeInNm,
    ResolutionInPixel,OriginalROI1,ROIRatio1,TargetDN1);
title('ROI Image 1')
[ExpandROI2,DomainCenter2,CDSize2] = DomainNumbering(ImageSizeInNm,
    ResolutionInPixel,OriginalROI2,ROIRatio2,TargetDN2);
title('ROI Image 2')
```

Part 2: Binarization and domain numbering.

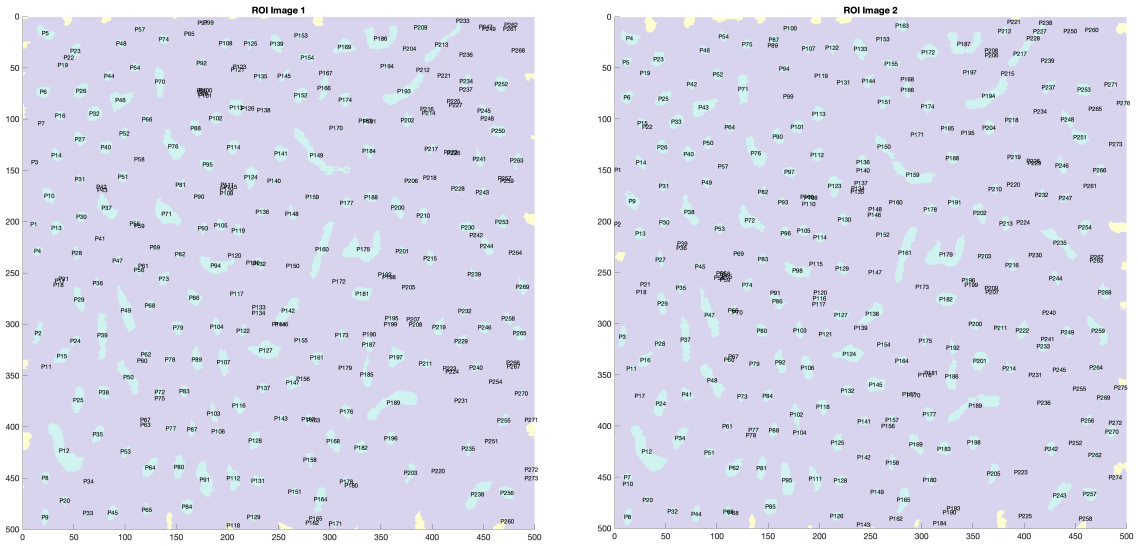

Figure B.3: The binarized deformation map and the numbered domains.

Modification of Numbering

For the subsequent triangulation operation, the domains of the area to be calculated must correspond to each other; thus, the automatically generated numbering needs to be adjusted. The adjustments include the deletion of domains that exist only in one map, and the counting of multiple centers when the same domain splits in another map. The results are shown in the Fig. B.4.

```
ModifiedDC1 = DomainModification(DomainCenter1,TargetDN1,ImageSizeInNm,CDSize1,
    ExpandROI1);
title('Modified ROI Image 1')
ModifiedDC2 = DomainModification(DomainCenter2,TargetDN2,ImageSizeInNm,CDSize2,
    ExpandROI2);
title('Modified ROI Image 2')
```

Part 3: Domain renumbering.

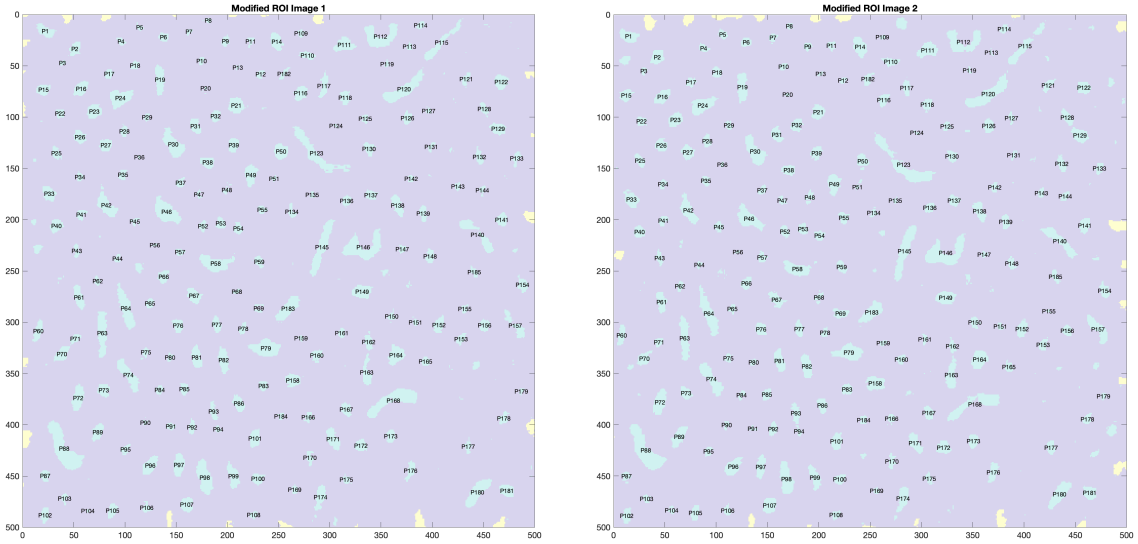

Figure B.4: The renumbered domains.

Delaunay Triangulation

The two sets of points of the two obtained images will be subjected to the first Delaunay triangulation using Matlab's built-in syntax. The results are shown in the Fig. B.5.

```
DelTri1 = DelaunayTriangulation(ExpandROI1,ModifiedDC1,ImageSizeInNm);
title('DelaunayTriangulation for ROI Image 1')
DelTri2 = DelaunayTriangulation(ExpandROI2,ModifiedDC2,ImageSizeInNm);
title('DelaunayTriangulation for ROI Image 2')
```

Part 4: Delaunay triangulation.

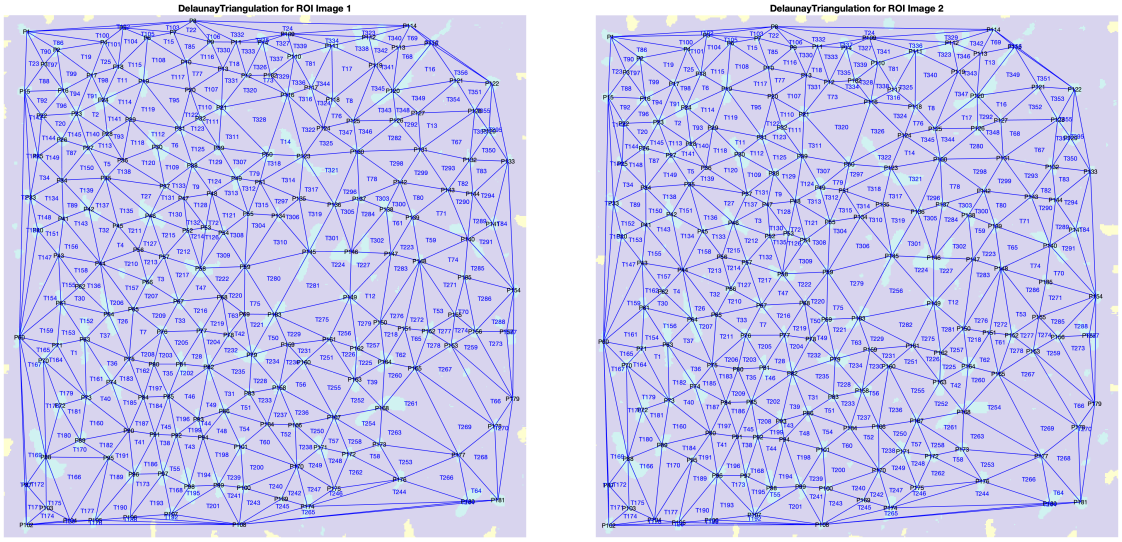

Figure B.5: The Delaunay meshes.

Modification of Delaunay Mesh

The auto-generated Delaunay mesh needs to be fine-tuned so that each triangle corresponds to the other, and the result is shown in the Fig. B.6..

```
[ModifiedDT1,~,~] = DTModification(ExpandROI1,ModifiedDC1,DelTri1,PreModifiedTN1
    ,VertexesOfPMTN1,ImageSizeInNm);
title('Modified DelaunayTriangulation for ROI Image 1')
[ModifiedDT2,~,~] = DTModification(ExpandROI2,ModifiedDC2,DelTri2,PreModifiedTN2
    ,VertexesOfPMTN2,ImageSizeInNm);
title('Modified DelaunayTriangulation for ROI Image 2')
```

Part 5: Modification of Delaunay mesh.

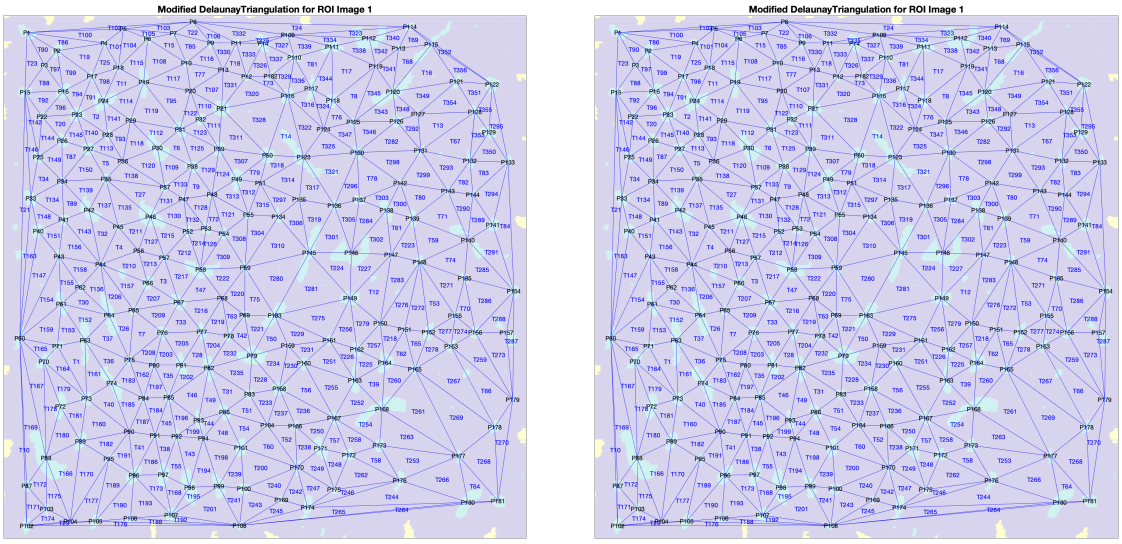

Figure B.6: The modified meshes.

Strain Mapping

The local stress distribution map can finally be successfully generated. The Fig. B.7 shows two examples in the x and y directions.

```
[L1X1,L1Y1,L1X2,L1Y2,L1X3,L1Y3,AllDomainX1,AllDomainY1] = SupplyDisplaying(
    ExpandROI1,ModifiedDT1,ImageSizeInNm,LocalTN1);
[L2X1,L2Y1,L2X2,L2Y2,L2X3,L2Y3,AllDomainX2,AllDomainY2] = SupplyDisplaying(
    ExpandROI2,ModifiedDT2,ImageSizeInNm,LocalTN2);
[ALStrain,AllX,AllY] = StrainAnalyzation(
    ModifiedDT1,ExpandROI1,AllDomainX1,AllDomainY1,L1X1,L1Y1,L1X2,L1Y2,L1X3,L1Y3,
    L2X1,L2Y1,L2X2,L2Y2,L2X3,L2Y3,ImageSizeInNm,LocalTN1,LocalTN2);
```

Part 6: Strain mapping.

Stress Mapping

The stress map can also be further derived in conjunction with the modulus maps. Fig. B.8 shows an example.

```
[Table,ResizedModulusMap1,ResizedModulusMap2,LocalStress] = SSFitting(ALXStrain,
    OriginalROI1,OriginalROI2,OriginalModulusMap1,OriginalModulusMap2,LocalTN1,
```

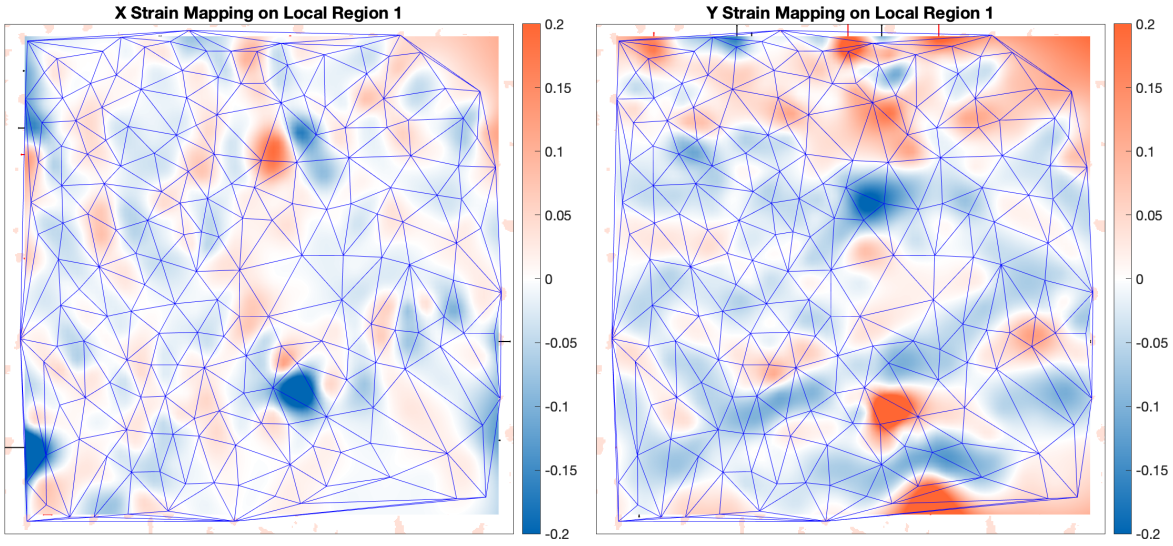

Figure B.7: Strain maps in x and y coordinates.

```
    AllDomainX1, AllDomainY1, ModuROIRatio1, LocalTN2, AllDomainX2, AllDomainY2,
    ModuROIRatio2, ModulusMin, ModulusMax, ImageSizeInNm, ResolutionInPixel);
title('Stress Mapping on ROI Image 1')
```

Part 7: Stress mapping.

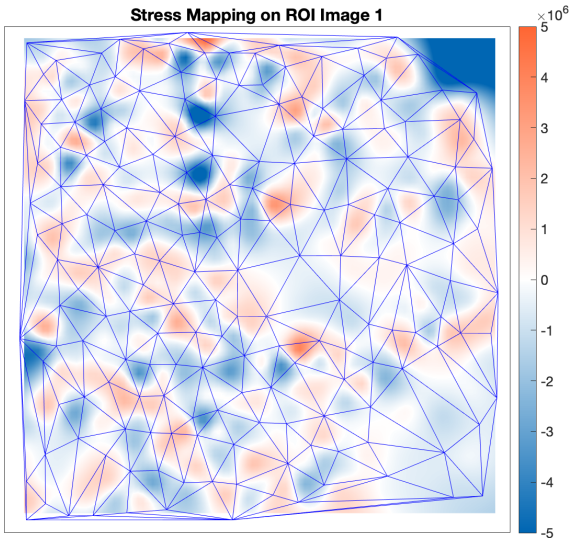

Figure B.8: The stress map.

Functions used in *SSMapping*

Binarization and Domain Numbering

In this function, the program first binarizes the deformation map. The domains located at the edges are then discarded before numbering because the domains at the edges cannot be calculated with the correct geometric centers.

```
function [ExpandROI,DomainCenter,CDSize] = DomainNumbering(ImageSizeInNm,
    ResolutionInPixel,OriginalROI,ROIRatio,CombinedDN)
% recover to original size
IRFactor    = ImageSizeInNm/ResolutionInPixel;
ResizedROI = imresize(OriginalROI,IRFactor);
% binarize image
ROI         = imcomplement(imbinarize(ResizedROI,ROIRatio));
hold on
% expand one array for 4 edges to remove edge particles by 8-connected 'bwlabel'
ExpandROI                                          = zeros(ImageSizeInNm+2,
    ImageSizeInNm+2);
ExpandROI(2:ImageSizeInNm+1,2:ImageSizeInNm+1) = ROI;
ExpandROI(:,1)                                     = 1;
ExpandROI(:,ImageSizeInNm+2)                       = 1;
ExpandROI(1,:)                                     = 1;
ExpandROI(ImageSizeInNm+2,:)                       = 1;
[ROILabel,NumDomain]                               = bwlabel(ExpandROI);
DomainCenter                                       = zeros(NumDomain,2);
% decide domain center
for i = 1:NumDomain
    [DomainX, DomainY] = find(ROILabel == i);
    DomainCenter(i,:)  = [mean(DomainX-1),mean(DomainY-1)]; % used for move the
        matrix to the orginal coords after expanding
end
% delete ROILable = 1 (edge particles which have been 8-connected)
[DomainX, DomainY] = find(ROILabel == 1);
n                  = size(DomainX,1);
for i = 1:n
```

```
26      ExpandROI(DomainX(i),DomainY(i)) = 2;
    end
28  DomainCenter(1,:) = [];
    % operation for combining domain
30  n       = size(CombinedDN,1);
    CDSize = [];
32  if n ~= 0
        for i = 1:n
34          PreCombinedDN = cell2mat(CombinedDN(i,:));
            for j = 1:size(PreCombinedDN,2)
36              [DomainX,~] = find(ROILabel == PreCombinedDN(1,j)+1);
                CDSize(i,j) = size(DomainX,1);
38          end
        end
40  end
    ExpandROI(:,[1 ImageSizeInNm+2]) = [];
42  ExpandROI([1 ImageSizeInNm+2],:) = [];
    imagesc(ExpandROI,'AlphaData',.2)
44  DomainCenter                    = rot90(DomainCenter);
    % label points
46  DomainLabel                     = arrayfun(@(x){sprintf('P%d',x)}, (1:NumDomain
        -1)');
    text(DomainCenter(1,:),DomainCenter(2,:),DomainLabel,'HorizontalAlignment','
        center','Color','black')
48  hold off
    end
```

Function 1: Binarization and domain numbering.

Domain Renumbering

```
1   function ModifiedDC = DomainModification(DomainCenter,CombinedDN,ImageSizeInNm,
        CDSize,ExpandROI)
    % zero matrix
3   n = size(CombinedDN,1);
```

```
ModifiedDC = [];
% make a new matrix
for i = 1:n
    PreCombinedDN      = cell2mat(CombinedDN(i,:));
    PreCombinedDCoord = DomainCenter(:,PreCombinedDN);
    CDCSumX            = 0;
    CDCSumY            = 0;
    for j = 1:size(PreCombinedDN,2)
        CDCSumX = CDCSumX + CDSize(i,j) * DomainCenter(1,PreCombinedDN(j));
        CDCSumY = CDCSumY + CDSize(i,j) * DomainCenter(2,PreCombinedDN(j));
    end
    CombinedDCoordX = CDCSumX / sum(CDSize(i,:));
    CombinedDCoordY = CDCSumY / sum(CDSize(i,:));
    CombinedDCoord  = [CombinedDCoordX;CombinedDCoordY];
    ModifiedDC      = [ModifiedDC,CombinedDCoord];
end
% original image
imagesc(ExpandROI,'AlphaData',.2)
hold on
% label points
Domainlabel = arrayfun(@(x){sprintf('P%d',x)}, (1:size(ModifiedDC,2))');
text(ModifiedDC(1,:),ModifiedDC(2,:),Domainlabel,'HorizontalAlignment','center
    ','Color','black')
hold off
end
```

Function 2: Domain renumbering.

Delaunay Triangulation

```
function DelTri = DelaunayTriangulation(ExpandROI,ModifiedDC,ImageSizeInNm)
imagesc(ExpandROI,'AlphaData',.2)
hold on
DelTri = delaunayTriangulation(ModifiedDC');
triplot(DelTri,'Color','blue','LineWidth',1)
```

```
hold on
% label points
Domainlabel = arrayfun(@(x){sprintf('P%d',x)}, (1:size(ModifiedDC,2))');
text(ModifiedDC(1,:),ModifiedDC(2,:),Domainlabel,'HorizontalAlignment','center','Color','black')
hold on
% label domains' center
TriCenter = incenter(DelTri);
TriLabel  = arrayfun(@(x) {sprintf('T%d', x)}, (1:size(DelTri,1))');
text(TriCenter(:,1),TriCenter(:,2),TriLabel,'HorizontalAlignment','center','Color','blue')
hold off
end
```

Function 3: Delaunay triangulation.

Delaunay-Mesh Modification

```
function [ModifiedDT,DTN,AllTC] = DTModification(ROI,ModifiedDC,DelTri,PreModifiedTN,VertexesOfPMTN,ImageSizeInNm)
imagesc(ROI,'AlphaData',.2)
hold on
% extract delaunay mesh to edit later
ModifiedDT = struct('Points',DelTri.Points,'ConnectivityList',DelTri.ConnectivityList);
% edit mesh
n = size(PreModifiedTN,1);
for i = 1:n
    ModifiedDT.ConnectivityList(PreModifiedTN(i),:) = VertexesOfPMTN(i,:);
end
% new mesh
triplot(ModifiedDT.ConnectivityList,ModifiedDT.Points(:,1),ModifiedDT.Points(:,2))
hold on
% label points
```

```
Domainlabel = arrayfun(@(x){sprintf('P%d',x)},(1:size(ModifiedDC,2))');
text(ModifiedDC(1,:),ModifiedDC(2,:),Domainlabel,'HorizontalAlignment','center','Color','black')
hold on
% new trianglar center
DTN    = size(ModifiedDT.ConnectivityList,1);
AllTC = zeros(DTN:2);
for i = 1:DTN
    VertexNum    = ModifiedDT.ConnectivityList(i,:);
    VertexCoord = ModifiedDT.Points(VertexNum',:);
    TriCenter    = mean(VertexCoord);
    AllTC(i,:)   = TriCenter;
end
% label centers
TriLabel = arrayfun(@(x) {sprintf('T%d',x)}, (1:DTN)');
text(AllTC(:,1),AllTC(:,2),TriLabel,'HorizontalAlignment','center','Color','blue')
hold off
```

Function 4: Delaunay-mesh modification.

Vertices Extraction

This function is used to extract the vertices of the triangle in advance to facilitate the stress calculation later.

```
function [X1,Y1,X2,Y2,X3,Y3,AllDomainX,AllDomainY] = SupplyDisplaying(ROI,
    ModifiedDT,ImageSizeInNm,LocalTN)
% local analysis
n           = size(LocalTN,2);
AllDomainX = zeros(n,3);
AllDomainY = zeros(n,3);
X1          = zeros(n,1);
Y1          = zeros(n,1);
X2          = zeros(n,1);
```

```
Y2          = zeros(n,1);
X3          = zeros(n,1);
Y3          = zeros(n,1);
for i = 1:n
    TriNum          = LocalTN(:,i); % triangle numbers
    TriVertexes     = ModifiedDT.ConnectivityList(TriNum,:); % vertexes of
        triangles
    DomainX         = ModifiedDT.Points(TriVertexes,1); % x coordinates of
        vertexes
    DomainY         = ModifiedDT.Points(TriVertexes,2); % y coordinates of
        vertexes
    X1(i)           = DomainX(1);
    Y1(i)           = DomainY(1);
    X2(i)           = DomainX(2);
    Y2(i)           = DomainY(2);
    X3(i)           = DomainX(3);
    Y3(i)           = DomainY(3);
    AllDomainX(i,:) = DomainX;
    AllDomainY(i,:) = DomainY;
end
end
```

Function 6: Vertices extraction

Strain Mapping

In this function, since the correspondence of each vertex in the two triangles needs to be determined, the calculation of the vector relationship between the three vertices is used to determine the deformation direction of the triangle, which makes the function complicated, as shown in Fig. B.9. Optimization methods are being considered.

```
function [ALStrain,AllX,AllY] = StrainAnalyzation(ModifiedDT1,ROI1,AllDomainX1,
    AllDomainY1,L1X1,L1Y1,L1X2,L1Y2,L1X3,L1Y3,L2X1,L2Y1,L2X2,L2Y2,L2X3,L2Y3,
    ImageSizeInNm,LocalTN1,LocalTN2)
AllXStrain = zeros(n,1);
```

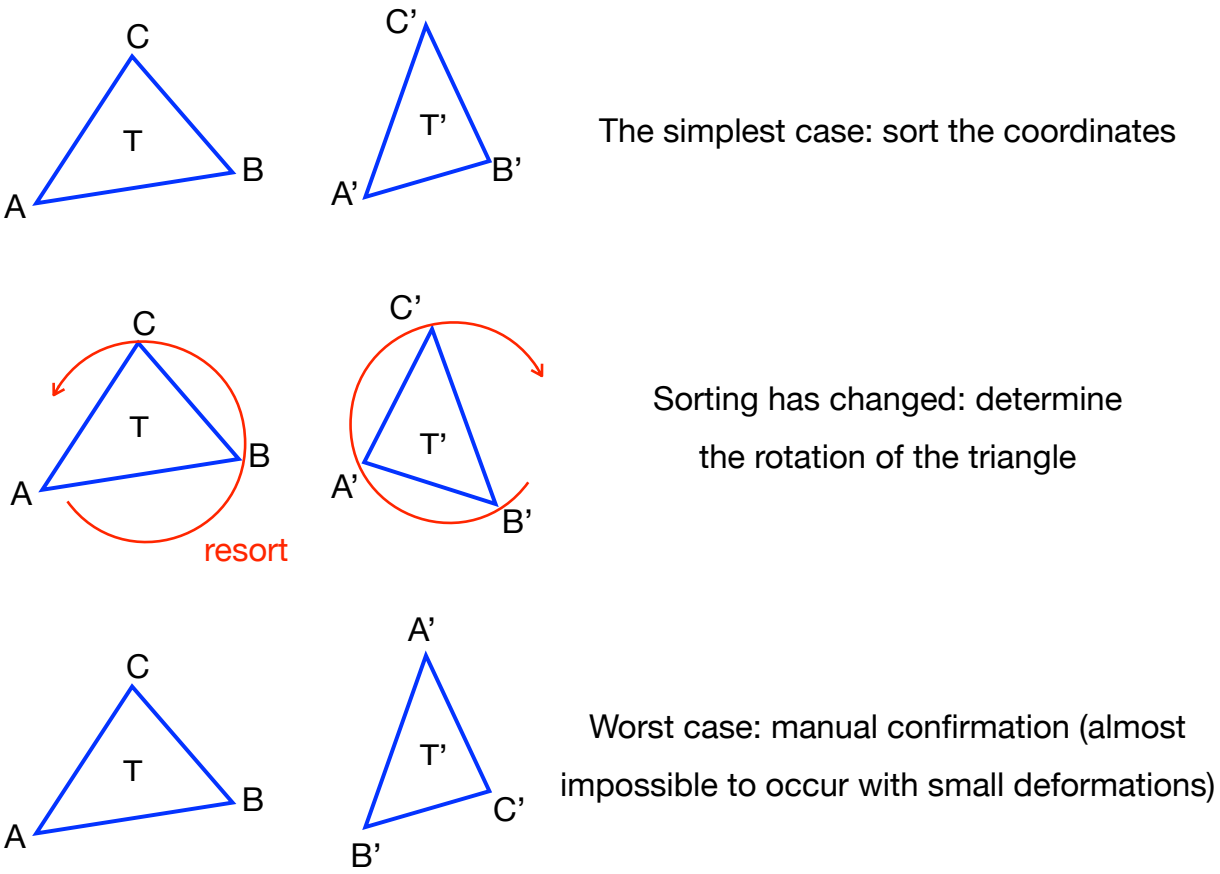

Figure B.9: The method of determining the mapping between two triangles.

```
AllX        = zeros(n,1);
AllY        = zeros(n,1);
for i = 1:n
    A = [L1X1(i);L1X2(i);L1X3(i)];
    B = [L2X1(i);L2X2(i);L2X3(i)];
    % Decide X1 (min)
    if L1X1(i) == min(A)
        if L2X1(i) == min(B)
            T1X1        = L1X1(i);
            T1Y1        = L1Y1(i);
            T2X1        = L2X1(i);
            T2Y1        = L2Y1(i);
            Table1Para1 = 1;
            Table2Para1 = 1;
        else
            if L2X2(i) == min(B)
```

```
                T1X1         = L1X1(i);
                T1Y1         = L1Y1(i);
                T2X1         = L2X2(i);
                T2Y1         = L2Y2(i);
                Table1Para1 = 1;
                Table2Para1 = 2;
            else
                if L2X3(i) == min(B)
                    T1X1         = L1X1(i);
                    T1Y1         = L1Y1(i);
                    T2X1         = L2X3(i);
                    T2Y1         = L2Y3(i);
                    Table1Para1 = 1;
                    Table2Para1 = 3;
                end
            end
        end
    end
    if L1X2(i) == min(A)
        if L2X1(i) == min(B)
            T1X1         = L1X2(i);
            T1Y1         = L1Y2(i);
            T2X1         = L2X1(i);
            T2Y1         = L2Y1(i);
            Table1Para1 = 2;
            Table2Para1 = 1;
        else
            if L2X2(i) == min(B)
                T1X1         = L1X2(i);
                T1Y1         = L1Y2(i);
                T2X1         = L2X2(i);
                T2Y1         = L2Y2(i);
                Table1Para1 = 2;
                Table2Para1 = 2;
            else
```

```
54                  if L2X3(i) == min(B)
                        T1X1         = L1X2(i);
56                      T1Y1         = L1Y2(i);
                        T2X1         = L2X3(i);
58                      T2Y1         = L2Y3(i);
                        Table1Para1 = 2;
60                      Table2Para1 = 3;
                    end
62              end
            end
64      end
        if L1X3(i) == min(A)
66          if L2X1(i) == min(B)
                T1X1         = L1X3(i);
68              T1Y1         = L1Y3(i);
                T2X1         = L2X1(i);
70              T2Y1         = L2Y1(i);
                Table1Para1 = 3;
72              Table2Para1 = 1;
            else
74              if L2X2(i) == min(B)
                    T1X1         = L1X3(i);
76                  T1Y1         = L1Y3(i);
                    T2X1         = L2X2(i);
78                  T2Y1         = L2Y2(i);
                    Table1Para1 = 3;
80                  Table2Para1 = 2;
                else
82                  if L2X3(i) == min(B)
                        T1X1         = L1X3(i);
84                      T1Y1         = L1Y3(i);
                        T2X1         = L2X3(i);
86                      T2Y1         = L2Y3(i);
                        Table1Para1 = 3;
88                      Table2Para1 = 3;
```

```
            end
        end
    end
end
% Decide X2 (max)
if L1X1(i) == max(A)
    if L2X1(i) == max(B)
        T1X2         = L1X1(i);
        T1Y2         = L1Y1(i);
        T2X2         = L2X1(i);
        T2Y2         = L2Y1(i);
        Table1Para2 = 1;
        Table2Para2 = 1;
    else
        if L2X2(i) == max(B)
            T1X2         = L1X1(i);
            T1Y2         = L1Y1(i);
            T2X2         = L2X2(i);
            T2Y2         = L2Y2(i);
            Table1Para2 = 1;
            Table2Para2 = 2;
        else
            if L2X3(i) == max(B)
                T1X2         = L1X1(i);
                T1Y2         = L1Y1(i);
                T2X2         = L2X3(i);
                T2Y2         = L2Y3(i);
                Table1Para2 = 1;
                Table2Para2 = 3;
            end
        end
    end
end
if L1X2(i) == max(A)
    if L2X1(i) == max(B)
```

```
124             T1X2          = L1X2(i);
                T1Y2          = L1Y2(i);
126             T2X2          = L2X1(i);
                T2Y2          = L2Y1(i);
128             Table1Para2 = 2;
                Table2Para2 = 1;
130         else
                if L2X2(i) == max(B)
132                 T1X2          = L1X2(i);
                    T1Y2          = L1Y2(i);
134                 T2X2          = L2X2(i);
                    T2Y2          = L2Y2(i);
136                 Table1Para2 = 2;
                    Table2Para2 = 2;
138             else
                    if L2X3(i) == max(B)
140                     T1X2          = L1X2(i);
                        T1Y2          = L1Y2(i);
142                     T2X2          = L2X3(i);
                        T2Y2          = L2Y3(i);
144                     Table1Para2 = 2;
                        Table2Para2 = 3;
146                 end
                end
148         end
    end
150     if L1X3(i) == max(A)
            if L2X1(i) == max(B)
152             T1X2          = L1X3(i);
                T1Y2          = L1Y3(i);
154             T2X2          = L2X1(i);
                T2Y2          = L2Y1(i);
156             Table1Para2 = 3;
                Table2Para2 = 1;
158         else
```

```
            if L2X2(i) == max(B)
160             T1X2         = L1X3(i);
                T1Y2         = L1Y3(i);
162             T2X2         = L2X2(i);
                T2Y2         = L2Y2(i);
164             Table1Para2 = 3;
                Table2Para2 = 2;
166         else
                if L2X3(i) == max(B)
168                 T1X2         = L1X3(i);
                    T1Y2         = L1Y3(i);
170                 T2X2         = L2X3(i);
                    T2Y2         = L2Y3(i);
172                 Table1Para2 = 3;
                    Table2Para2 = 3;
174             end
            end
176     end
    end
178 % Decide X3 (the other)
    Table1Para3 = 6 - Table1Para1 - Table1Para2;
180 Table2Para3 = 6 - Table2Para1 - Table2Para2;
    if Table1Para3 == 1
182     if Table2Para3 == 1
            T1X3 = L1X1(i);
184         T1Y3 = L1Y1(i);
            T2X3 = L2X1(i);
186         T2Y3 = L2Y1(i);
        else
188         if Table2Para3 == 2
                T1X3 = L1X1(i);
190             T1Y3 = L1Y1(i);
                T2X3 = L2X2(i);
192             T2Y3 = L2Y2(i);
            else
```

```
194                 if Table2Para3 == 3
                        T1X3 = L1X1(i);
196                     T1Y3 = L1Y1(i);
                        T2X3 = L2X3(i);
198                     T2Y3 = L2Y3(i);
                    end
200             end
            end
202     end
        if Table1Para3 == 2
204         if Table2Para3 == 1
                T1X3 = L1X2(i);
206             T1Y3 = L1Y2(i);
                T2X3 = L2X1(i);
208             T2Y3 = L2Y1(i);
            else
210             if Table2Para3 == 2
                    T1X3 = L1X2(i);
212                 T1Y3 = L1Y2(i);
                    T2X3 = L2X2(i);
214                 T2Y3 = L2Y2(i);
                else
216                 if Table2Para3 == 3
                        T1X3 = L1X2(i);
218                     T1Y3 = L1Y2(i);
                        T2X3 = L2X3(i);
220                     T2Y3 = L2Y3(i);
                    end
222             end
            end
224     end
        if Table1Para3 == 3
226         if Table2Para3 == 1
                T1X3 = L1X3(i);
228             T1Y3 = L1Y3(i);
```

```
            T2X3 = L2X1(i);
230         T2Y3 = L2Y1(i);
        else
232         if Table2Para3 == 2
                T1X3 = L1X3(i);
234             T1Y3 = L1Y3(i);
                T2X3 = L2X2(i);
236             T2Y3 = L2Y2(i);
            else
238             if Table2Para3 == 3
                    T1X3 = L1X3(i);
240                 T1Y3 = L1Y3(i);
                    T2X3 = L2X3(i);
242                 T2Y3 = L2Y3(i);
                end
244         end
        end
246 end
    % Check if xmin or xmax have changed to other points during two figure's
        time
248 if ((T1X2 - T1X1) * (T1Y3 - T1Y2) - (T1Y2 - T1Y1) * (T1X3 - T1X2)) * ((T2X2
    - T2X1) * (T2Y3 - T2Y2) - (T2Y2 - T2Y1) * (T2X3 - T2X2)) < 0
     if (abs(T2X2 - T2X3) < abs (T2X1 - T2X3)) && (abs(T2X2 - T2X3) < abs (
        T2X1 - T2X2))
250      T2Inter = T2X3;
         T2X3    = T2X2;
252      T2X2    = T2Inter;
         T2Inter = T2Y3;
254      T2Y3    = T2Y2;
         T2Y2    = T2Inter;
256  end
     if (abs(T2X1 - T2X3) < abs (T2X2 - T2X1)) && (abs(T2X1 - T2X3) < abs (
        T2X2 - T2X3))
258      T2Inter = T2X3;
         T2X3    = T2X1;
```

```
260             T2X1     = T2Inter;
                T2Inter  = T2Y3;
262             T2Y3     = T2Y1;
                T2Y1     = T2Inter;
264         end
    end
266     U1              = T2X1 - T1X1;
    U2              = T2X2 - T1X2;
268     U3              = T2X3 - T1X3;
    XStrain         = ((T1Y2 - T1Y3) * U1 + (T1Y3 - T1Y1) * U2 + (T1Y1 - T1Y2) *
        U3) /...
270      (T1X2 * T1Y3 + T1X1 * T1Y2 + T1X3 * T1Y1 - T1X2 * T1Y1 - T1X3 * T1Y2 -
           T1X1 * T1Y3);
    AllXStrain(i) = XStrain;
272     AllX(i)         = (T1X1+T1X2+T1X3)/3;
    AllY(i)         = (T1Y1+T1Y2+T1Y3)/3;
274     [X,Y,Z]         = griddata(AllX,AllY,ALStrain,linspace(min(AllX),max(AllX))',
        linspace(min(AllY),max(AllY)),'v4');
    PColorMap       = pcolor(X,Y,Z);
276     shading interp
    colorbar
278     uistack(PColorMap,'bottom')
    hold on
280 end
triplot(ModifiedDT1.ConnectivityList,ModifiedDT1.Points(:,1),ModifiedDT1.Points
    (:,2))
282 hold on
TriangleNumber1 = LocalTN1';
284 TriangleNumber2 = LocalTN2';
Table           = table(TriangleNumber1,TriangleNumber2,ALStrain);
286 Table(n+1,:)     = {NaN,NaN,mean(ALStrain)};
BaseImage       = imagesc(ROI1,'AlphaData',.2);
288 uistack(BaseImage,'bottom')
hold on
290 end
```

Function 7: Strain mapping (x coordinate as an example).

Local Modulus

Exporting the stress mapping first requires extracting the modulus of each triangle, which is the function below.

```
function [ALModulus,ResizedModulusMap] = LocalModulus(OriginalModulusMap,
    ModulusMin,ModulusMax,LocalTN,AllDomainX,AllDomainY,OriginalROI,ModuROIRatio,
    ImageSizeInNm,ResolutionInPixel)
% rescale
ModulusMap          = rescale(OriginalModulusMap,ModulusMin,ModulusMax);
% resize
IRFactor            = ImageSizeInNm/ResolutionInPixel;
ResizedROI          = imresize(OriginalROI,IRFactor);
ResizedModulusMap   = imresize(ModulusMap,IRFactor);
% record non-ROI coords (stupid method)
% crop for accelerating
i1                  = floor(min(min(AllDomainX)));
i2                  = ceil(max(max(AllDomainX)));
j1                  = floor(min(min(AllDomainY)));
j2                  = ceil(max(max(AllDomainY)));
ModuROI             = imcomplement(imbinarize(ResizedROI,ModuROIRatio));
LROI                = ModuROI((j1:j2),(i1:i2));
n                   = length(find(LROI == 0));
NROICoord           = zeros(n,2);
k = 1;
for j = j1:j2
    for i = i1:i2
        if ModuROI(j,i) == 0
            NDomainCoord = [i,j];
            NROICoord(k,:) = NDomainCoord;
            k = k+1;
        end
```

```
    end
end
NROICoordX = NROICoord(:,1);
NROICoordY = NROICoord(:,2);
% local analysis
n           = size(LocalTN,2);
ALModulus   = zeros(n,1);
for i = 1:n
    DomainX              = AllDomainX(i,:);
    DomainY              = AllDomainY(i,:);
    [AreaIn,~]           = inpolygon(NROICoordX,NROICoordY,DomainX,DomainY);
    AreaNROIX            = NROICoordX(AreaIn);
    AreaNROIY            = NROICoordY(AreaIn);
    FullSize             = [ImageSizeInNm ImageSizeInNm];
    % change matrix to line
    LineNumber           = sub2ind(FullSize,AreaNROIX,AreaNROIY);
    ModulusForAllPoints  = ResizedModulusMap(LineNumber);
    % median of all modulus
    AverageModulus       = median(ModulusForAllPoints);
    ALModulus(i)         = AverageModulus;
end
end
```

Function 8: Extracting the representative modulus of each triangle.

Stress Mapping

```
function [Table,ResizedModulusMap1,ResizedModulusMap2,LocalStress] = SSFitting(
    ALStrain,OriginalROI1,OriginalROI2,OriginalModulusMap1,OriginalModulusMap2,
    LocalTN1,AllDomainX1,AllDomainY1,ModuROIRatio1,LocalTN2,AllDomainX2,
    AllDomainY2,ModuROIRatio2,ModulusMin,ModulusMax,ImageSizeInNm,
    ResolutionInPixel)
[ALModulus1,ResizedModulusMap1] = LocalModulus(OriginalModulusMap1,ModulusMin,
    ModulusMax,LocalTN1,AllDomainX1,AllDomainY1,OriginalROI1,ModuROIRatio1,
    ImageSizeInNm,ResolutionInPixel);
```

```
[ALModulus2,ResizedModulusMap2] = LocalModulus(OriginalModulusMap2,ModulusMin,
    ModulusMax,LocalTN2,AllDomainX2,AllDomainY2,OriginalROI2,ModuROIRatio2,
    ImageSizeInNm,ResolutionInPixel);
ALStress          = ALModulus2 - ALModulus1;
LocalModulus1     = ALModulus1;
LocalModulus2     = ALModulus2;
TriangleNumber1 = LocalTN1';
TriangleNumber2 = LocalTN2';
Table             = table(TriangleNumber1,TriangleNumber2,LocalModulus1,
    LocalModulus2,LocalStress,LocalStrain);
[X,Y,Z]           = griddata(XAllX,XAllY,LocalStress,linspace(min(XAllX),max(XAllX
    ))',linspace(min(XAllY),max(XAllY)),'v4');
PColorMap         = pcolor(X,Y,Z);
shading interp
colorbar
uistack(PColorMap,'bottom')
hold on
triplot(ModifiedDT1.ConnectivityList,ModifiedDT1.Points(:,1),ModifiedDT1.Points
    (:,2))
hold on
BaseImage = imagesc(ExpandROI1,'AlphaData',.2);
uistack(BaseImage,'bottom')
hold on
end
```

Function 9: Stress mapping.

B.3 References

[1] Wang, D., Liang, X., Russell, T. P. & Nakajima, K. Visualization and quantification of the chemical and physical properties at a diffusion-induced interface using afm nanomechanical mapping. *Macromolecules* **47**, 3761–3765 (2014).

[2] Hutter, J. L. & Bechhoefer, J. Calibration of atomic-force microscope tips. *Review of scientific instruments* **64**, 1868–1873 (1993).

[3] Nakajima, K. *et al.* Nano-palpation afm and its quantitative mechanical property mapping. *Microscopy* **63**, 193–208 (2014).

[4] Johnson, K. L., Kendall, K. & Roberts, a. Surface energy and the contact of elastic solids. *Proceedings of the royal society of London. A. mathematical and physical sciences* **324**, 301–313 (1971).

[5] Miyata, T. *et al.* Nanoscale stress distribution in silica-nanoparticle-filled rubber as observed by transmission electron microscopy: Implications for tire application. *ACS Applied Nano Materials* **4**, 4452–4461 (2021).